January 2017

Investigating Evaporation Of Melting Ice Particles Within A Bin Melting Layer Model

Andrea Neumann

Recommended Citation

Neumann, Andrea, "Investigating Evaporation Of Melting Ice Particles Within A Bin Melting Layer Model" (2017). *Theses and Dissertations*. 2053.
https://commons.und.edu/theses/2053

INVESTIGATING EVAPORATION OF MELTING ICE PARTICLES WITHIN A BIN MELTING LAYER MODEL

by

Andrea J. Neumann
Bachelor of Science, University of North Dakota, 2009
Master of Science, University of North Dakota, 2012

A Dissertation

Submitted to the Graduate Faculty

of the
University of North Dakota

in partial fulfillment of the requirements

for the degree of

Doctor of Philosophy

Grand Forks, North Dakota
December
2016

This dissertation, submitted by Andrea J. Neumann in partial fulfillment of the requirements for the Degree of Doctor of Philosophy from the University of North Dakota, has been read by the Faculty Advisory Committee under whom the work has been done and is hereby approved.

____
Michael Poellot

____
Mark Askelson

____
Gretchen Mullendore

____
Soizik Laguette

____
Andrew Heymsfield

This dissertation is being submitted by the appointed advisory committee as having met all of the requirements of the School of Graduate Studies at the University of North Dakota and is hereby approved.

____
Grant McGimpsey
Dean of the School of Graduate Studies

____
Date

PERMISSION

Title	Investigating Evaporation of Melting Ice Particles within a Bin Melting Layer Model
Department	Atmospheric Sciences
Degree	Doctor of Philosophy

In presenting this dissertation in partial fulfillment of the requirements for a graduate degree from the University of North Dakota, I agree that the library of the University shall make it freely available for inspection. I further agree that permission for extensive copying for scholarly purposes may be granted by the professor who supervised my dissertation work or, in his absence, by the Chairperson of the department or the dean of the School of Graduate Studies. It is understood that any copying or publication or other use of this dissertation or part thereof for financial gain shall not be allowed without my written permission. It is also understood that due recognition shall be given to me and to the University of North Dakota in any scholarly use which may be made of any material in the dissertation.

Andrea Neumann
28 November 2016

TABLE OF CONTENTS

LIST OF FIGURES

LIST OF TABLES

ACKNOWLEDGEMENTS

I wish to express my sincere appreciation to the members of my faculty advisory committee for all of their guidance, support, and encouragement during my time in the doctoral program at the University of North Dakota including:

Prof. Michael Poellot for ten years of guidance and mentorship. Thanks to your efforts I have been able to participate in three NASA field campaigns and a handful of local flight projects, gotten to collect the data I use in both my master's thesis and doctoral dissertation, and learn some awesome things about clouds, physics, and instrumentation. Thank you for the many hours of time you have devoted to reading my senior project, master's thesis, and doctoral dissertation.

Dr. Mark Askelson for all your help with my master's thesis and doctoral dissertation. My writing has definitely improved under your patient tutelage.

Dr. Gretchen Mullendore for being an awesome role model. You have consistently shown me by example of how to be both a good scientist and a good teacher. Thank you again for allowing me the opportunity to see things from the other side of the podium and teach a class.

Dr. Andrew Heymsfield for inspiring me with your passion for cloud physics science and creativity. It was truly fantastic to work with you for a whole summer at NCAR and being able use your knowledge (both in person and in the form of the large mountain of published

research you have authored and co-authored). Thank you also for authoring the PMM proposal that allowed me to be able to do my doctoral degree.

Dr. Soizik Laguette for agreeing to serve on my doctoral committee and being genuinely interested in my work. I thought of you often when writing my dissertation as a reminder to write so that those both within my research specialty and the general science community can understand what I am trying to say.

Besides my faculty advisory committee, there are many other people who deserve my appreciation:

Dr. David Delene for the numerous hours spent teaching and debating how to write data processing code and fix airborne (and some surface-based) instrumentation.

Joseph O'Brien for helping me out with two NASA field campaigns, a whole lot of coding, bearing with the CSI, and being a great friend.

Ryan Stanfield, Shaoyue (Emily) Qui, and Travis Toth for working through the master's and doctoral degrees together with me.

The previous doctoral students in the UND Atmospheric Sciences program who showed me that getting the doctoral degree takes work, but is possible.

The graduate students, both past and present, who I have had the pleasure to work alongside. I will cherish the many experiences we have shared together, from tornado chasing, aurora viewing, to the many parties and get-togethers we have attended.

The members of Redeemer Lutheran Church and the Grand Forks Curling Club whose stories of their extremely various life experiences have given me perspective on my own.

My family who has supported me my whole life and really encouraged me to pursue my goals. I know there are a few of them who are very excited to be able to call me “Dr. Andrea”.

And finally my biggest thank you to Kevin, my fiancée. Thank you for your continual support and encouragement even though we were often a quarter of a continent or more away from each other.

ABSTRACT

Single column models have been used to help develop algorithms for remote sensing retrievals. Assumptions in the single-column models may affect the assumptions of the remote sensing retrievals. Studies of the melting layer that use single column models often assume environments that are near or at water saturation. This study investigates the effects of evaporation upon melting particles to determine whether the assumption of negligible mass loss still holds within subsaturated melting layers. A single column, melting layer model is modified to include the effects of sublimation and evaporation upon the particles. Other changes to the model include switching the order in which the model loops over particle sizes and model layers; including a particle sedimentation scheme; adding aggregation, accretion, and collision and coalescence processes; allowing environmental variables such as the water vapor diffusivity and the Schmidt number to vary with the changes in the environment; adding explicitly calculated particle temperature, changing the particle terminal velocity parameterization; and using a newly-derived effective density-dimensional relationship for use in particle mass calculations.

Simulations of idealized melting layer environments show that significant mass loss due to evaporation during melting is possible within subsaturated environments. Short melting distances, accelerating particle fall speeds, and short melting times help constrain the amount of mass lost due to evaporation while melting is occurring, even in subsaturated profiles. Sublimation prior to melting can also be a significant source of mass loss. The trends shown on the particle scale also appear in the bulk distribution parameters such as rainfall rate and ice water content.

Simulations incorporating observed melting layer environments show that significant mass loss due to evaporation during the melting process is possible under certain environmental conditions. A profile such as the first melting layer profile on 10 May 2011 from the Midlatitude Continental Convective Clouds Experiment (MC3E) that is neither too saturated nor too subsaturated is possible and shows considerable mass loss for all particle sizes. Most melting layer profiles sampled during MC3E were too saturated for more than a dozen or two of the smallest particle sizes to experience significant mass loss. The aggregation, accretion, and collision and coalescence processes also countered significant mass loss at the largest particles sizes because these particles are efficient at collecting smaller particles due to their relative large sweep-out area.

From these results, it appears that the assumption of negligible mass loss due to evaporation while melting is occurring is not always valid. Studies that use large, low-density snowflakes and high RH environments can safely use the assumption of negligible mass loss. Studies that use small ice particles or low RH environments (RH less than about 80%) cannot use the assumption of negligible mass loss due to evaporation. Retrieval algorithms may be overestimating surface precipitation rates and intensities in subsaturated environments due to the assumptions of negligible mass loss while melting and near-saturated melting layer environments.

CHAPTER I
INTRODUCTION

Instruments such as the Global Precipitation Measurement (GPM) satellite microwave imager (GMI) and dual-frequency precipitation radar (DPR) are used to measure microwave radiation being emitted and scattered upwards in the satellite's direction. For passive radiometers such as the GMI, many different cloud and precipitation profiles can result in similar radiometric brightness temperatures. Thus, Bayesian estimation methods are used to determine which cloud and precipitation profiles are most likely to cause current brightness temperatures (Petty and Li 2013). Melting hydrometeors can have a large impact upon the microwave energy being observed with a satellite. Olson et al. (2001b) found that partially melted particles have enhanced microwave absorption and scattering efficiencies compared to dry ice particles. Because of the increase in the absorption and scattering efficiencies, the brightness temperatures in the 10.65 to 85.5 GHz frequency range are larger for simulations of precipitation that include melting than for simulations that do not include melting (Olson et al. 2001a).

Active remote sensing platforms such as DPR measure the time between transmission of microwave energy and the reception of its "echo" to determine a radar reflectivity profile. The radar reflectivity profiles give rough estimates of the precipitation rate within a column. However, there is not always a direct relationship between reflectivity and precipitation rate. Within melting regions, "bright bands" of radar reflectivity factors are sometimes observed.

These bright bands are caused by large melting ice particles which have a dielectric constant somewhere between the dielectric constant of pure ice (0.197) and pure water (0.93). Bright bands can cause skewed precipitation intensity and accumulation estimates from ground radar data, but can also be used to determine stratiform rain regions from satellite radar data (Iguchi et al. 2010).

Scattering and absorption properties of melting particles is being investigated to help improve estimates of cloud and precipitation retrievals. Since melting hydrometeors have such different scattering and absorption properties than rain or dry snow, work is needed to accurately portray these particles. Processes such as evaporation can influence the scattering and absorption properties of melting particles. Evaporation removes liquid water from the melting particle, which should make it radiometrically more like dry snow, whereas condensation increases the liquid water mass upon melting particles, making them radiometrically more like very large raindrops. Incorrect assumptions about the effects of evaporation upon melting particles could cause biases within the cloud and precipitation retrievals from both active and passive microwave radiometers.

This study aims to further melting layer research by analyzing the assumption that mass loss due to evaporation during melting is negligible. The specific goal of this study is to determine whether a melting ice particle loses a significant fraction of its mass due to evaporation and if so, how long it takes for this to occur.

CHAPTER II
BACKGROUND

For this study, understanding when and where evaporation plays a role within the melting layer will determine whether this processes is significant within the layer. Some studies such as Mitra et al. (1990) and Hardaker et al. (1995) assume that the mass loss due to evaporation is negligible. The justification of this assumption in Mitra et al. (1990) is that typical melting layers are at or near saturation and large snowflakes fall too quickly through the melting for much, if any, evaporation to occur. Szyrmer and Zawadzki (1999) take into account condensational growth of melting ice particles in water saturated and supersaturated environments. They state that an ice particle can gain up to 7% of its original mass during the melting process in a water saturated environment. However, they do not say anything about mass loss due to evaporation in subsaturated environments. Beyond these studies, there is an apparent lack of research on ice particle melting rates in subsaturated environments.

Most models appear to assume that the particles are always melting within cloud or a high RH environment. Places where ice particles may fall into warm subsaturated environments are:

- below mesoscale convective system (MCS) anvils
- below cloud base in a MCS

- elevated regions of precipitation advecting over a dry lower layer, such as the leading edge of a rainband
- the downstream region of an orographic wave cloud.

Evaporation has two functions related to ice particle melting: it removes heat and mass from the particle. Removal of heat due to melting will keep the particle temperature at 273 K and slow down the melting rate. In sub-saturated environments, sublimation will remove ice mass from the ice particle before enough heat has been imparted to the ice particle to induce melting, causing a reduction in terminal velocity and slowing the melting process. After melting has started, the evaporation will have the following effects:

- removing liquid water mass, which changes the melted fraction of the particle and further reduces the total mass;
- changing the melted fraction of the particle changes the capacitance of the particle, which in turn affects the melting and evaporation rates,
- reducing the liquid water mass decreases the density of the ice particle, while melting offsets this by increasing the density,
- reducing the liquid water mass also decreases the effective dielectric constant, thus reducing the reflectivity of the melting ice particles
- increasing the amount of water vapor in the air increases the relative humidity and feeds back into the melting rate.

CHAPTER III
MELTING LAYER MODEL CHANGES AND SENSITIVITY TESTS

This experiment utilizes a melting layer model that was originally written by Olson et al. (2001) and modified since. It is a 1D bin microphysical model that describes the vertical distribution of melting precipitation particles. The melting rate of the particles is calculated at all model levels and particles are not allowed to refreeze once they begin to melt. Terminal velocity of raindrops are parameterized following Battaglia et al. (2003) and the terminal velocity of ice particles are parameterized following Heymsfield and Westbrook (2010). This chapter includes a derivation of the melting rate equation, a description of changes to the model, and results of some sensitivity tests. Other equations included in the model are presented in the Appendix.

Derivation of Melting Rate Equation

The energy budget of a melting ice particle usually assumes that only three processes are occurring: heat conduction from the atmosphere, heat loss due to evaporation, and heat loss due to the endothermic melting of ice. Energy gain or loss from accretion of cloud water or aggregation with other ice particles is typically ignored. The derivation of the melting rate equation from energy budget of a melting particle is based on the work in Rasmussen and Heymsfield (1987):

$$\left(\frac{dq}{dt}\right)_{conduction}+\left(\frac{dq}{dt}\right)_{melt}+\left(\frac{dq}{dt}\right)_{evaporation}+\left(\frac{dq}{dt}\right)_{accretion}=0 \tag{3-1}$$

where $\left(\frac{dq}{dt}\right)_{conduction}$ is the latent heat given to the ice particle through heat conduction of the atmosphere, $\left(\frac{dq}{dt}\right)_{melt}$ is the latent heat used in the melting of the ice contained within the ice particle, $\left(\frac{dq}{dt}\right)_{evaporation}$ is the latent heat lost due to evaporation, and $\left(\frac{dq}{dt}\right)_{accretion}$ is the sensible heat transferred from the accretion of cloud droplets. For this study, the sensible heat transfer from accreted cloud droplets is ignored. The latent heat gain due to conduction is given by

$$\left(\frac{dq}{dt}\right)_{conduction}=4\pi CDk_a f_h\left(T_\infty-T_p\right) \tag{3-2}$$

where *C* is the dimensionless capacitance factor of the melting ice particle, *D* is the diameter of the melting ice particle, k_a is the thermal conductivity of air, f_h is the thermal ventilation coefficient, T_∞ is the ambient air temperature, and T_p is the temperature of the melting ice particle. Even though this study assumes spherical ice particles, (3-2) uses an ice crystal capacitance following Mitra et al. (1990). The use of the ice particle capacitance allows for an easy way to account for non-spherical particle shapes. Following Westbrook and Heymsfield (2011) the ice crystal capacitance is broken up into the particle diameter (*D*) and the capacitance factor (*C*) since the capacitance is often a factor of *D*.

The latent heat absorbed by the melting process is equal to

$$\left(\frac{dq}{dt}\right)_{melt} = L_f\left(\frac{dm_m}{dt}\right) \tag{3-3}$$

where L_f is the latent heat of fusion and m_m is the mass of ice that is melted. The latent heat loss due to evaporation is

$$\left(\frac{dq}{dt}\right)_{evaporation} = L_e\left(\frac{dm_e}{dt}\right) = \frac{4\pi CDL_e f_v \psi}{R_v}\left[\frac{e(T_\infty)}{T_\infty} - \frac{e_s(T_p)}{T_p}\right] \tag{3-4}$$

where L_e is the latent heat of evaporation, m_e is the mass of evaporated water, f_v is the water vapor ventilation coefficient, ψ is the diffusivity of water vapor in air, R_v is the gas constant for water vapor, $e(T_\infty)$ is the actual ambient vapor pressure, and $e_s(T_p)$ is the saturated vapor pressure of the melting ice particle. The actual vapor pressure can be approximated as

$$e(T_\infty) = RHe_s(T_\infty) \tag{3-5}$$

where RH is the relative humidity of the air and $e_s(T_\infty)$ is the saturated vapor pressure of the air.

The melting rate of the ice particle is derived through substitution of equations (3-2) through (3-5) into (3-1) and solving for $\left(\frac{dm_m}{dt}\right)$:

$$\left(\frac{dm_m}{dt}\right) = \frac{4\pi CDf_v}{L_f}\left\{k_a\left(T_\infty - T_p\right) + \frac{L_e\psi}{R_v}\left[\frac{RHe_s(T_\infty)}{T_\infty} - \frac{e_s(T_p)}{T_p}\right]\right\} \tag{3-6}$$

One more assumption that goes into (3-6) is that the heat ventilation coefficient is approximately equal to the water vapor ventilation coefficient (f_v) and thus f_v is able to be a common factor for the heat conduction and the evaporation terms.

Changes to the Melting Layer Model

The melting layer model is modified to receive input of temperature, relative humidity, and pressure profiles from outside of the model. This allows for incorporation of observed melting layer profiles as well as idealized profiles with set temperature and relative humidity lapse rates.

In order to conduct this study, the evaporation and sublimation processes are defined within the model. Olson et al. (2001) assume that the melting of the hydrometeors occurs within a saturated environment and thus do not take into account mass changes due to condensation, evaporation, deposition, or sublimation. Deposition or sublimation begins at the very top of the melting layer since the ice particle does not have any liquid water on its surface. This process is represented by

$$\frac{dm_i}{dt} = \frac{4\pi CDf_v\psi}{R_v}\left[\frac{RHe_s\left(T_\infty\right)}{T_\infty} - \frac{e_{si}\left(T_p\right)}{T_p}\right] \tag{3-7}$$

where $\frac{dm_i}{dt}$ is the rate of change of the particle ice mass (m_i), and e_{si} is the saturated vapor pressure over ice. e_{si} is computed using the equation set from Buck (1981), given by

$$e_{si}\left(T\right) = a_i f_e \exp\left[\left(b_i - \frac{T}{d_i}\right)\frac{T}{T+c_i}\right] \tag{3-8}$$

where T is the temperature in degrees Celsius and f_e is an enhancement factor, given by

$$f_e = 1.0 + 10^{-4}\left[2.2 + \frac{P}{1000}\left(0.0383 + 6.4 * 10^{-5}T\right)\right]$$

The coefficients for (3-8) are provided in Table 3-1 and P is the air pressure in Pascals. Once melting has started, it is assumed that condensation or evaporation is occurring on the melting portions of the ice particle. The evaporation process is represented by (3-4).

Table 3-1: The values and units of the coefficients within equation (3-8).

Coefficient	Value	Unit
a_i	6.1115	hPa
b_i	23.036	None
c_i	279.82	°C
d_i	333.7	°C

In Olson et al. (2001), the model is looped through all of the model layers to calculate the parameters for a single particle size, and then the same is done for each particle size. Looping through the equations in this manner makes the model very fast, efficient, and allows for no numerical diffusion of the particle concentration through the model layers. However, this way of running the model makes it difficult to compute parameters such as aggregation because the model assumes constant number concentration throughout the model depth for each particle size and the time steps between model layers vary between size bins. Therefore, the order of looping through equations is changed so that the model loops though all of the particle sizes on a model layer before performing the calculations for the next model layer. This introduces the need for a time step and for a sedimentation scheme. The sedimentation equation is given here:

$$n(D,k+1) = n(D,k) + n(D,k-1)v_t(D,k-1)\frac{\Delta t}{\Delta z} - n(D,k)v_t(D,k)\frac{\Delta t}{\Delta z} \qquad (3\text{-}9)$$

where $n(D,k+1)$, $n(D,k)$, and $n(D,k-1)$ are the number concentration for a particle with diameter *D* at the *k*th plus one, *k*th, and the *k*th minus one model levels respectively; $v_t(D,k)$ and $v_t(D,k-1)$ are the terminal velocities of particle size *D* at the *k*th and *k*th minus one model levels, Δt is the time step of the model, and Δz is the depth of an individual model layer.

In addition to melting, aggregation, accretion, and collision and coalescence (henceforth abbreviated as A/A/CC) can be important processes within the melting layer. The "continuous growth model" (Pruppacher and Klett 1997, p. 617) is used to represent the A/A/CC processes; this model assumes that all particles with a given size collect the same amount of mass in a given time period. Since this model explicitly tracks both ice and liquid water mass for each particle, one set of equations can be used to represent the aggregation, accretion, and collision and coalescence processes simultaneously. There are two mass collection equations, one for ice mass and one for liquid water mass which were modified from (Pruppacher and Klett 1997, their equations 15-2 and 15-3) and are given as

$$\left(\frac{dm_{ai}}{dt}\right)=\sum_{x=1}^{N}K\left(D,D_x\right)n\left(D_x\right)m_i\left(D_x\right)\Delta D_x \tag{3-10}$$

$$\left(\frac{dm_{al}}{dt}\right)=\sum_{x=1}^{N}K\left(D,D_x\right)n\left(D_x\right)m_l\left(D_x\right)\Delta D_x \tag{3-11}$$

where $\left(\frac{dm_{ai}}{dt}\right),\left(\frac{dm_{al}}{dt}\right)$ is the mass rate of change of ice, liquid water for the current collector particle of diameter D, respectively; m_{ai} is the ice mass collected through A/A/CC; m_{al} is the liquid water mass collected through A/A/CC; N is the total number of particle size bins; and $n(D_x)$ is the number concentration for the particle size D_x; $m_i(D_x)$ is the ice mass within particle D_x; $m_l(D_x)$ is the liquid water mass within particle D_x; ΔD_x is the width of the particle size bin; and $K(D,D_x)$ is the gravitational collection kernel between particles D and D_x. $K(D,D_x)$ is given by

$$K\left(D,D_x\right)=\frac{\pi}{4}E_c\left(D+D_x\right)^2\max\left[v_t\left(D\right)-v_t\left(D_x\right),0\right] \tag{3-12}$$

where $v_t(D)$ is the terminal velocity of particle D and $v_t(D_x)$ is the terminal velocity of particle D_x, and E_c is the collection efficiency. Currently E_c is set to 1.0 for all combinations of particle sizes. The rate of change in the number concentration as a result of the A/A/CC processes is

$$\left(\frac{dn(D)}{dt}\right) = -n(D)\sum_{x=1}^{N} K(D_x, D)\,n(D_x)\,\Delta D_x \qquad \text{(3-13)}$$

Equation (3-13) determines the number of particles of size D that are being collected by all of the other particle collectors in the size distribution. The maximum function within (3-12) ensures that the current particle D cannot collect a faster moving drop than itself. Since that does not happen due to gravitational sedimentation alone, the value of (3-13) for that particle combination is set to zero.

Because the model uses a moving grid, the mean diameter of each size bin changes as the particles undergo mass changing processes (e.g. aggregation, sublimation, etc.); there is no movement of particles from size bin to size bin, leading to no distribution dispersion within an individual model layer (Jacobson and Turco 1995). Unless a particle is completely evaporated/sublimated away, the evaporation, melting, and sublimation processes will only change parameters such as mean size of the size bin and mass on the particle, and will not affect the number concentration of particles within the bin.

Since nucleation of new particles is not addressed with this model, the only changes to the number concentration within a single bin are due to

- loss from A/A/CC,
- loss due to complete evaporation and sublimation, and
- gain or loss from sedimentation between model layers.

When a particle loses all mass due to evaporation/sublimation, the masses, diameters, and number concentration associated with that particle size are all set to zero. Changes in the number concentration within a layer for a single bin is determined by

$$n(D) = n(D) + \left(\frac{dn(D_r)}{dt} \right) \Delta t \qquad (3\text{-}14)$$

The resultant masses of ice and liquid water for the particle after the evaporation/sublimation, melting, and A/A/CC processes are

$$m_i = \begin{cases} m_i + \Delta m_{ai} - \Delta m_m - \Delta m_s & m_i + \Delta m_{ai} \geq \Delta m_m + \Delta m_s \\ 0 & m_i + \Delta m_{ai} < \Delta m_m + \Delta m_s \end{cases} \qquad (3\text{-}15)$$

$$m_l = \begin{cases} m_l + \Delta m_{al} + \Delta m_m + \Delta m_e & m_l + \Delta m_{al} + \Delta m_m \geq \Delta m_e \\ 0 & m_l + \Delta m_{al} + \Delta m_m < \Delta m_e \end{cases} \qquad (3\text{-}16)$$

where m_i is the total ice mass of the particle, Δm_{ai} is the change of ice mass due to aggregation, Δm_m is the change of ice mass due to melting in a given time step, Δm_s is the change of ice mass due to deposition/sublimation, m_l is the total liquid mass of the particle, Δm_{al} is the change of liquid mass due to accretion and collision and coalescence, and Δm_e is the change of liquid water mass due to condensation/evaporation Currently, the model is configured to have a static environment so that changes in particle mass due to the evaporation and sublimation processes do not feed back into the model temperature and relative humidity profiles.

Sensitivity Tests

Several sensitivity studies are conducted with the melting layer model in order to determine sensitivity to certain environmental and particle properties. For all sensitivity study simulations, an idealized melting layer 1 km deep is used with 100 model levels, a constant 6.5 K km^{-1} temperature lapse rate (Γ_∞), and 80% RH at all model layers. 1200 ice particles are simulated ranging from 20 µm to 25 mm in diameter and the A/A/CC processes are turned off.

The pressure profile within the idealized simulations is given by

$$P = P_{surf} \exp\left(\frac{-h}{H}\right) \tag{3-17}$$

where P_{surf} is the pressure at the Earth's surface, h is the altitude of a model layer, and H is the scale height of the atmosphere. For the sensitivity tests, P_{surf} is set to 970 hPa and H is equal to 7729 m. The altitude (above ground level) of the top layer of the model (h_0) is determined by

$$h_0 = \frac{T_{surf}}{\Gamma_\infty} \tag{3-18}$$

where T_{surf} is the local Earth's surface temperature, which is set to 19.5 °C. From (3-17), (3-18), and the given P_{surf}, H, T_{surf} and Γ_∞, the top of the model domain is at 3 km above ground level.

Three of the sensitivity studies are conducted on thermal conductivity of air (k_a), the latent heat of vaporization (L_v), and the latent heat of fusion (L_f). For each variable, a model run is conducted using a constant value and another run uses an equation to compute the variable according to changes in air temperature. The constant values and equations for k_a, L_f, and L_v are shown in Table 3-2. Results from these simulations (not shown) indicate that the values of k_a, L_v, and L_f vary little within typical melting layer environments and variations within these parameters have little effect upon the melting, sublimation, and evaporation processes.

Table 3-2: Constant values and equations for the thermal conductivity of air (*k_a*), latent heat of fusion (*L_f*), and latent heat of vaporization (*L_v*). Equation for *k_a* came from Beard and Pruppacher (1971) and the equations for *L_f* and *L_v* are based on 2.14 in Rogers and Yau (1996).

Parameter	Constant	Equation
k_a	2.43*10^{-2} J m^{-1} s^{-1} K^{-1}	$0.02380696+7.1128*10^{-5}\left(T_\infty-273.15\right)$
L_f	2.34*10^{5} J kg^{-1}	$3.33*10^{5}-\left(2050-4210\right)\left(T_\infty-273.15\right)$
L_v	2.5*10^{6} J kg^{-1}	$2.501*10^{6}-(4210-1870)\left(T_\infty-273.15\right)$

Water Vapor Diffusivity and the Schmidt Number

The melting layer model originally came with an assumed constant water vapor diffusivity (ψ) value of 2.21*10^{-5} m^2 s^{-1}. However, Oraltay and Hallett (2005) state that the dependence of ψ with respect to pressure cannot be ignored. Hall and Pruppacher (1976) state that ψ can be determined by:

$$\psi = 2.11*10^{-5}\left[\frac{P_0}{P}\right]\left[\frac{T_\infty}{T_0}\right]^{1.94}, \tag{3-19}$$

where P is the air pressure at model level k, P_0 is equal to 101325 Pa and T_0 is equal to 273.15 K. Table 3-3 reiterates the importance of pressure upon ψ by showing that values of ψ computed using (3-19) can differ up to 50% from an assumed constant value of 2.21* 10^{-5} m^2 s^{-1}. Water vapor diffusivity is a factor in the equations that govern evaporation, sublimation, melting, and the particle surface temperature.

Table 3-3: Values of air density and water vapor diffusivity as a function of given atmospheric pressure and temperature using (3-19) and the relative difference from a constant 2.21*10^{-5} m^2 s^{-1} water vapor diffusivity.

Pressure [hPa]	Temperature [°C]	Air Density [kg m^{-3}]	ψ [m^2 s^{-1}]	% difference from ψ_0
660	5	0.83	3.36*10^{-5}	51.8
660	0	0.84	3.24*10^{-5}	46.6
760	5	0.95	2.91*10^{-5}	31.9
760	0	0.97	2.81*10^{-5}	27.3
1000	5	1.25	2.21*10^{-5}	0.0
1000	0	1.28	2.14*10^{-5}	3.3

To demonstrate how much ψ impacts the melting rate, two model simulations are run. One simulation utilizes a constant ψ and the other utilizes ψ computed using (3-19) at each model layer. Figure 3-1 shows that changing ψ has a large impact upon the amount of ice mass melted in each model layer. The variable ψ model run has melting commencing at a lower altitude than the constant ψ run. The peak melt amount is about 10% greater for the variable ψ case (at 0.40 km) than for the constant ψ case at 0.35 km. This trend is similar for all ice particle sizes simulated in the model.

Similarly to ψ, the Schmidt number (Sc) is a factor in the ventilation coefficient of the ice particle, which in turns affects the evaporation, melting, and sublimation rates. Sc is given in Hall and Pruppacher (1976) as

$$Sc = \frac{\eta}{\psi \rho_a}, \tag{3-20}$$

where η is the dynamic viscosity of air from List (1984) and is given by

$$\eta = 1.832 * 10^{-5} \left(\frac{296.16 + 120.0}{T_\infty + 120.0} \right) \left(\frac{T_\infty}{296.16} \right)^{1.5} \tag{3-21}$$

and ρ_a is the air density. The air density at a given model level is from Olson et al. (2001), and is given by

$$\rho_a = \frac{P}{R_d\left(1.0 + 0.61w\right)T_\infty} \tag{3-22}$$

Another sensitivity study is conducted to determine the effects of Sc upon the melting rate. One model run uses a constant Sc of 0.6 and another model run calculates Sc using (3-20) at each model level; both model runs hold ψ constant throughout. Figure 3-2 shows that the variable Sc causes an increase in the amount of ice melted in each model layer between the 0.2 and 0.4 km levels. As a result, the particle finishes melting in a slightly shorter distance in the variable Sc run compared to the constant Sc simulation. The change in the distance required for the ice particle to melt changes the time needed for the particle to melt which may decrease the amount of mass evaporated from the particle.

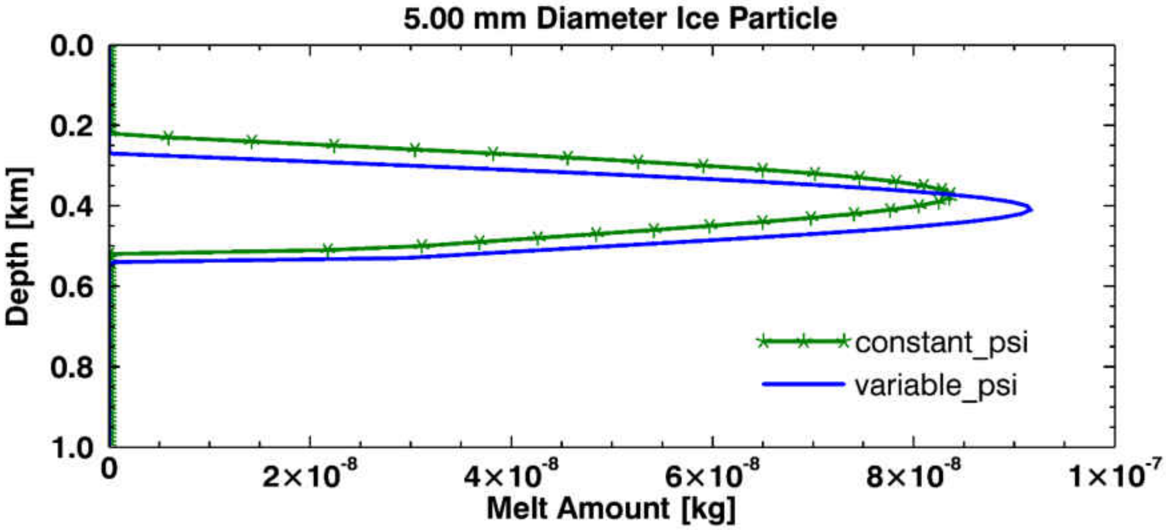

Figure 3-1: The amount of ice melted [kg] for a 5 mm diameter ice particle at each model level from a model run with constant water vapor diffusivity (green line) and the melted amount in a model run with the water vapor diffusivity calculated at each model level (blue line).

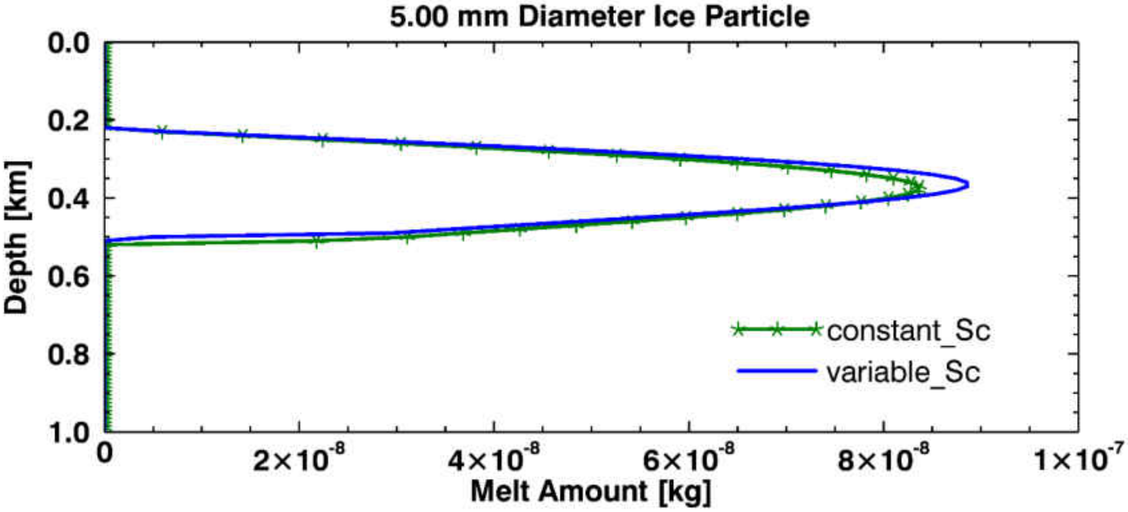

Figure 3-2: The amount of ice melted at each model level for a 5 mm diameter ice particle in a melting layer simulation using a constant Schmidt number (green line with stars) and a variable Schmidt number (blue line).

Ice Particle Temperature

In (3-6), the ice particle temperature must be computed independently, which is accomplished using

$$T_p(k,D)=\begin{cases} T_\infty-\dfrac{L_s\psi}{k_aR_v}\left[\dfrac{e_{si}(T_p)}{T_p(k,D)}-\dfrac{RHe_s(T_\infty)}{T_\infty}\right] & F_{liq}(k,D)=0 \\ 273.15K & 0<F_{liq}(k,D)<1 \\ T_\infty-\dfrac{L_e\psi}{k_aR_v}\left[\dfrac{e_s(T_p)}{T_p(k,D)}-\dfrac{RHe_s(T_\infty)}{T_\infty}\right] & F_{liq}(k,D)=1 \end{cases} \tag{3-23}$$

where $F_{liq}(k,D)$ is the fraction of liquid water to solid ice present on the ice particle, which is a function of model level and particle size. Under subsaturated conditions, the temperature of the ice particle is less than 0 °C at the top of the melting layer and thus the surface of the ice particle must warm to 0 °C before melting begins (Mitra et al. 1990). At this stage, the particle surface temperature is determined by the balance of heat gain by the ice particle from the atmosphere through conduction and heat loss through sublimation ($F_{liq}(k,D)$ = 0). Once the ice particle surface temperature reaches 0 °C, melting commences and it is assumed that the surface of the ice particle remains at 0 °C until melting has fully completed. The resulting liquid drop surface temperature is assumed to be a function of the heat balance between thermal conduction and evaporation ($F_{liq}(k,D) = 1$).

To demonstrate how the changes to the melting layer model proposed here affect the melting and evaporation rates, a small sensitivity study is conducted. One model run has the default values of T_p, Sc, and ψ held constant with values of 273.15 K, 0.6, and $2.21*10^{-5}$, respectively. A second model run calculates T_p at each model layer.

In the variable T_p simulation, the temperature of an ice particle is about -1.4 °C at the top of the melting layer for an environment with an 80% relative humidity and the particle slowly warms as it falls through the melting layer (Figure 3-3). This difference in temperature leads to more mass being sublimated away from the particles for the run with fixed particle temperature than for the variable particle temperature in the top 200 meters of the simulations (Figure 3-4). Once the particles begin to melt, the particle temperature equals 0.01 °C for both simulations. However, more mass is evaporated away from the particles in the variable particle temperature simulation because the melting particles have more mass within that simulation than for the fixed temperature simulation. Figure 3-4 also shows there are large differences in the evaporation rate between the two simulations after the particles are completely melted. This is because for the fixed particle temperature simulation, the large temperature difference between the particle and the environment allows for condensational growth to occur, while for the variable particle temperature, evaporation is occurring (Figure 3-5).

The melting rates are also impacted by the differences in particle temperature between the two simulations (Figure 3-6). The first change is that in the simulations with the variable particle temperature, melting starts 30 meters further down into the melting layer than for the simulation with fixed particle temperature. The second change is that in areas where both simulations have melting, the amount of melting in each layer is greater for the variable temperature simulation. This is because there is less sublimation higher in the melting layer in the variable particle temperature simulation, thus the particles have more mass to melt, which leads to increased melting layer rates, per (3-6).

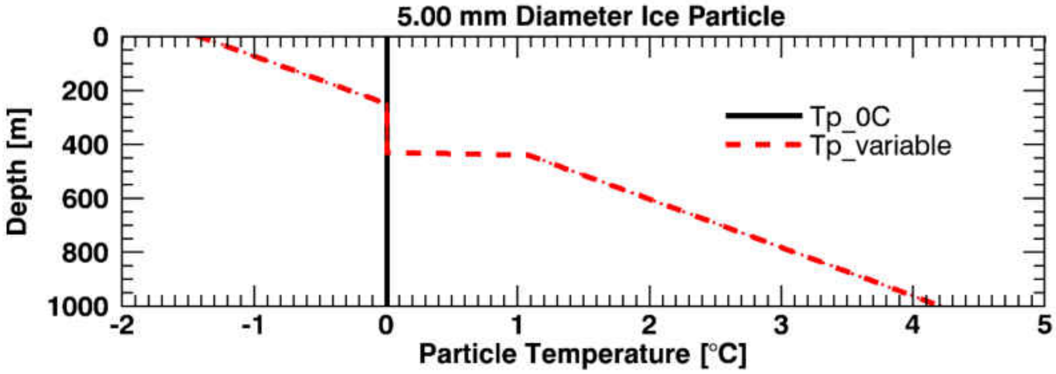

Figure 3-3: Temperature of a 5 mm diameter simulated ice particle as a function of distance from the top of the model for a model simulation holding the particle temperature constant at 0 °C (black solid line) and for a simulation computing particle temperature from (3-; dashed red line). Relative humidity is 80% and the lapse rate is 6.5 °C km^{-1} for both simulations.

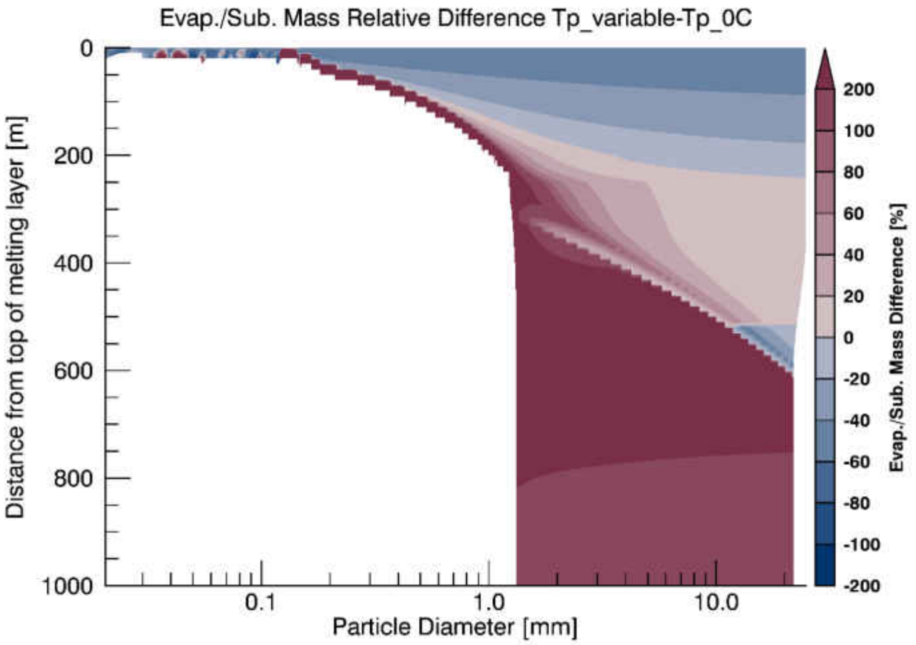

Figure 3-4: Relative difference in evaporated and sublimated mass between model runs assuming a constant particle temperature versus calculating particle temperature as a function of particle diameter and distance from the top of the melting layer model. Positive values indicate regions where more mass is evaporating/sublimating from the particles for the variable temperature run than for the constant temperature simulation.

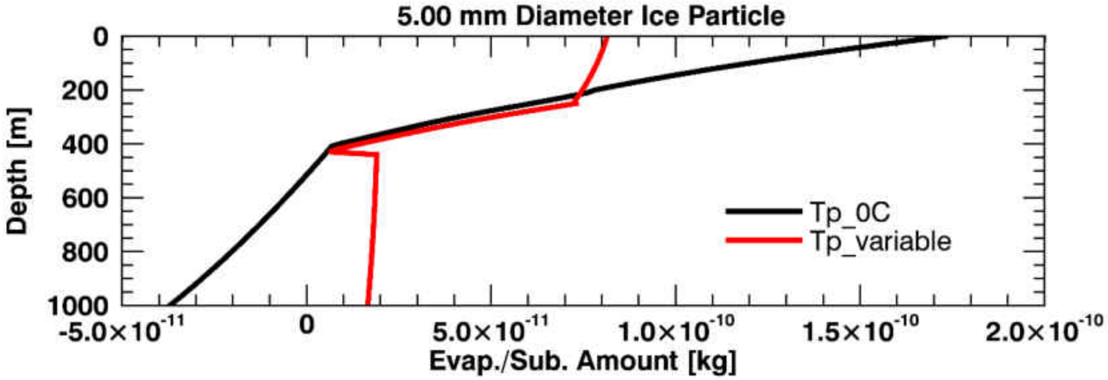

Figure 3-5: Amount of combined evaporation/sublimation amount in kilograms as a function of distance from the top of the melting layer for a 5 mm diameter particle during simulations of an idealized melting layer with a temperature lapse rate of 6.5 °C km^{-1} and relative humidity equal to 80% with the simulation holding particle temperature constant at 0.01 °C (black line) and another computing particle temperature with a heat balance equation (red line).

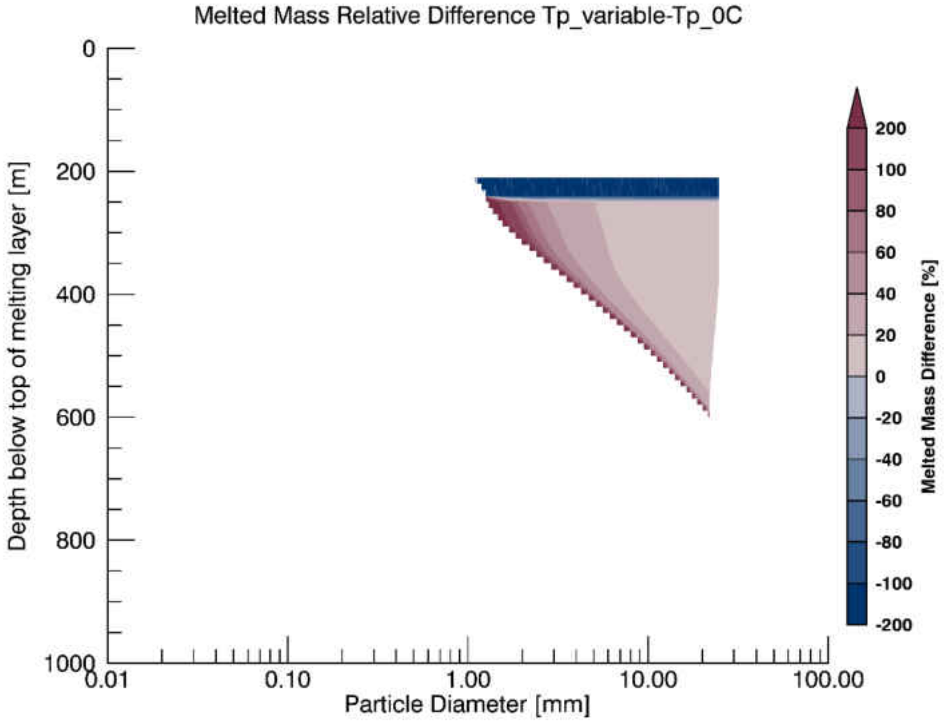

Figure 3-6: Relative difference in melted mass between model runs assuming a constant particle temperature versus calculating particle temperature as a function of particle diameter and distance from the top of the melting layer model. Positive values indicate regions where more mass is melting from the particles for the variable temperature run than for the constant particle temperature simulation.

Raindrop Terminal Velocity

The Battaglia et al. (2003) terminal velocity parameterization used in the melting layer model works well for raindrops (Figure 3-7a), but not for cloud droplets and drizzle. Figure 3-7b shows that the Battaglia et al. (2003) parameterization produces negative fall speeds for droplets smaller than 100 µm. To work around this, the model uses the ice particle fall speed if it is greater than the parameterized raindrop fall speed. The ice particle fall speed parameterization comes from Heymsfield and Westbrook (2010) and is dependent on ice particle diameter, mass, area ratio and air density. From Beard and Pruppacher (1969), the fall speed of a 100 µm drizzle drop at a pressure of 700 hPa is 0.7 to 0.8 m s^{-1} and that of a

200 µm drop is over 1.5 m s^{-1} (also shown in Figure 3-7). To obtain reasonable drizzle drop fall speeds the parameterization of the raindrop fall speed is changed from using Battaglia et al. (2003) to the Beard (1976) parameterization.

In addition to changing the terminal fall speed of liquid-phase particles, changing the raindrop fall speed parameterization changes the velocity of the melting particles. For the melting particles, the fall speed (v_t) is an average of the two fall speeds, taken from Battaglia et al. (2003)

$$v_t = \frac{F_{lmass} + F_{lmass}^2}{9.2 - 3.6\left(F_{lmass} + F_{lmass}^2\right)}\left(v_{t,rain} + v_{t,snow}\right) + v_{t,snow}, \tag{3-24}$$

where F_{lmass} is the liquid mass fraction (ratio of liquid mass to total mass), $v_{t,rain}$ is the terminal velocity from the Beard (1976) parameterization, and $v_{t,snow}$ is the terminal fall speed of an ice particle with the same equivalent diameter from the Heymsfield and Westbrook (2010) parameterization. Both $v_{t,rain}$ and $v_{t,snow}$ have been corrected for effects of air density upon the terminal velocity by:

$$v_{t,new} = \gamma v_{t,orig} \tag{3-25}$$

where $v_{t,new}$ is the terminal velocity corrected for air density, $v_{t,orig}$ is the original, non-corrected terminal velocity, and γ is given by

$$\gamma = \left(\frac{\rho_0}{\rho_a}\right)^{0.5} \tag{3-26}$$

where ρ_0 equals 1.20 kg m^{-3}.

A new pair of model runs are conducted to demonstrate the effect of using the Beard (1976) parameterization instead of Battaglia et al. (2003)/Heymsfield and Westbrook (2010).

The new runs are conducted at a RH of 95% to ensure the small-diameter ice particles that are greatly affected by the new fall speed parameterization do not sublimate away before they melt. All of the other parameters are at their default values as described in Olson et al. (2001).

The Beard (1976) parameterization simulation results in terminal fall speeds that are twice as fast as those produced with the Battaglia et al. (2003)/Heymsfield and Westbrook (2010) combination for particles that are 120 to 180 µm in diameter (Figure 3-8a). The net result of the change in terminal velocity parameterization is a 10-20% increase in the evaporative mass loss for the 150 to 180 µm diameter particles (Figure 3-8b). For particles greater than 400 µm in diameter, there is a very small positive increase in both the terminal fall speed and the evaporative mass loss.

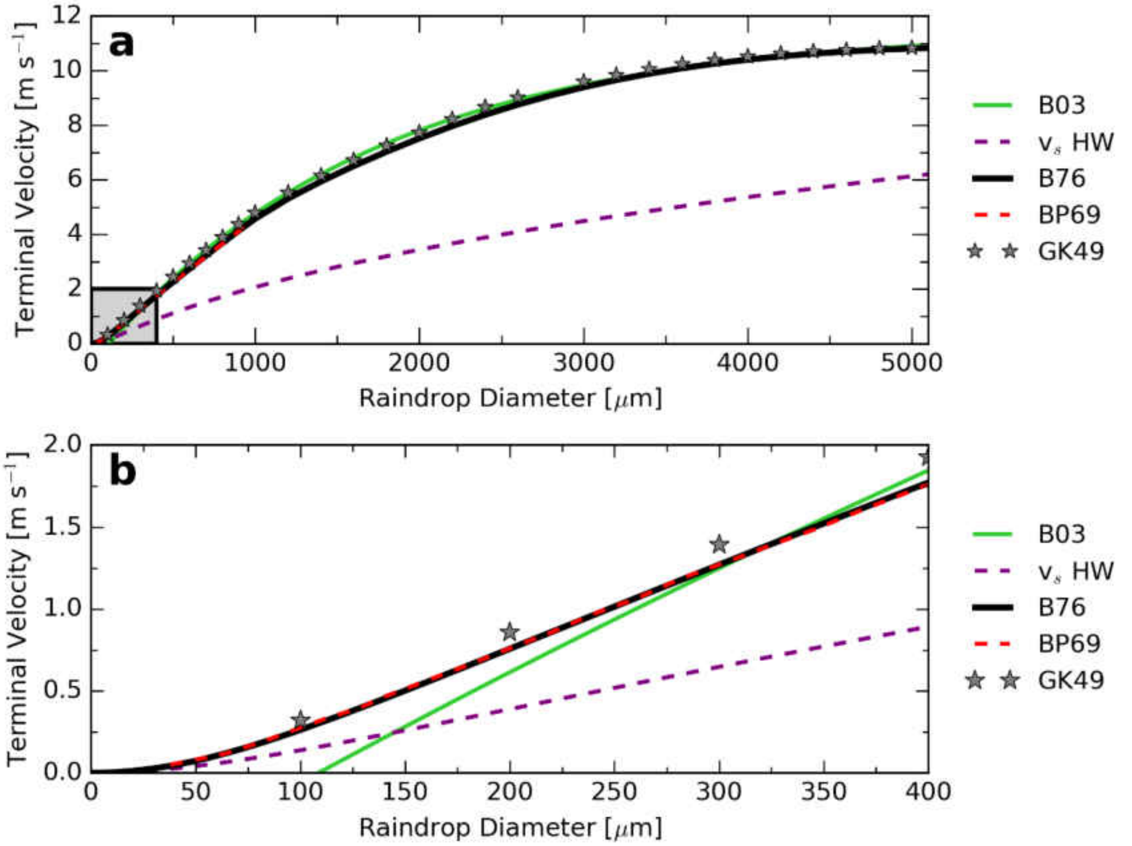

Figure 3-7: Distribution of raindrop terminal fall speeds at a pressure of 700 hPa and temperature of 287 K as a function of raindrop diameter as observed by Gunn and Kinzer (1949; stars) and Beard and Pruppacher (1969; dashed red line), the parameterizations of drizzle raindrops according to Battaglia (2003; solid green line) and Beard (1976; solid black line), and the ice particle terminal fall speed using the Heymsfield and Westbrook (2010; dashed purple line) parameterization as a function of equivalent diameter. The Gunn and Kinzer (1949) data are corrected from a density of 1.20 kg m^{-3} to a density of 0.85 kg m^{-3} by using (3-). a) For diameter range 10 µm to 5.1 mm. b) For diameter range 10 to 400 µm. Area of b) is shown as a gray box in a).

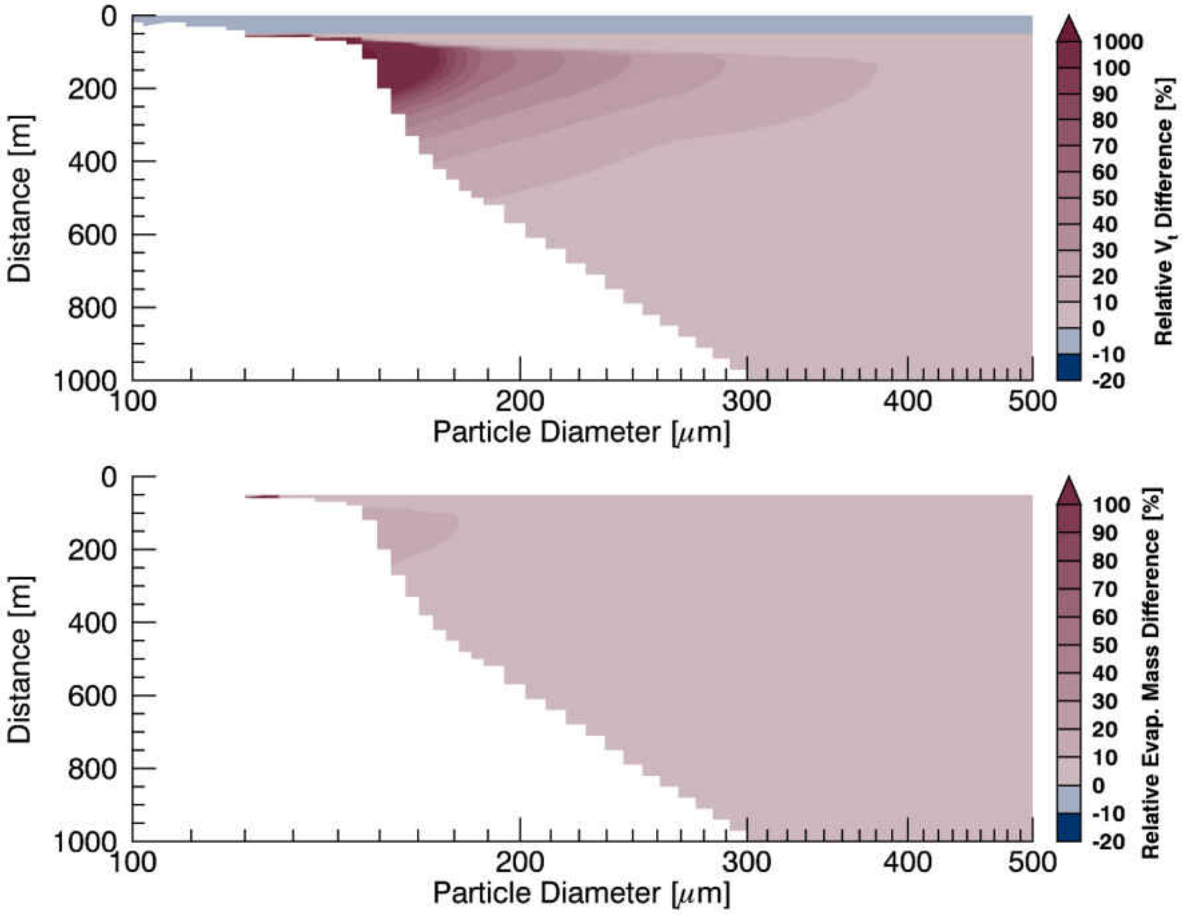

Figure 3-8: a) The relative difference in the terminal fall speed of particles as a function of particle size in millimeters and distance from the top of the model in meters for particles in the 100 to 500 µm size range. Positive values indicate the Beard (1976) terminal fall speed is greater than the Battaglia et al. (2003) fall speed. b) The relative difference in the mass evaporated as a function of particle size in millimeters and distance from the top of the model in meters for particles in the 100 to 500 µm size range. Positive values indicate where a greater amount of evaporation occurred for the simulation using the Beard (1976) terminal fall speed relation than for the simulation using the Battaglia et al. (2003) relation.

Ice Particle Mass

The melting layer model in Olson et al. (2001) is highly sensitive to initial ice particle mass. In addition to the amount of mass that needs to be melted, the Heymsfield and Westbrook (2010) ice particle fall speed parameterization is sensitive to particle mass. Initially, ice particle effective density (ρ_s) was set to a constant 100 kg m^{-3} for all particle sizes. Because the model assumes spherical particles, this density relation gives large particles too much mass, causing the simulated melting layers to be too deep. Table 3-4 shows that for an idealized melting layer profile simulation, the melting layer depth (defined as the distance between the 0 °C isotherm and the altitude in which the particle is ice-free) is over 2 km. This is three to ten times deeper than melting layers observed in the Midlatitude Continental Convective Clouds Experiment (MC3E; Jensen et al. 2015) shown in Table 3-5. The observed melting layer depth is defined as the distance between the 0 °C isotherm and the altitude in which all the particles in the in-situ imagery are all round. For more information about the rationale behind the choice of melting layer depth definition, see Chapter 4.

Table 3-4: Melting layer depths and terminal fall speeds for 2.5 cm diameter ice particles at the top of the melting layer (adjusted to an air density of 1.2 kg m^{-3}) for idealized melting layer profiles with a temperature lapse rate of 6.5 K km^{-1}, relative humidity of 100%, and aggregation/accretion/collision and coalescence processes turned off. The "Variable ρ_s" parameterization is the density-dimensional relation developed in this study.

Mass-Dimensional Relationship	Melting Layer Depth [m]	V_t (D=2.5 cm) [m s^{-1}]
ρ_s = 100 kg m^{-3}	2350	8.3
Heymsfield et al. 2013 at 0 °C	700	2.3
Variable ρ_s	430	1.3

Table 3-5: Average relative humidity and melting layer depths for observed melting layers during the Midlatitude Continental Convective Clouds Experiment.

Date	Profile Number	Average Relative Humidity [%]	Melting Layer Depth [m]
27 April 2011	1	95	429
27 April 2011	2	96	363
10 May 2011	1	69	662
10 May 2011	2	80	516
10 May 2011	3	84	200
10 May 2011	4	91	162
20 May 2011	1	86	579
20 May 2011	2	91	471
20 May 2011	3	58	593
20 May 2011	4	72	490
1 June 2011	1	66	684

The extreme melting layer depth for the ρ_s = 100 kg m^{-3} simulation results from a combination of too much ice mass to melt and from a very large terminal fall speed. Table 3-4 shows that the fall speed of a 25 mm diameter particle in the ρ_s = 100 kg m^{-3} simulation is much larger than the typical dendritic aggregate fall speeds of 1-2 m s^{-1} (Locatelli and Hobbs 1974). Heymsfield and Wright (2014) show that typical fall speed for 25 mm diameter hailstones are between 9 and 22 m s^{-1}. Thus, assuming a constant particle density of 100 kg m^{-3} does not produce ice particles that are consistent with typical stratiform precipitation regions associated with mesoscale convective systems.

The ice particle mass-dimensional (m-D) relation from Heymsfield et al. (2013) is used to replace the constant particle density assumption in the melting layer model. This m-D relation is temperature dependent and since the melting layer top is here defined as 0 °C, the m-D from Heymsfield et al. (2013) is also taken at 0 °C. For particles smaller than 30 µm, the Heymsfield et al. (2013) m-D produces a particle density greater than the density of ice (917 kg m^{-3}). These small particles are adjusted so the ice particle density equals the density of pure ice, as shown in Figure 3-9. Although this m-D relationship produced particles with reasonable terminal fall speeds, the melting layer depths are still too deep compared to observed melting layers with similar relative humidities (Table 3-4).

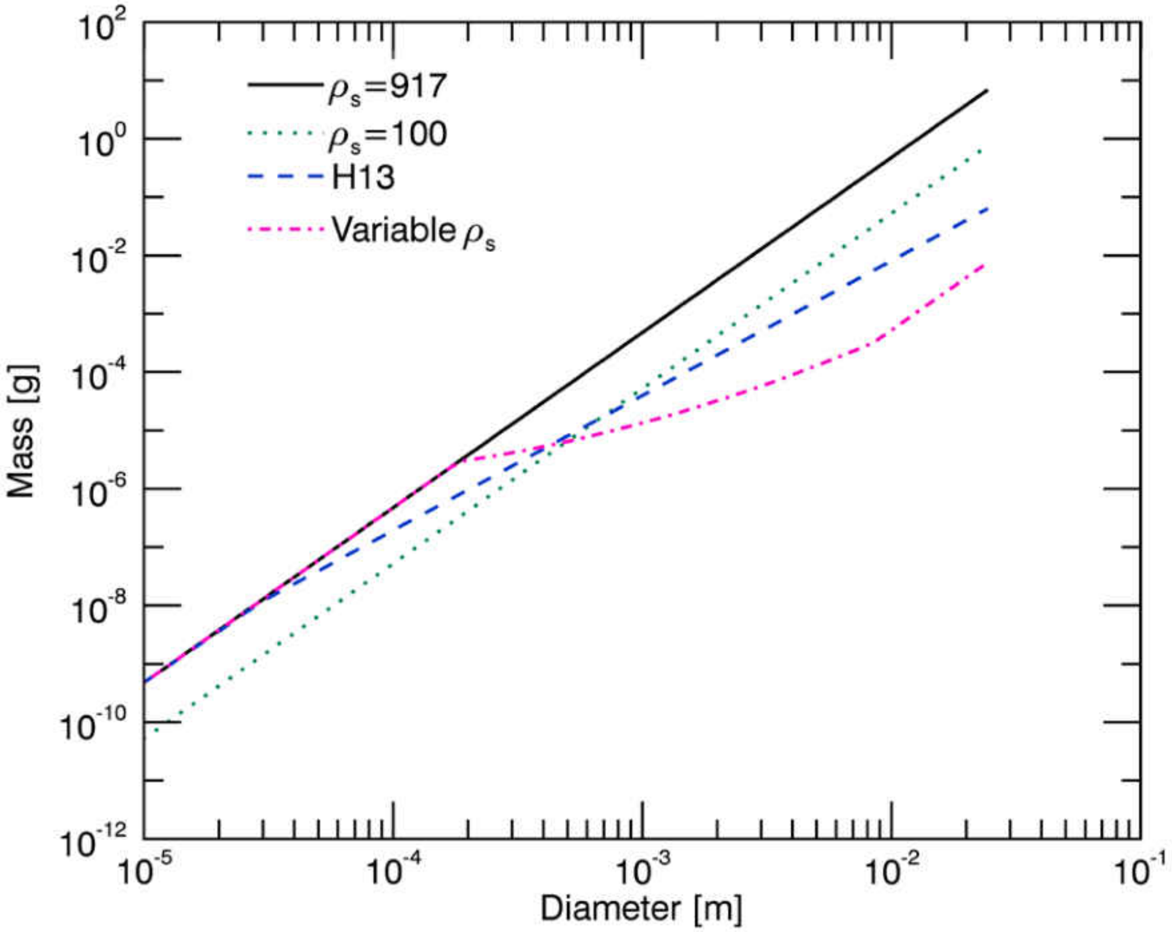

Figure 3-9: Ice particle mass in grams as a function diameter in meters for five density/mass-dimensional relations including solid ice spheres ($\rho_s = 917$; solid black line), spheres with a density of 100 kg m^{-3} (dotted green line), the Heymsfield et al. (2013) mass-dimensional relation at 0 °C (dashed blue line), and a quadratic density-dimensional relation (dash-dotted pink line).

A new density-dimensional relationship is developed by using MC3E observations and working “backwards” with the Heymsfield and Westbrook (2010) fall speed parameterization. Spectral Doppler data from the Ka ARM Zenith Radar (formerly known as the millimeter-wave cloud radar; Moran et al. 1998) at the Atmospheric Radiation Measurement Program Southern Great Plains Central Facility (Stokes and Schwartz 1994) are analyzed to determine how quickly typical snow and ice particles fall above the melting layer. From subjective analyses of these data, it is determined that a typical large aggregate falls approximately at 2.0 m s^{-1}. In-situ measurements from MC3E indicate that the largest aggregates have a maximum diameter of about 25 mm. Some aggregates exceed this size, but they are relatively rare.

Assuming that the terminal velocity spectra follows the form of $v_t\left(D_s\right)=a\log_{10}\left(D_s\right)+b$, that a 25 mm diameter particle falls at 2.0 m s^{-1}, and a 10 µm particle falls at 0.01 m s^{-1} in still air, a terminal velocity distribution is given by

$$v_t\left(D\right)=0.5856\log_{10}\left(D_s\right)+2.9382 \tag{3-27}$$

From in-situ hydrometeor image data, an average particle image area ratio can be determined, which is used in the Heymsfield and Westbrook (2010) fall speed parameterization. The hydrometeor image area ratio from is the ratio of the area of shaded pixels to the area of a minimum enclosing circle, an example of which is shown in Figure 3-11. An assumed area ratio distribution was derived from Heymsfield et al. (2015) Figure 19 at 0 °C. An inverse tangent function is fit to the area ratio data and shown in Figure 3-10; the area ratio distribution can be approximated by

$$AR\left(D_s\right)=1094.5-696.6\tan^{-1}\left(D_s*10^6+1009.8\right) \tag{3-28}$$

Equations (3-27) and (3-28) are used in a golden-section search optimization routine developed to compute the effective density and mass of the ice particles (it is assumed that all particles fit the assumed terminal velocity and area ratio distributions). From there, a quadratic function was found to best represent the density function, shown in Figure 3-12. The functions for the particle effective density and mass are given by

$$\rho_s\left(D_e\right)=10\,\hat{}\,\{0.3521\left[\log_{10}\left(D_e\right)\right]^2+0.2718\log_{10}\left(D_e\right)-0.9444\} \tag{3-29}$$

$$m\left(D_s\right)=0.0222D_s^{1.86} \tag{3-30}$$

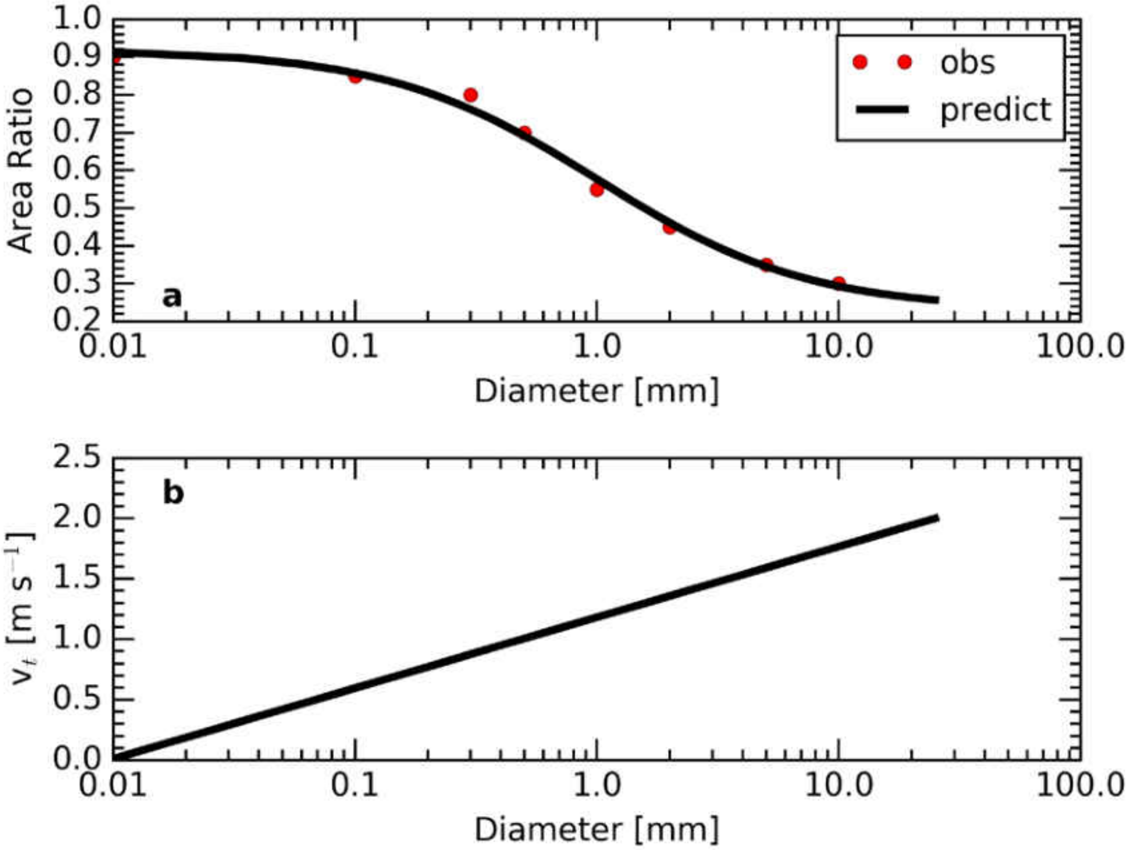

Figure 3-10: (a) Distribution of area ratio with respect to particle diameter based on Figure 19 in Heymsfield et al. (2015) at 0 °C. (b) An assumed distribution of terminal fall speeds based on Eq.(3-27).

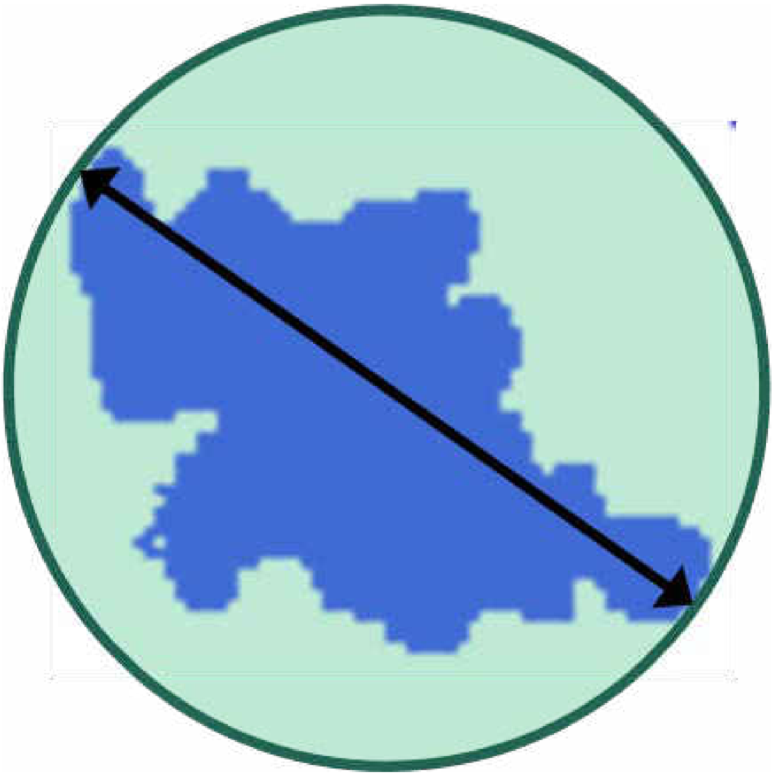

Figure 3-11: Example of a two-dimensional shadow image with the maximum dimension denoted by an arrow and within a minimum enclosing circle.

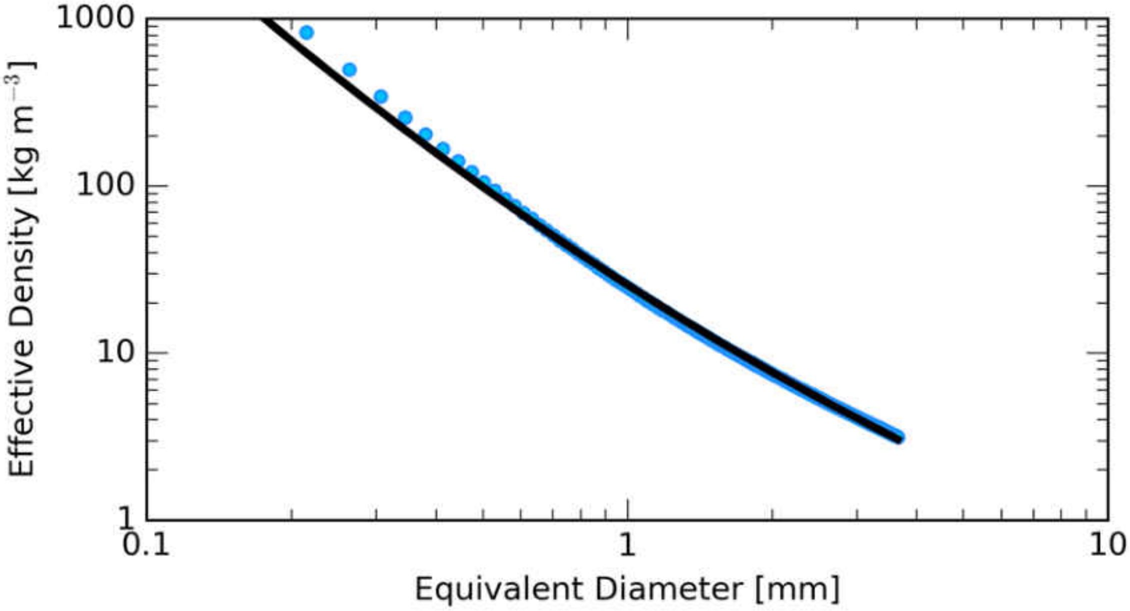

Figure 3-12: Log base-10 of the effective particle density in kg m^{-3} as a function of the log base-10 of the equivalent spherical diameter in meters.

Air Density

A sensitivity study is conducted to determine how different air densities impact the melting simulations. Three simulations are conducted using three different 0 °C isotherm altitudes of 4.6, 3.0, and 1.0 km, respectively. The reasoning for these altitudes are:

- The 4.6 km 0 °C isotherm altitude is chosen to represent the general upper-bounds of 0 °C isotherm altitudes found in the Midlatitude Continental Convective Clouds Experiment (see Chapter 5).
- The sensitivity tests in this chapter and the idealized simulations in Chapter 4 are conducted with the 0 °C isotherm set at 3 km.
- The 1.0 km altitude is chosen as the lowest altitude that is possible and still have a full 1 km deep simulation above ground level.

As in the other sensitivity tests Γ_∞ of 6.5 °C km^{-1} and RH = 80% are used. Unlike in other sensitivity tests, particle temperature varies according to (3-23) and the particle density is computed using (3-29).

One of the biggest impacts of changing the air density of the simulation is on the terminal velocities of the particles. Figure 3-13 shows that at the top and bottom of the simulations, the terminal fall speed for a 5 mm diameter particle is greatest for the 4.6 km altitude simulation and smallest for the 1.0 km altitude simulation. This is due to the lower air density at higher altitudes causing less particle drag and therefore faster fall speeds according to (3-25) and (3-26). Within the 250 to 400 m depths where all three simulations have melting particles (Figure 3-14), the 4.6 km altitude simulation has the smallest terminal velocity of the three simulations. This is probably due to the delay in the onset of melting for high-altitude particles compared to particles that melt at lower altitudes (Figure 3-14).

The melting rates are the largest in the 1.0 km altitude simulation (not shown). This is because ψ increases with decreasing air density (Table 3-3), which results in enhanced evaporation and sublimation for melting layers located at high altitudes compared to melting layers low in the atmosphere (Figure 3-15). The enhanced evaporation and sublimation increases cooling which reduces the melting rate for high-altitude particles compared to low-altitude particles. The low-altitude particles also have a slower v_t than their high-altitude counterparts, which results in low-altitude particles having larger residences times within a model layer. This results in the greatest melting amount per model layer occurring with the 1.0 km altitude simulation (Figure 3-14). The increasing melting amounts also correspond to shallower melting layer depths with increasing air density (Table 3-6).

Table 3-6: Values for air density at the top of each melting layer simulation and melting layer depth (for 2.5 cm diameter particles) within three melting layer simulations defined to start at the given 0 C isotherm altitude. the melting layer depth is defined as the smallest distance between the top of the simulation (0 °C isotherm altitude) and where the mass-weighted liquid volume fraction is greater than 0.999.

0 °C isotherm altitude [km]	Air Density at 0 °C [kg m^{-3}]	Melting Layer Depth [m]
4.6	0.68	660
3.0	0.84	630
1.0	1.18	590

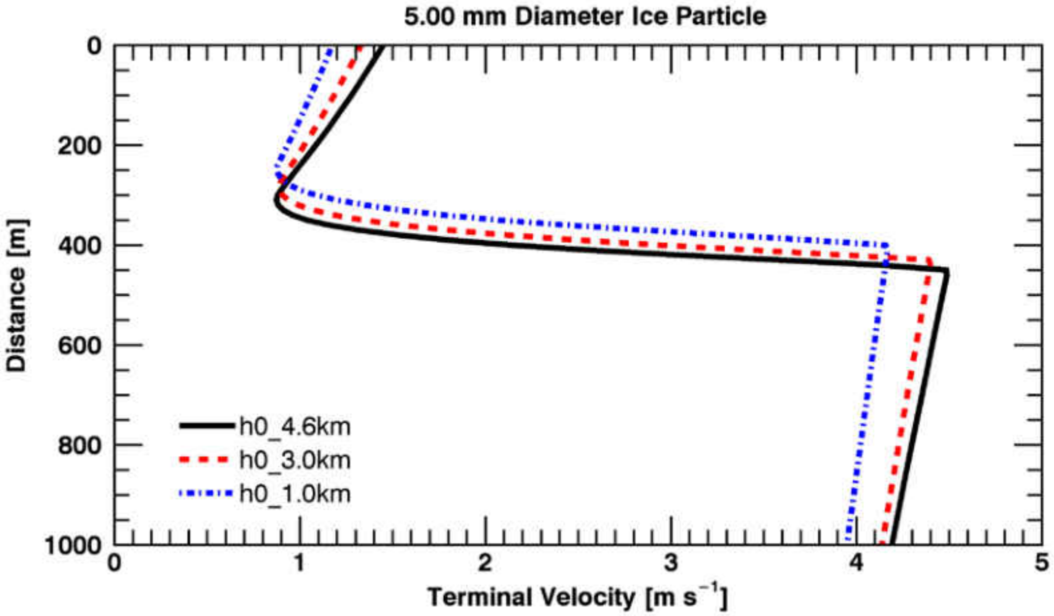

Figure 3-13: Terminal velocity of a 5 mm diameter ice particle as a function of distance from the top of the simulation domain for simulation top altitudes of 4.6 km (black solid line), 3.0 km (red dashed line), and 1.0 km (blue dash-dot line).

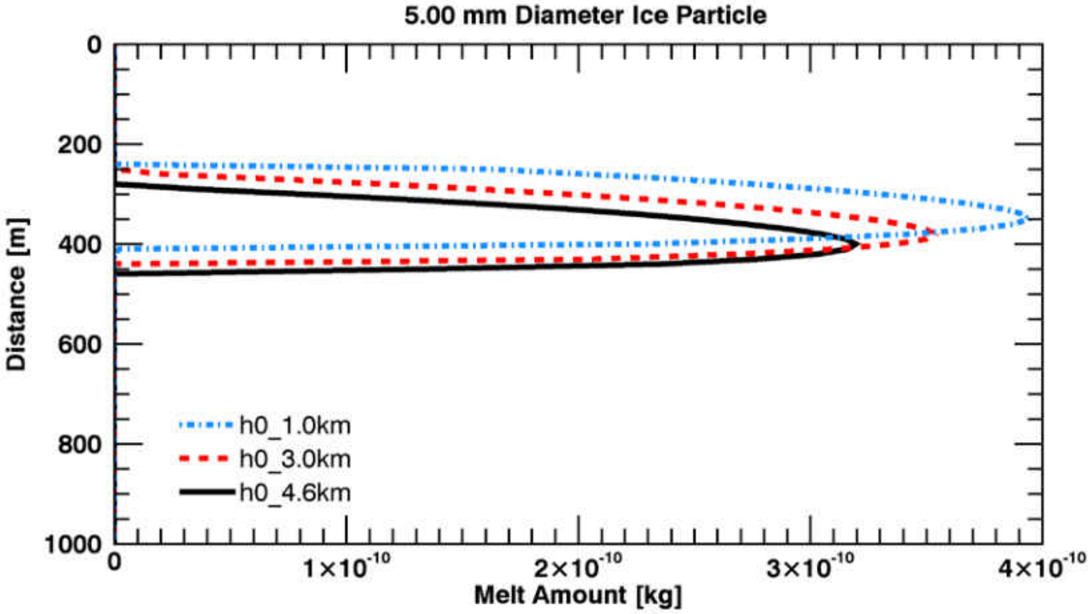

Figure 3-14: The amount of ice melted at each model level for a 5 mm diameter ice particle in a melting layer simulation with a top of simulation altitude of 1.0 km (blue dash-dot line), 3.0 km (red dashed line), and 4.6 km (black solid line).

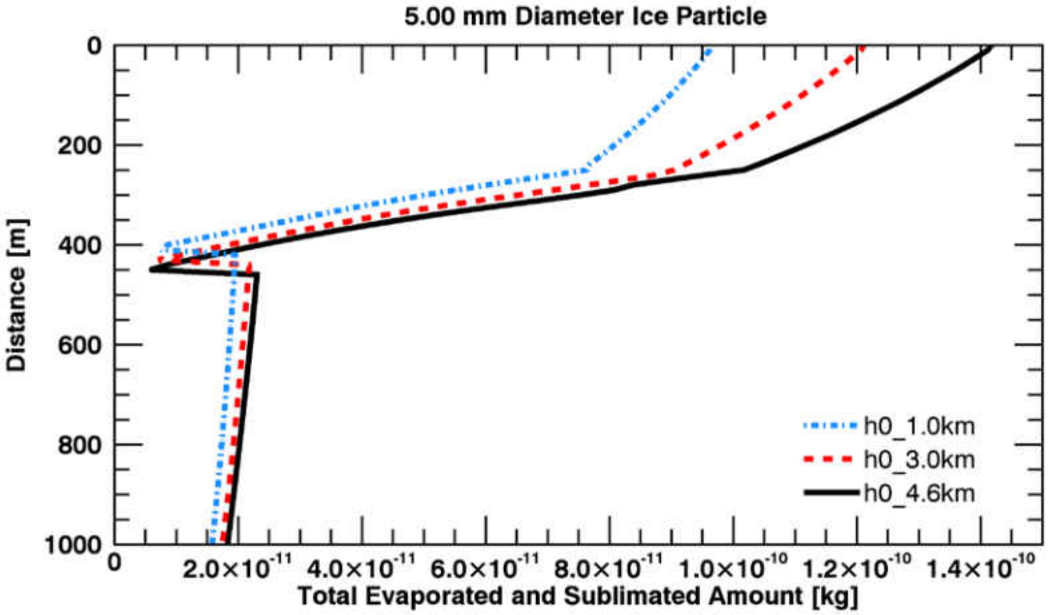

Figure 3-15: Amount of combined evaporation/sublimation amount in kilograms as a function of distance from the top of the melting layer for a 5 mm diameter particle during simulations of an idealized melting layer with a temperature lapse rate of 6.5 °C km^{-1} and relative humidity equal to 80% with the top simulation altitude of 1.0 km (blue dash-dotted line), 3.0 km (red dashed line), and 4.6 km (black solid line).

Summary and Conclusions

This chapter describes changes to make the melting layer model of Olson et al. (2001) more physically realistic. Evaporation and sublimation processes are incorporated into the melting layer model, the order in which the model looped over particle size and model layers is reversed, a particle sedimentation scheme is included, and A/A/CC processes are included. Environmental variables such as k_a, L_v, and L_f do not vary significantly within typical melting layer environments and thus are left at their default values. Other environmental variables such as ψ and Sc are changed to follow (3-19) and (3-20), respectively. Particle temperature also plays an important role, especially at the top of the melting layer where air temperatures are greater than 0 °C, but there is not enough heat transfer to overcome evaporational cooling. Thus, the particle temperature is changed from a fixed 0.01 °C to one computed using (3-23). The terminal velocity of liquid drops is changed to follow the Beard (1976) parameterization to create more realistic fall speeds for drizzle-sized drops. The melting layer model is especially sensitive to particle density, thus a new density-dimensional relationship is developed (3-29) for use in this modeling study that creates particles with realistic masses, fall speeds, and melting distances. These changes are utilized in the rest of the melting layer simulations within this study. Sensitivity studies also show the model is sensitive to changes in air density. Increasing air density within the melting layer increases the melting rates, slows down the terminal fall speeds of the particles, and reduces the evaporation and sublimation rates.

CHAPTER IV
IDEALIZED SIMULATIONS

Idealized simulations are conducted to gain an understanding of basic processes without complicating factors. In this study, the idealized simulations are of a melting layer that has no vertical air motion, a single temperature lapse rate, constant relative humidity, and constant influx of ice particles at the top of the model. Aggregation, accretion, and collision and coalescence are also omitted from the idealized simulations to further simplify the effects of evaporation within the melting layer upon the particles.

Thirty-three simulations of melting layers with constant RH profiles are used in this study. The range of RH covered by these simulations is 20% to 100% with increments of 2.5% from simulation to simulation. In actuality, the temperature lapse rate through the melting layer may have some dependence upon the relative humidity; however for this study, the temperature lapse rate and the relative humidity are assumed to be independent of one another. Other than changing the RH of the profile, all other input parameters remain the same, with details given in Table 4-1. Results of calculations within the model are saved every 12000 time steps (10 minutes of simulation time) and the results at 30 minutes of simulation time are presented here. Discussion includes details on whether ice and snow particles lose a significant amount of mass due to evaporation while melting and why this occurs. In addition, the effects of sublimation and evaporation upon the particle size distribution are described.

Table 4-1: Values and units of the melting layer model parameters including the number of model layers, individual model layer depth (Δz), number of simulation time steps, simulation time step (Δt), number of particle size bins, equivalent spherical diameter bin width (ΔD_e), the number concentration distribution (*n(D)*), the density distribution ($\rho_s(D_e)$), the temperature lapse rate (Γ_∞), the altitude of the zero degree isotherm (*h₀*), and the idealized air pressure profile. T_{surf} and P_{surf} are the air temperature and pressure at the Earth's surface, respectively, while *H* is the scale height of the atmosphere.

Parameter	Value	Unit
# model layers	101	None
Δz	10	m
# model time steps	36000	None
Δt	0.05	s
# diameters	300	None
ΔD_e	$1.21*10^{-5}$	m
n(D)	$2.39*10^{-7} D^{-1.0377} \exp(-4.9432D)$	cm^{-3}
$\rho_s(D_e)$	$10 \wedge \left\{0.3521\left[\log_{10}(D_e)\right]^2 + 0.2718\log_{10}(D_e) - 0.9444\right\}$	kg m^{-3}
Γ_∞	6.5	°C km^{-1}
h₀	$\frac{T_{surf}}{\Gamma_\infty}$	m
P	$P_{surf} \exp\left(\frac{-h_0}{H}\right)$	Pa
T_{surf}	19.5	°C
P_{surf}	970.0	hPa
H	7729	m

Results and Discussion

Figure 4-1 shows that sublimation before melting and evaporation after melting decrease particle mass. Sublimation removes small particles before melting begins and decreases the mass contained within the remaining particles. The minimum diameter at which particles "survive" sublimation increases with decreasing relative humidity (Figure 4-1a). All particles sublimate away in environments with RH less than 50%. After melting is complete, evaporation continues to remove mass from the resultant raindrops within environments with RH less than 95% (Figure 4-1c). In near-water-saturated conditions, water vapor condenses upon the particles throughout the melting process and continues to do so after melting is complete.

Particles do lose a significant amount of mass while melting under certain conditions. Figure 4-1b shows that sub-millimeter-size particles lose over 10% of their mass (considered the threshold for significant mass loss in this study) in environments with relative humidities as high as 90%. However, the largest particles (initial diameters greater than 10 mm) do not experience a 10% mass loss during evaporation until the environmental relative humidity is less than 80%. In near-water-saturated environments, water vapor condenses upon the melting particles, causing them to gain a small amount of mass while melting (Figure 4-1b). The relative humidity at which particles either have a net gain or loss of mass while melting is particle size dependent.

The relative evaporative mass loss during melting is somewhat constrained when compared to the relative mass loss due to evaporation and especially when compared to the relative mass loss due to sublimation. There are two main reasons for this: delay in the onset of melting after the particle falls below the 0 °C isotherm and a short amount of time the particles are melting compared to how long they spend sublimating and falling within the model after melting is complete.

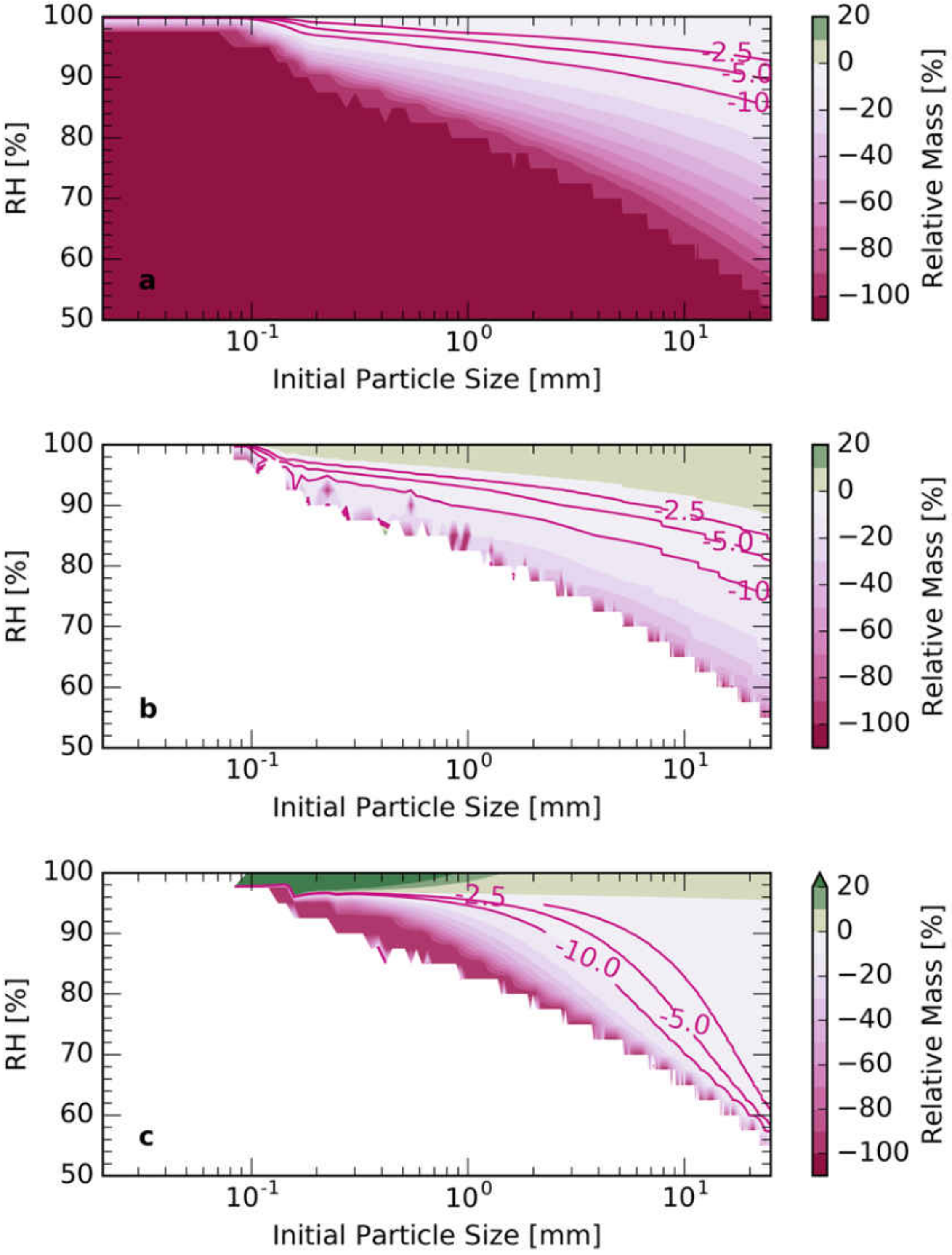

Figure 4-1: Relative particle mass change from a) sublimation before melting, b) evaporation during melting c) evaporation after melting as a function of initial particle size and relative humidity. Negative values indicate conditions where particles lost mass. The -10% relative mass change contour is highlighted for clarity.

Delay in the Onset of Melting

In subsaturated conditions, melting does not begin immediately once particles fall into air that has temperatures greater than 0 °C. Cooling from sublimation keeps the particle surface temperature below 0 °C until there is enough heat from the surrounding air conducted onto the particle surface to warm it until it reaches 0 °C and melting begins (Fig. 3-3). The ice-bulb temperature, which is defined as the temperature an air parcel would have if cooled adiabatically to saturation at constant pressure by sublimation of ice into it (American Meteorological Society 2016), is a very good approximation to the surface temperature of an ice particle. Melting on the ice particle surface starts when the ice-bulb temperature of the environment is greater than 0 °C.

In near-water-saturated environments (RH > 90%), a relatively small difference in temperature between the environment and the particle is required to overcome the small amount of evaporative cooling that occurs and thus the particles only fall a short distance before melting starts (Figure 4-2). In more subsaturated profiles, a larger environment-particle temperature difference is required in order to overcome evaporative cooling and warm the particle to 0 °C. This means that the particles fall further into the above-freezing air mass until they encounter a sufficiently large temperature difference to begin melting. The greater the degree of subsaturation, the further the particles must fall before melting can begin (Figure 4-2).

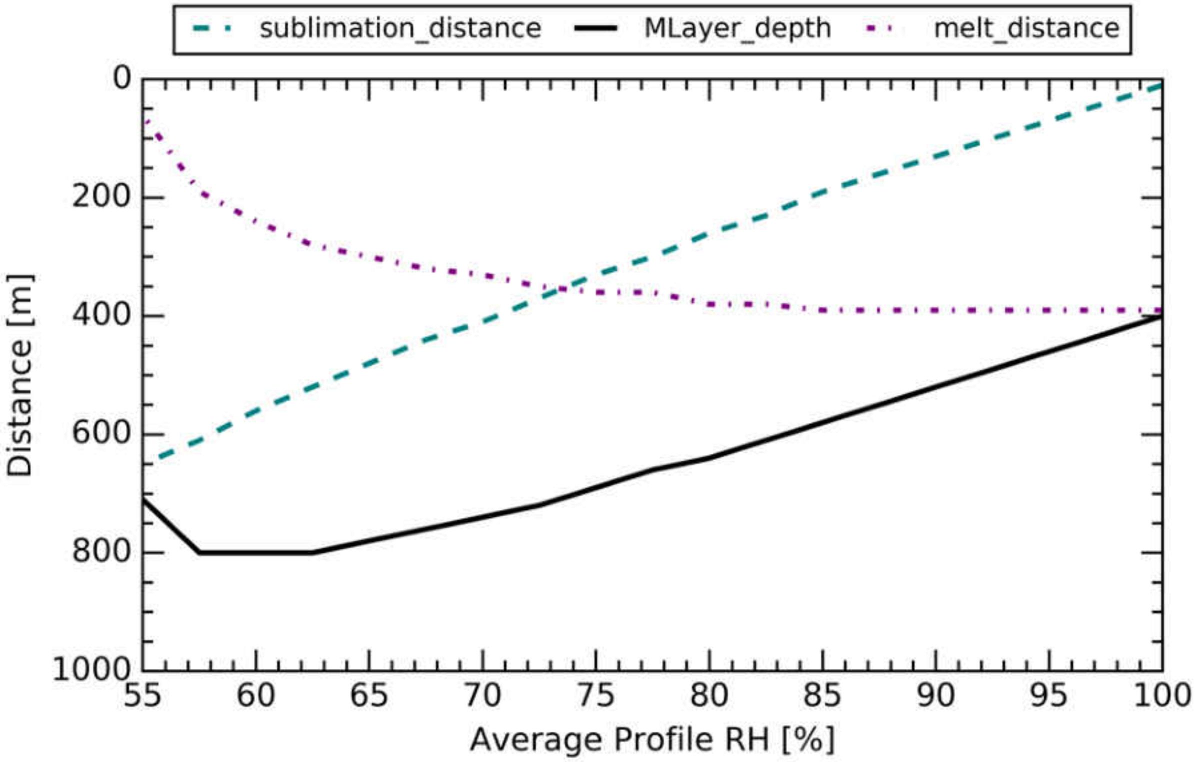

Figure 4-2: Total melting layer depth (solid line), distance from 0 °C until melting begins (dashed line), and maximum distance melting particles fall while melting (dashed-dotted line).

Melting Residence Time

The residence time (τ) of the particles within the melting layer model is determined from the particles' fall speeds and is given by

$$\tau(D) = \sum_{k=1}^{K} \frac{\Delta z}{v_t(D)} \qquad (4\text{-}1)$$

where *k* is the model layer number and *K* is the total number of model layers. (4-1) is used to calculate the residence time of three regions: when particles are undergoing sublimation after falling below the 0 °C isotherm and before melting has begun (defined as when the liquid volume fraction, F_l is less than 0.0001), during melting (0.0001 ≤ F_l ≤ 0.9999), and after melting (F_l > 0.9999). This defines "dry" ice and snow particles as containing less than 0.01% liquid water by volume and fully melted drops as containing more than 99.99% liquid water by volume. Figure 4-3 shows that except for those particles that evaporate completely while melting, most particles spend equal or less time melting than they do sublimating. There are two main reasons for this: 1) particles have a slower average v_t before melting compared to while melting and 2) in low-RH environments particles fall further while sublimating than while they do melting within the simulations.

The initial mass-weighted mean v_t within the idealized simulations is 1.3 m s^{-1}, which is slower than the 3.5 to 5.0 m s^{-1} mass-weighted mean v_t the particle distributions have by the time all particles finish melting (Figure 4-4). In addition, in sub-saturated environments most particles experience a decrease in v_t between the top of the model domain and where melting starts (Figure 4-5). This difference in v_t increases as the RH of the environment decreases, due to the increased amount of mass removed via sublimation from the particles (Figure 4-1). The reduction in v_t due to sublimation lengthens the time required to fall into air warm enough for melting to start which adds to the time during which particles undergo sublimation. On the other hand, Figure 4-5 shows that the largest particle sizes in the highest RH environments appear to have a slightly increased v_t as they fall before melting, which is likely due to increased particle mass from depositional growth.

Besides mass removal due to sublimation, the v_t also decreases slightly as the particles descend due to the increased air density and increased drag upon the particles, but this is minor compared to the effect sublimation and evaporation have upon the particles. There is a 5% total reduction in v_t due to the increase in air density between the top of the model to the bottom (not shown). Therefore, most of the reduction in particle v_t comes through the sublimation mass loss and not the change in the air density. The reduction in v_t due to drag is nearly constant across the spectrum of profile RH values in this study, but will vary depending on the air pressure profile

In contrast to the sublimation part of the melting layer, the mass-weighted mean v_t, as well as most individual particle v_t, increase drastically while melting (Figure 4-4). As particles melt, the low-density ice is converted into high-density liquid water and the particle size decreases. With a smaller particle size, the frictional drag upon the particle is less and thus the particle falls faster. While the cloud-sized particles (those particles with diameters initially less than approximately 500 μm) do not demonstrate much change in v_t due to their already dense initial composition, the large, low-density particles undergo a larger increase in v_t than what is shown in Figure 4-4 (not shown). With the higher v_t, the particles more quickly fall into higher air temperatures, which in turn leads to increased melting rates (Figure 4-6) and faster melting than if the particle v_t remained constant.

For profiles with RH less than 73%, particles fall further while sublimating before melting begins than they fall while melting (Figure 4-2). The lower the environment RH, the higher temperatures need to be to impart enough heat to a particle to overcome cooling from sublimation and begin melting. Thus, the particles need to fall further into the melting layer to where the environmental temperature is high enough to offset the sublimational cooling and begin melting. Additionally, sublimation removes mass prior to melting; then once melting starts, there is less mass to melt and thus melting completes faster and over a shorter distance compared to a similar-sized particle that does not encounter as much sublimation. Therefore, with decreasing RH the distance traveled by the particles while sublimating increases and in the low-RH environments, the distance traveled via sublimation is greater than the distance traveled while melting.

In summary, particles do lose a significant amount of mass due to evaporation while melting in conducive conditions. In high RH environments particles experience little to no evaporational mass loss, but in low RH environments (RH between 50% and 90%) significant mass loss due to evaporation can occur. The evaporative mass loss during melting is curtailed somewhat compared to the sublimation mass loss because of the following reasons:

- In low-RH environments, there is a delay between when particles fall below the 0 °C isotherm and when they begin to melt. During this time, particles undergo sublimation. The time particles spend sublimating is often equal to or greater than the time spent melting. Particle v_t is low while sublimating compared to when melting, contributing to the longer time spent sublimating rather than melting. In environments with RH less than 73%, particles fall further while sublimating than they do while melting, also contributing to the increased time spent sublimating rather than melting.
- In very low-RH environments, particles often sublimate away prior to melting. Those particles that do survive to the melting stage have experienced heavy mass loss and therefore have little ice left to melt, creating small melting times in which little mass can be evaporated.

These results show the effects of evaporation upon individual particles; the next section describes the effects of evaporation upon the whole of the particle size distribution as the particles fall through the melting layer.

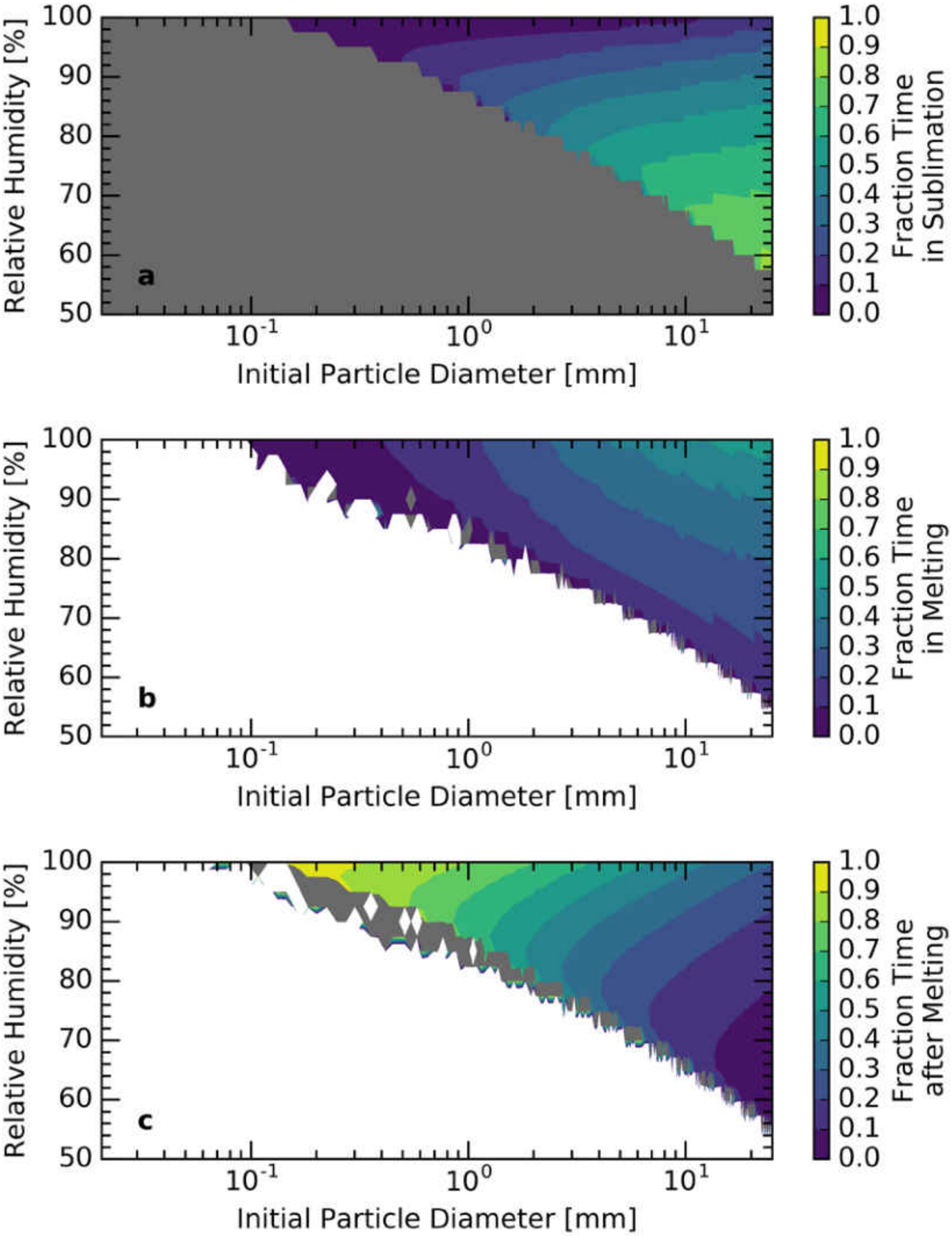

Figure 4-3: Time ice particles spend undergoing a) sublimation when below the 0 °C isotherm and before melting begins, b) melting, and c) evaporating after the particles have finished melting and before the particles fall out of the bottom of the model domain as a function of relative humidity and the initial particle diameter. Gray shaded areas denote where particles evaporate/sublimate completely.

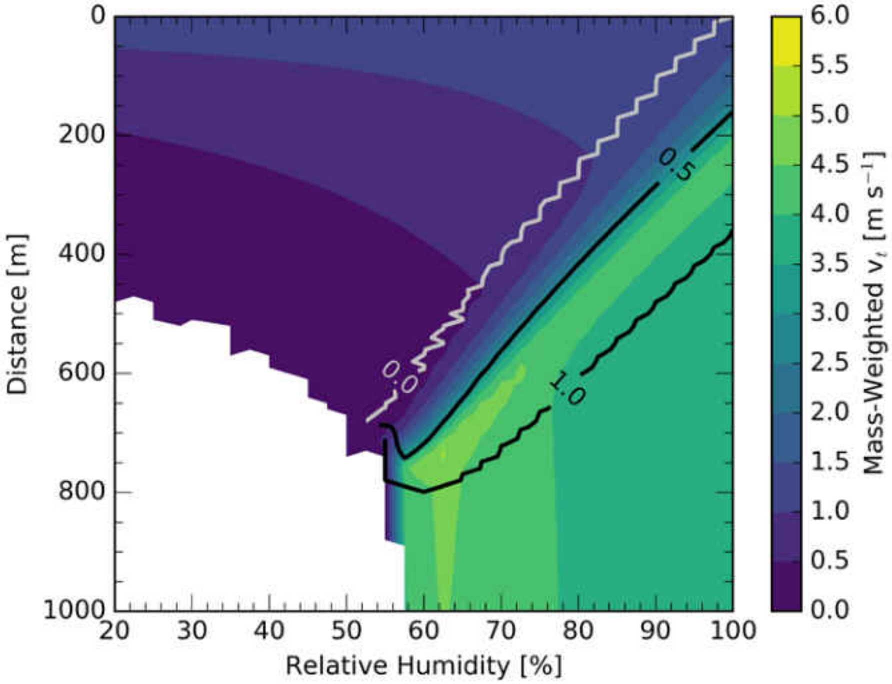

Figure 4-4: The mass-weighted mean terminal velocity of particles within idealized melting layer simulations as a function of environment relative humidity and distance from the top of the model. Mass-weighted mean liquid volume fraction is overlaid at levels of 0.0001 (black), 0.5 (dark gray), and 0.9999 (light gray).

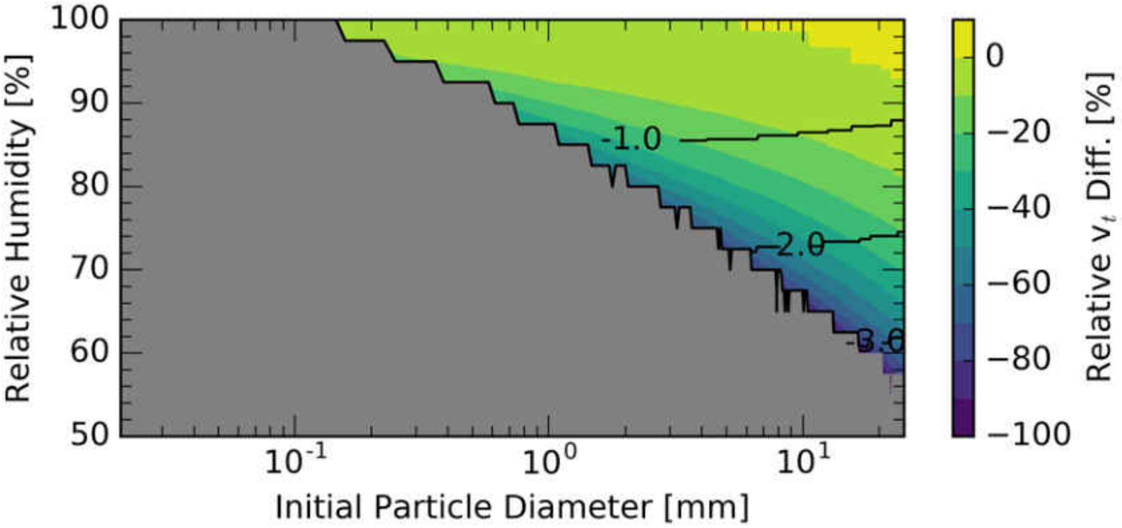

Figure 4-5: Relative change in particle terminal velocity (v_t) before melting starts (color) in idealized melting layer simulations as function of particle size and profile relative humidity. Black contours denote the relative decrease in v_t due to air density and gray shaded area denotes where particles sublimated completely before melting begins.

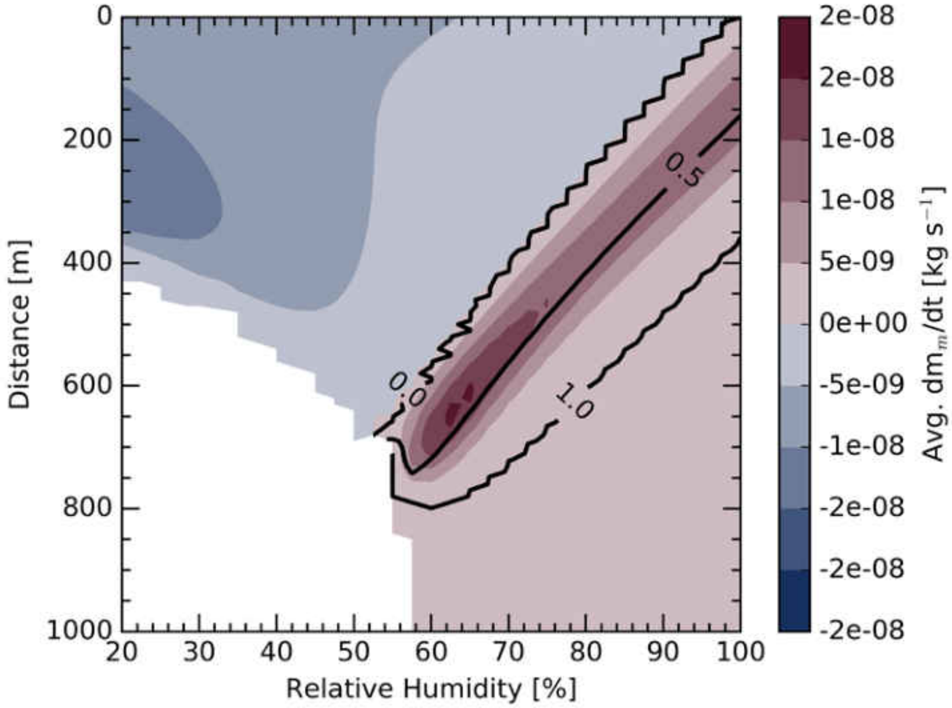

Figure 4-6: The mass-weighted mean melting rate [kg s^{-1}] as a function of relative humidity [%] and distance from the top of the melting layer [meters]. The red contour denotes where the mass-weighted mean melting rate is equal to zero kg s^{-1}. The mass-weighted mean liquid volume fraction at 0.0001 (black), 0.5 (dark gray), and 0.9999 (light gray) are overlaid.

Mass-Weighted Mean Melting Rates

The maximum mass-weighted mean instantaneous melting rates are found about midway through the melting process for each simulated melting layer profile in which melting occurs (Figure 4-6). This results from a combination of the compensating factors of the increasingly large temperature difference between the particle and the air and the decreasing particle diameters as particles fall through the melting layer. As the difference between the air and the particle temperatures increases, so does the amount of heat imparted to the particle from the atmosphere via conduction. As melting progresses mass is converted from ice to liquid water. Since liquid water has a greater density than ice, the particles' volume decreases as the particles melt, which in turn results in decreasing particle diameter. The model has an assumption of fixed effective density for ice for each particle size, which means there is a specified ratio of air-to-ice volume within the simulated particles. When the ice mass decreases, the volume of air also decreases proportionally with the particle ice volume, which further reduces particle diameter.

The overall maximum mass-weighted mean melting rates occur within the 60-70% RH profiles (Figure 4-6). This is fairly well correlated with trends seen in the mass-weighted mean diameter (Figure 4-7). In the 60-70% RH profiles, particles undergo sublimation for a relatively long period of time (Figure 4-3a), which leads to particles as large as several millimeters in diameter sublimating away prior to melting (Figure 4-1a). This moves the mean mass of the distribution to larger sizes compared to the distributions found within the high RH environments (Figure 4-7). Thus when melting starts, the low-RH profiles have only large particles left to melt, and the large *D* leads to large $\frac{dm_m}{dt}$ as shown in (1-6).

Changes in IWC/LWC/TWC

Figure 4-8 shows that the TWC decreases by at least half of the initial TWC value between the top and bottom of the melting layer in all simulations. In the very low RH profiles (RH < 50%), sublimation removes all of the particle mass before the particles can melt (Figure 4-1a). Evaporation also removes mass from the particles after melting has completed for subsaturated profiles (50% ≤ RH < 95%; Figure 4-1c). For at or near water-saturated profiles (RH ≥ 95%) condensation is taking place and the particles are growing slightly (Figure 4-1c), which in turn increases the LWC with respect to increasing distance from the top of the melting layer (Figure 4-8c).

Sublimation removes a large amount of the ice mass within the particle distribution in mid- to low-RH environments (RH less than 75%; Figure 4-9a), which causes a drastic decrease in the IWC with increasing distance from the 0 °C isotherm (Figure 4-8b). Small particles sublimate away and reduce the N_t (Figure 4-10) with increasing distance into the melting layer. The rainfall rate also decreases with increasing height in the sub-saturated profiles due to sublimation. Figure 4-11 shows that the rainfall rate decreases slightly when melting is occurring and after melting has finished, but the bulk of the mass flux reduction occurs before melting where sublimation occurs. Thus the bulk of the mass removal from the particle distribution is from sublimation prior to melting rather than from evaporation while melting.

Even in the water-saturated and nearly water-saturated profiles the maximum LWC is a little over 0.20 g m^{-3}, which is less than half of the input water content. Condensation of water vapor upon the raindrops increases the rainfall rate near the bottom of the simulation (Figure 4-11) and increases the LWC in that region slightly (Figure 4-8c).

There is some numerical diffusion within the sedimentation scheme that affects the number concentration of the particles. Within simulations with RH equal to 95% and that do not include evaporative mass loss, the effect of the numerical diffusion problem is about a 2-3% loss within the rainfall rate when the particles are melting and undergoing a rapid transition from slow to fast fall speeds (Figure 4-12d). The reduction of the rainfall rate as a result of the numerical diffusion is constant within simulations that do not include evaporative mass loss (not shown). N_t decreases both as a result of model numerical diffusion and as a result of the nearly constant rainfall rate. To maintain a constant rainfall rate in the melting regions of the profile when particle mass remains constant, (4-2) shows N_t must decrease to counteract the increasing particle v_t during melting.

$$R = \sum_{i=1}^{Nbins} \frac{\pi}{6} n(D_i) v_t(D_i) D_i^3 \left(\frac{1000mm}{m}\right)\left(\frac{3600s}{hr}\right). \tag{4-2}$$

The maximum amount of LWC in the profile is less than half of the input TWC because of the decrease in N_t. Figure 4-12b shows that the LWC the distribution would have if all size bins had a concentration of 1.0 m^{-3} increases while melting is occurring, but does not change once melting completes for a simulation with evaporative mass loss turned off. This shows that particle mass is conserved when there is no condensation or evaporation and the model is not arbitrarily changing particle mass. The LWC that accounts for the variable $N(D)$ is a function of the increasing water content within the particles as particles fall further into the melting layer and melt and the decrease of $N(D)$ due to conserving the rainfall rate and numerical diffusion. The decrease in N_t is why the LWC peaks at less than half of the value of the input TWC and also decreases slightly before reaching a constant value in the absence of condensation and evaporation (Figure 4-12a).

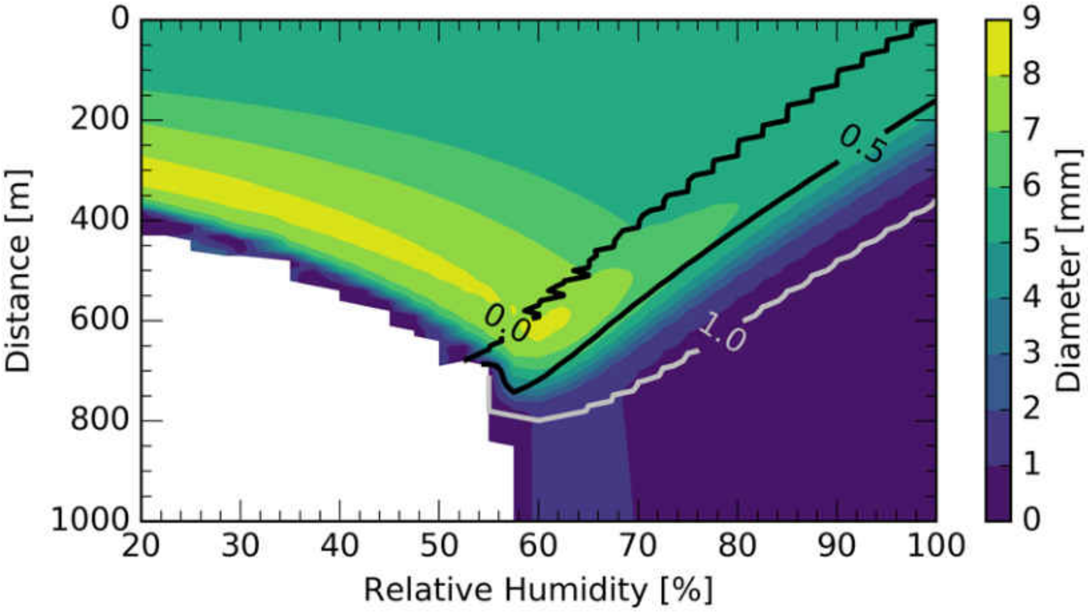

Figure 4-7: Mass-weighted mean diameter of particle distributions within melting layer simulations as a function of simulation profile relative humidity and distance from the top of the melting layer model (color). Mass-weighted mean liquid volume fraction is overlaid at 0.0 (black), 0.5 (dark gray), and 1.0 (light gray) contours.

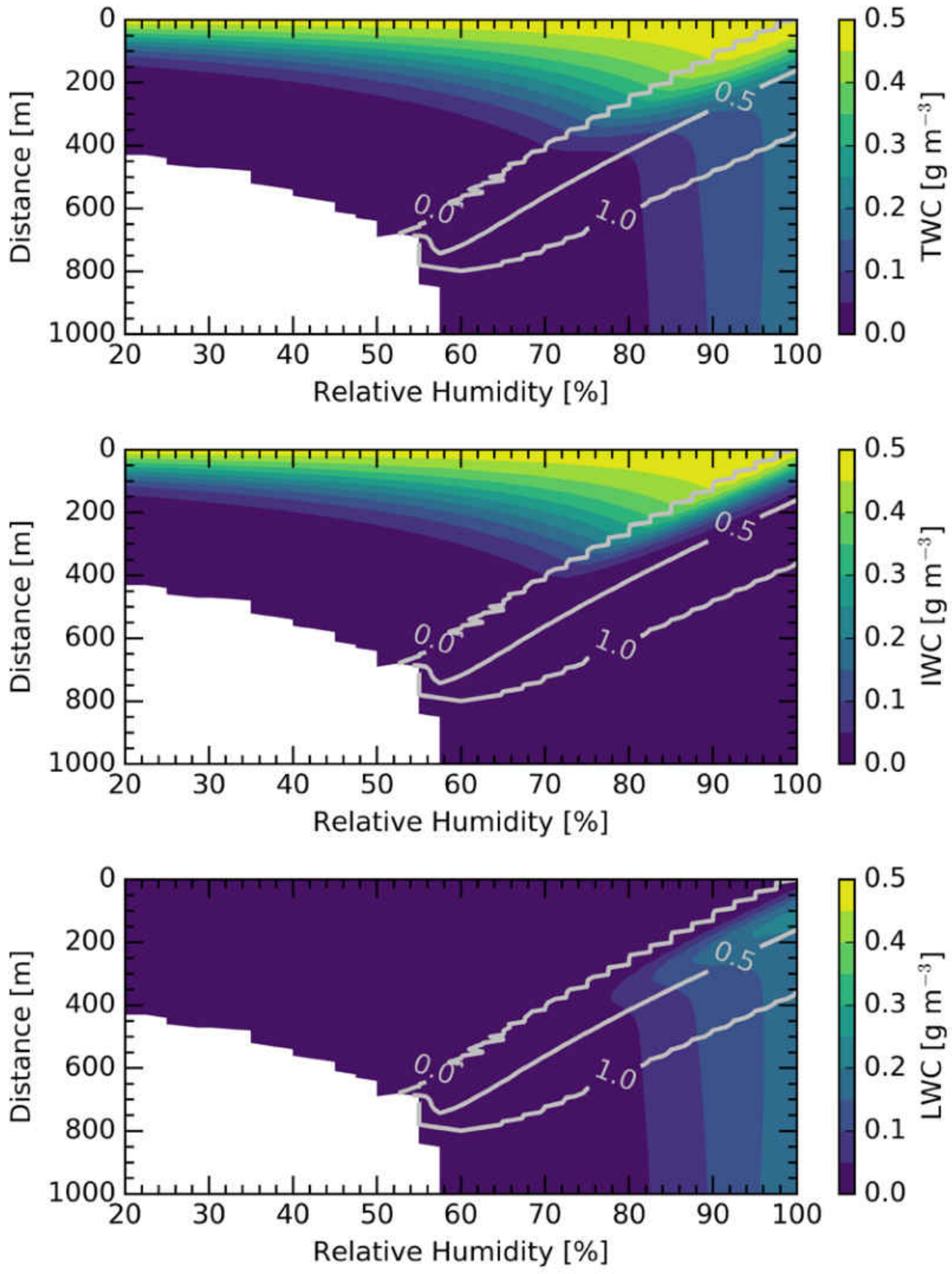

Figure 4-8: The a) total condensed water content (TWC), b) IWC, and c) LWC as a function of profile relative humidity in percent and distance from the top of the melting layer model in meters (color). Mass-weighted mean liquid volume fraction is overlaid at 0.0 (black), 0.5 (dark gray), and 1.0 (light gray) contours.

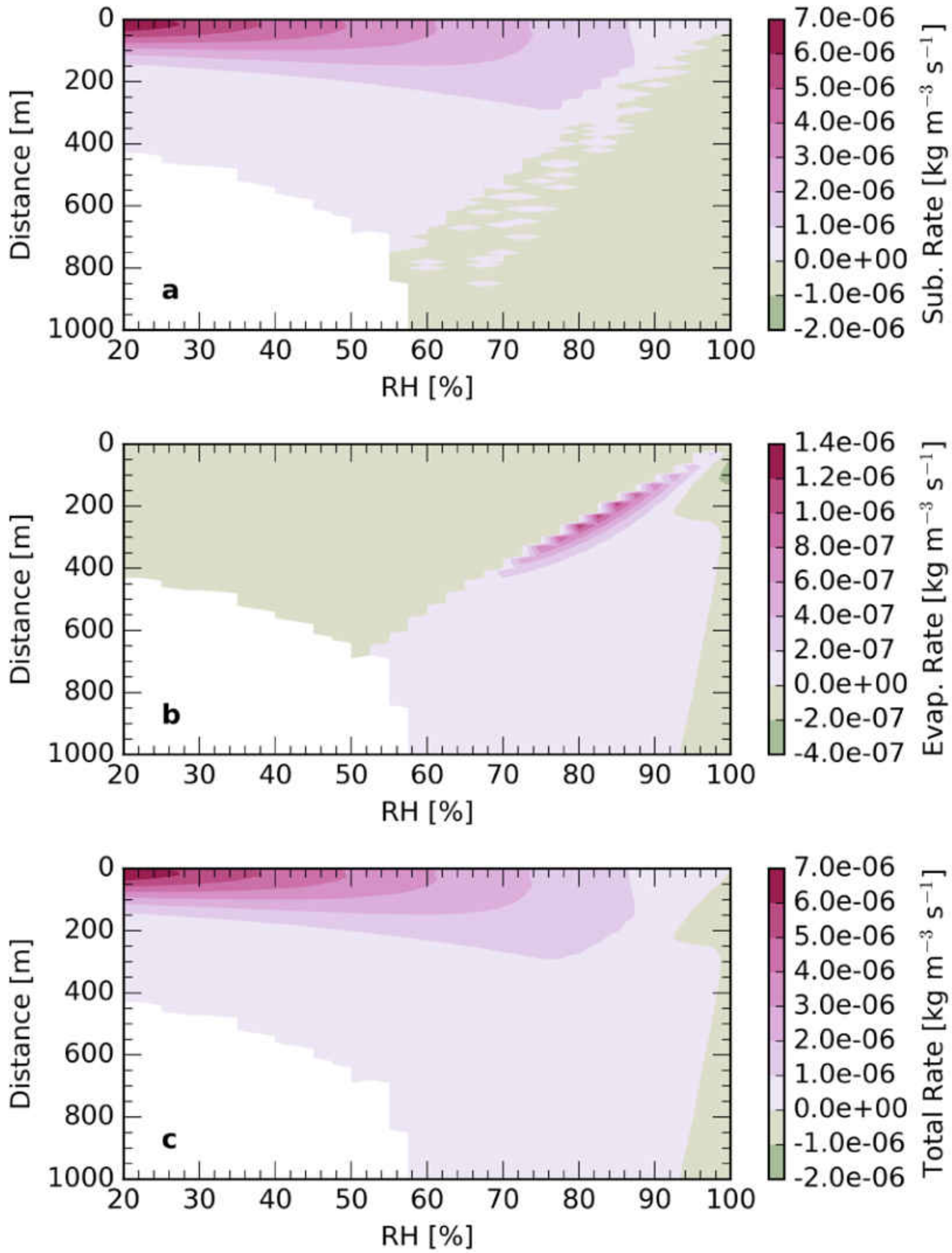

Figure 4-9: a) Total sublimation rate, b) total evaporation rate, and c) combined total evaporation and sublimation rate [kg m^{-3} s^{-1}] as a function of profile relative humidity [%] and distance from the top of the simulation [meters].

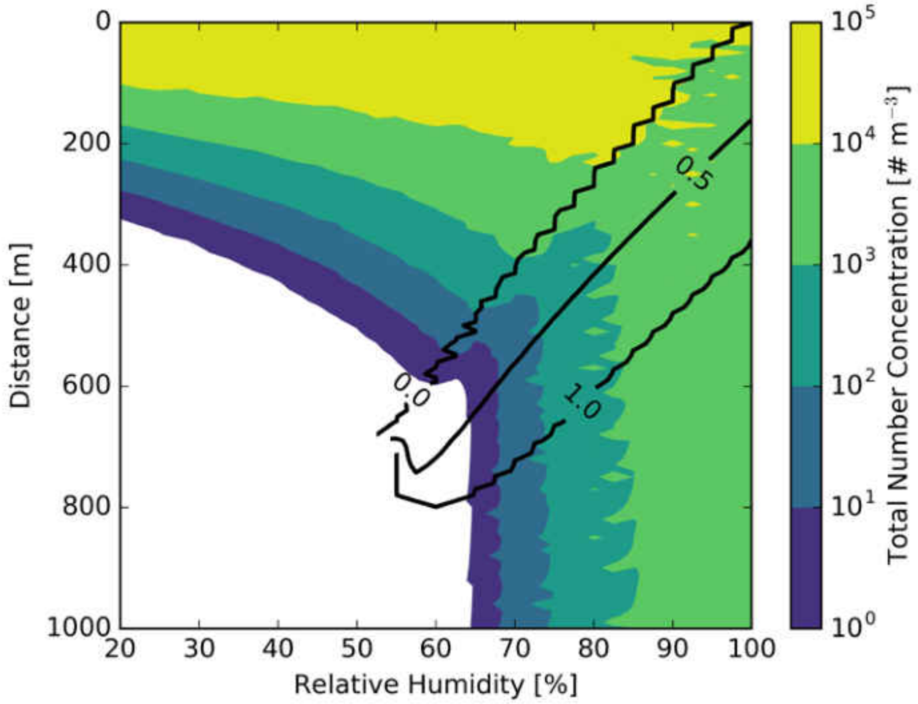

Figure 4-10: Total number concentration [# m^{-3}] as a function of relative humidity [%] and distance from the top of the melting layer [meters].

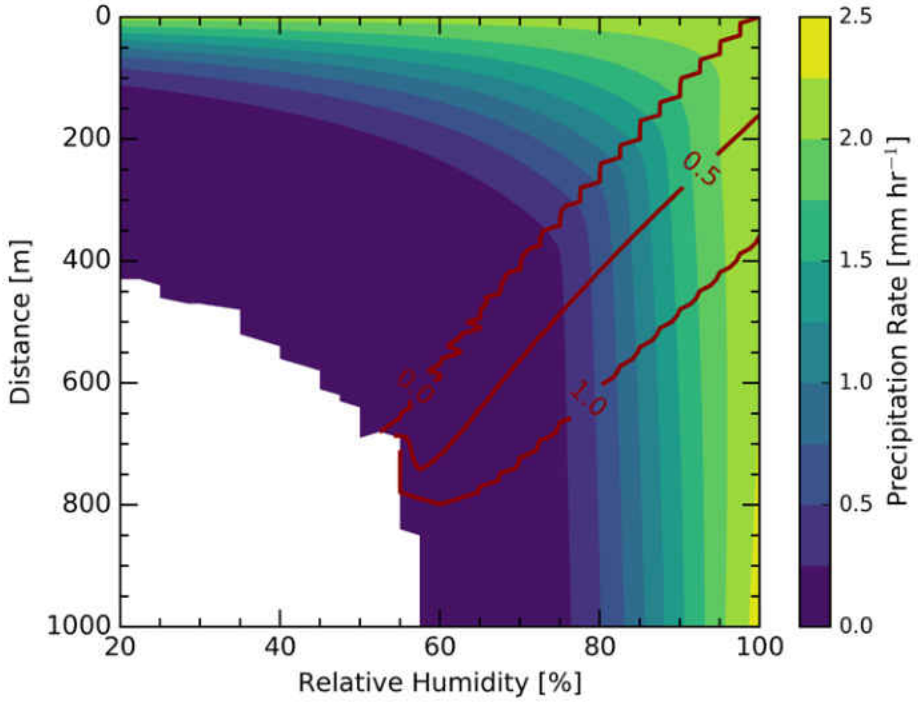

Figure 4-11: Precipitation rate in mm hr^{-1} (colors and gray contours) within the simulations as a function of relative humidity and distance from the top of the melting layer simulation.

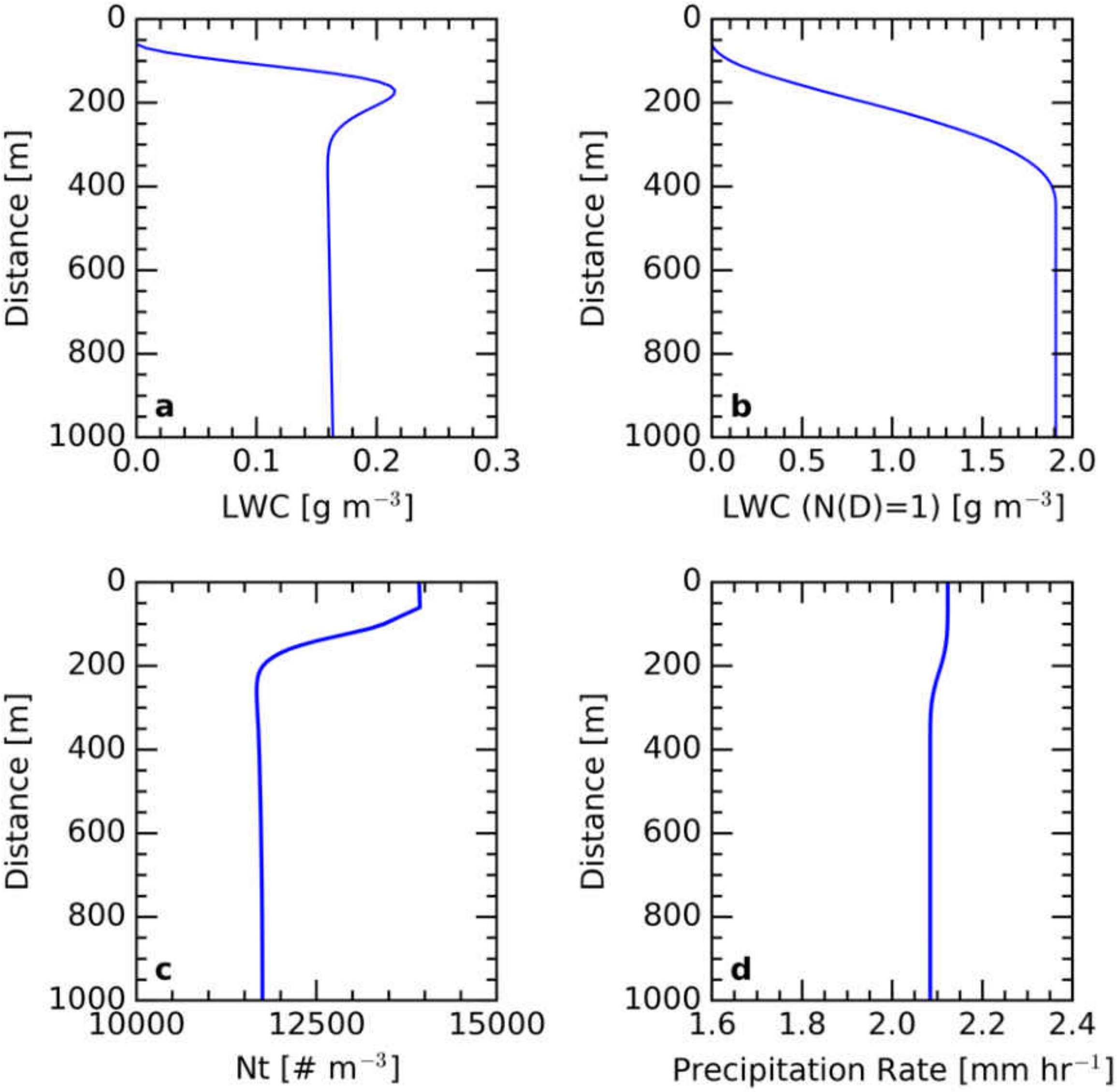

Figure 4-12: The a) liquid water content (LWC), b) liquid water content assuming the number concentration for each size bin equals 1.0 m^{-3}, c) total number concentration (N_t), and the precipitation rate for a simulation with a relative humidity of 95% and mass loss due to evaporation and sublimation turned off.

Conclusions

These results show that there is significant mass loss due to evaporation during melting within subsaturated environments. Short melting distances, accelerating particle fall speeds, and short melting times help constrain the amount of mass lost due to evaporation while melting is occurring, even in subsaturated profiles. Additional mass loss due to sublimation prior to melting can also be significant due to the delay in the onset of melting within the subsaturated profiles and the small terminal fall speeds and large sublimation rates found prior to the start of melting.

The trends shown on the particle scale also appear in the bulk distribution parameters such as rainfall rate and IWC. Sublimation removes a large amount of mass prior to melting, resulting in decreasing IWC, TWC, and rainfall rates with increasing distance into the melting layer within the subsaturated profiles. Condensational growth in the nearly water-saturated profiles (RH > 95%) results in an increase in LWC and rainfall rate with increasing distance into the melting layer.

From these results, it appears that the assumption of negligible mass loss due to evaporation while melting is occurring may not be valid. Studies such as Mitra et al. (1990) that use large, low-density snowflakes and high RH environments can safely use the assumption of negligible mass loss. Studies that use small ice particles or low RH environments (RH less than about 80%) cannot use the assumption of negligible mass loss due to evaporation.

CHAPTER V
MC3E PROFILE SIMULATIONS

Simulations that use observed atmospheric properties (e.g. air temperature) are conducted to learn how well the melting layer model can simulate real-world conditions. In turn, the model can help quantify variables that are difficult to measure directly from aircraft data (e.g. particle liquid water fraction).

Eleven melting layer simulations are conducted using air temperature, pressure, and relative humidity from in-situ aircraft data collected during the Midlatitude Continental Convective Clouds Experiment (MC3E). A brief description of this field campaign is given along with the methodology of how melting layer profiles are determined. As in Chapter 4, results of calculations within the model are saved every 12000 time steps (10 minutes of simulation time) and the results at 30 minutes of simulation time are presented here. Discussion includes details on whether ice and snow particles lose a significant amount of mass due to evaporation while melting, how well the simulations compare with the observations, and how the assumptions of particle shape, size, and density can affect the model results.

MC3E Field Campaign and Citation Instrumentation

MC3E was a field campaign conducted over north-central Oklahoma in spring of 2011 (Jensen et al. 2015). The campaign was jointly funded by the NASA Global Precipitation

Measurement Mission and the U. S. Department of Energy Atmospheric Radiation Measurement programs. One of the goals of MC3E was to "…advance understanding of different components of convective simulations and microphysical parameterizations" (Jensen et al. 2015). To reach this goal, a variety of mesoscale convective systems were observed using radiosondes, rain gauges, distrometers, a multitude of ground-based radars, airborne remote sensing, and airborne in-situ measurements. The airborne in-situ measurement platform was the UND Citation II research aircraft, henceforth referred to as the "Citation".

From the Citation dataset, ambient air temperature is derived from measurements made with the Rosemount Platinum Resistance total temperature sensor. Dew point temperature is measured by an EdgeTech Model 137 Vigilant aircraft hygrometer (henceforth known as the EdgeTech) and derived from tunable diode laser (TDL) hygrometer data (May 1998). In this study, dew point data from the TDL are used preferentially and the EdgeTech dew point data are used to fill in gaps in the TDL data. Aircraft position data, including altitude, are obtained with an Applanix Position and Orientation system. Total water content (TWC) and liquid water content (LWC) measurements are from the Sky Tech Research Nevzorov probe (Korolev et al. 1998). The temperature, humidity, position, TWC, and LWC data are processed using the Airborne Data Processing and Analysis package (ADPAA; Delene 2011) and also undergo manual quality assurance procedures.

The Particle Measuring Systems Inc. two-dimensional cloud (2DC) probe, the Droplet Measurement Technologies Inc. Cloud Imaging Probe (CIP), and the Stratton Park Engineering Company (SPEC) Inc. High-Volume Precipitation Spectrometer – Version 3 (HVPS-3) were used to record hydrometeor shadow images. 2DC, CIP, and HVPS-3 data are processed using the System for Optical Array Probe (OAP) Data Analysis (SODA; Bansemer 2016) software package to retrieve hydrometeor properties such as diameter and particle concentrations.

Melting Layer Determination

Air temperature data are analyzed to find the altitude of the 0 °C isotherm. Particle concentrations are examined for altitudes near the 0 °C isotherm to ensure there were hydrometeors present within and just above the melting layer. Particle imagery are used to determine the time at which particles were considered completely melted, as evidenced by round or nearly-round images. Particles must be nearly round in all of the OAP probe data available at that time (instrument performance issues prohibited data being available for all probes at all times).

In this study, valid melting layer profiles must have a discernable melting layer base in which all the particles within the OAP imagery are round or nearly so. Some melting layers in MC3E were not sampled through their full depth and are excluded from this analysis. The profiles through the melting layer must be continuous, and thus are limited to profiles that were sampled using ascending/descending ramp or ascending/descending spiral flight patterns. This restricts analysis over a small area and excludes the uncertainty associated with averaging across a large area that may contain vastly different populations of hydrometeors and varying thermodynamic profiles that have different melting layer depths. Finally, for simplicity the melting layer profiles sampled on 1 May 2011 are excluded due to the presence of two distinct melting layers separated by a very deep layer (over 1000 m) of below-freezing air.

The observed melting layer depth is defined as the distance between the 0 °C isotherm and the altitude at which all of the particles in the in-situ imagery are round. The definitions of the melting layer depths (model and observed) were chosen to be as consistent with one another as possible while allowing for uncertainties in measurements and the simplification of particle shape within the model. The OAP images cannot be used to determine which particles are just starting the melting process. (High-resolution Cloud Particle Imager data were not available for these melting layer profiles.) Thus, the 0 °C isotherm is used as a consistent level designating the top of the melting layer. Similarly, OAP data cannot be used to determine whether a round particle is completely comprised of liquid or if ice fragments are hidden inside a drop. This introduces some uncertainty into observed melting layer depths, but it is estimated that this uncertainty is no more than 50 meters and will tend to make the actual melting layer depth deeper than what is shown in Table 5-1.

Table 5-1: The time (in UTC) when the UND Citation crossed the 0 °C isotherm, the time at which the Citation was at the base of the melting layer (ML), and the observed depth of the melting layer.

Date	Profile Number	0 C time	Base Time	ML Depth [m]
04/27/11	1	10:03:42	10:08:30	429
04/27/11	2	10:38:34	10:37:24	363
05/10/11	1	23:00:33	23:03:22	662
05/10/11	2	23:22:42	23:25:17	516
05/10/11	3	23:28:59	23:30:25	200
05/10/11	4	23:37:02	23:38:02	162
05/20/11	1	13:32:26	13:31:00	579
05/20/11	2	15:17:48	15:19:04	471
05/20/11	3	15:51:58	15:49:00	593
05/20/11	4	16:31:26	16:33:24	490
06/01/11	1	21:24:37	21:28:52	684

MC3E Simulations Methodology

The Citation did not always sample a full km below the top of the melting layer in which the simulations cover. Thus, observed air temperature, pressure, and relative humidity data are augmented with ARM sounding data. The soundings were released every three hours during active weather periods from the ARM Southern Great Plains Central Facility site and can be found at http://www.arm.gov/instruments/sondeadjust/. The sounding data were quality controlled and corrected for temperature and relative humidity biases following Miloshevich et al. (2009).

Ice particle number concentration distributions in the melting layer model are initialized to represent the particular distribution being simulated. To estimate these distributions, merged OAP data (HVPS-3 data combined with CIP data or 2DC data when CIP data are not available) are averaged into 5 second intervals and a gamma distribution of the form

$$n(D) = N_0 D^{\mu} \exp(-\lambda D) \qquad \text{5-1}$$

is fit to them. The region just above each melting layer profile is analyzed to find the median values of N_0, μ, λ, and the maximum particle diameter present in the distribution (D_{max}). Results of the median distribution parameters for each observed profile are given in Table 5-2. The region just above the melting layer is generally where air temperatures range from -2 °C to 0 °C, but sometimes the region ends at the lowest temperature the Citation was at before entering a level flight pattern or descending into warmer air.

D_{max} is used to derive the model bin width (ΔD_e) through an iterative procedure. First, the equivalent liquid spherical diameter of a particle with equivalent mass to D_{max} (D_{emax}) is found by assuming the ice particle effective density can be represented by (2-19). Since (2-19) is in terms of D_e and not D, trial and error is used to determine D_{emax}. Second, the minimum model bin equivalent spherical diameter (equal to $2*10^{-5}$ m) is subtracted from D_{emax} to get the range of D_e in the model. Finally, the range of D_e is divided by the number of model bins (300) to obtain ΔD_e.

For each simulation, values of N_0, μ, λ, ΔD_e, and the input T_∞, P, and RH are changed to match the respective MC3E profile being simulated. All model levels are initialized with the same particle number distribution, but then are allowed to change as a result of aggregation, evaporation, etc. As in Chapter 3, vertical air motion is assumed to be negligible. However, the aggregation, accretion, and collision and coalescence processes are turned on because previous research suggests that these processes were probably occurring within some of the melting layer profiles considered here (Neumann et al. 2014).

Table 5-2: Median values of the gamma distribution intercept (N_0), breadth (μ), and slope (λ) parameters as well as the mean values of maximum diameter (D_{max}) in the observed 5-second averaged particle size distributions in the given timeframe for the particular melting layer profile on the given date.

Date	Profile #	-2 C time	0 C time	N_0 [cm$^{-(3+\mu)}$ μm^{-1}]	μ	λ [cm^{-1}]	D_{max} [mm]	ΔD_e [μm]
04/27	1	35985	36222	$9.3880*10^{-8}$	-0.9497	2.9852	13.3	7.94
04/27	2	38500	38314	$1.0596*10^{-6}$	-0.6491	7.9164	8.7	9.00
05/10	1	82700	82833	$1.1207*10^{-7}$	-1.0377	2.7840	13.2	7.90
05/10	2	84317	84390	$1.7167*10^{-10}$	-2.2849	0.2402	6.6	5.00
05/10	3	84400	84539	$7.1410*10^{-9}$	-1.6015	7.6048	3.4	3.30
05/10	4	84900	85022	$1.6886*10^{-8}$	-1.5821	8.3769	5.0	4.20
05/20	1	48746	48900	$4.6331*10^{-8}$	-1.2753	2.4764	15.0	8.60
05/20	2	54900	55069	$1.0876*10^{-6}$	-0.6452	6.1035	11.0	7.00
05/20	3	57118	57250	$1.1355*10^{-7}$	-0.9341	4.6510	8.7	6.00
05/20	4	59300	59486	$4.0650*10^{-9}$	-1.7085	1.8827	8.7	6.00
06/01	1	76900	77077	$7.5815*10^{-9}$	-1.2588	2.9815	9.4	6.30

Results and Discussion

Description of MC3E Melting Layer and Properties

Eleven melting layer profiles sampled during MC3E fit all of the above criteria; the dates, times, and melting layer depths are provided in Table 5-1. Most profiles exhibit steep temperature lapse rates over parts, if not through the entire, melting layer (Figure 5-1a). This is not that surprising given the convective environments in which the profiles were collected. The second profile on 27 April (4/27_P2) and the second profile on 10 May (5/10_P2) had 120 m deep layers in which the temperature is approximately isothermal at 0.0 °C and 1.0 °C, respectively. Other than these two, there is little evidence of isothermal layers present with the melting layer like that which was presented in Willis and Heymsfield (1989). Two of the profiles (the first profile on 27 April and the second profile on 20 May) had two regions of above 0 °C temperatures separated by a shallow (100-200 m) layer of sub-0 °C temperatures.

Most of the eleven melting layer profiles were sampled between 2.7 and 4.3 km above mean sea level. The pressure for these melting layers varied between 610 and 740 hPa Figure 5-1b). The atmospheric air column was cooler on 27 April than on the rest of the days with valid melting layers (not shown). This led to the melting layers on 27 April to being located at lower altitudes and have correspondingly higher pressures than the rest of the melting layer profiles used in this study (Figure 5-1b).

Although the total number of observed melting layer profiles is small, a wide variety of humidity profiles were sampled with respect to liquid water (Figure 5-2). Based on RH, the melting layers can be roughly grouped into four types of profiles: supersaturated, near-saturated, subsaturated, and very subsaturated. The supersaturated profile is defined as having RH at or above water saturation for the majority of the depth in which particles melt. The 4/27_P2 is the only melting layer profile that fits into the supersaturated category. This profile is supersaturated in the top 200 meters of the melting layer and the RH slowly decreases with increasing distance through the profile.

Near-saturated profiles are profiles generally have RH above 90% at the top of the melting layer and have peak RH between 95 and 100%. There are four profiles from the MC3E data in which fit this category: first profile from 27 April (4/27_P1), 5/10_P2, first profile from 20 May (5/20_P1), and second profile from 20 May (5/20_P2). These profiles generally have peak RH values between 95 and 100% in the 150-400 meters below the 0 °C isotherm, and below 400 meters have RH slowly decreasing with increasing distance into the melting layer.

Profiles with RH generally between 60 and 90% are considered subsaturated profiles. Four of the profiles in this study fall into this category: the first, third, and fourth profiles from 10 May (5/10_P1, 5/10_P3, and 5/10_P4, respectively) and the fourth profile from 20 May (5/20_P4). These profiles generally have the largest RH in the top 200 m of the profiles and the RH decreases with increasing distance below the peak RH for a few hundred meters (Figure 5-2).

The third profile on 20 May (5/20_P3) and the melting layer profile from 1 June (6/01_P1) fall into the very subsaturated category. The 5/10_P3 has an RH of 60% at the top of the melting layer, maximum RH of 65% about 300 m below the 0 °C isotherm, and has a bottom RH near 50%. The 6/01_P1 is near saturated at the 0 °C isotherm, the RH decreases to about 60% near 300 m into the melting layer, increases to 78%, then decreases to 30% at 1 km below the top of the melting layer.

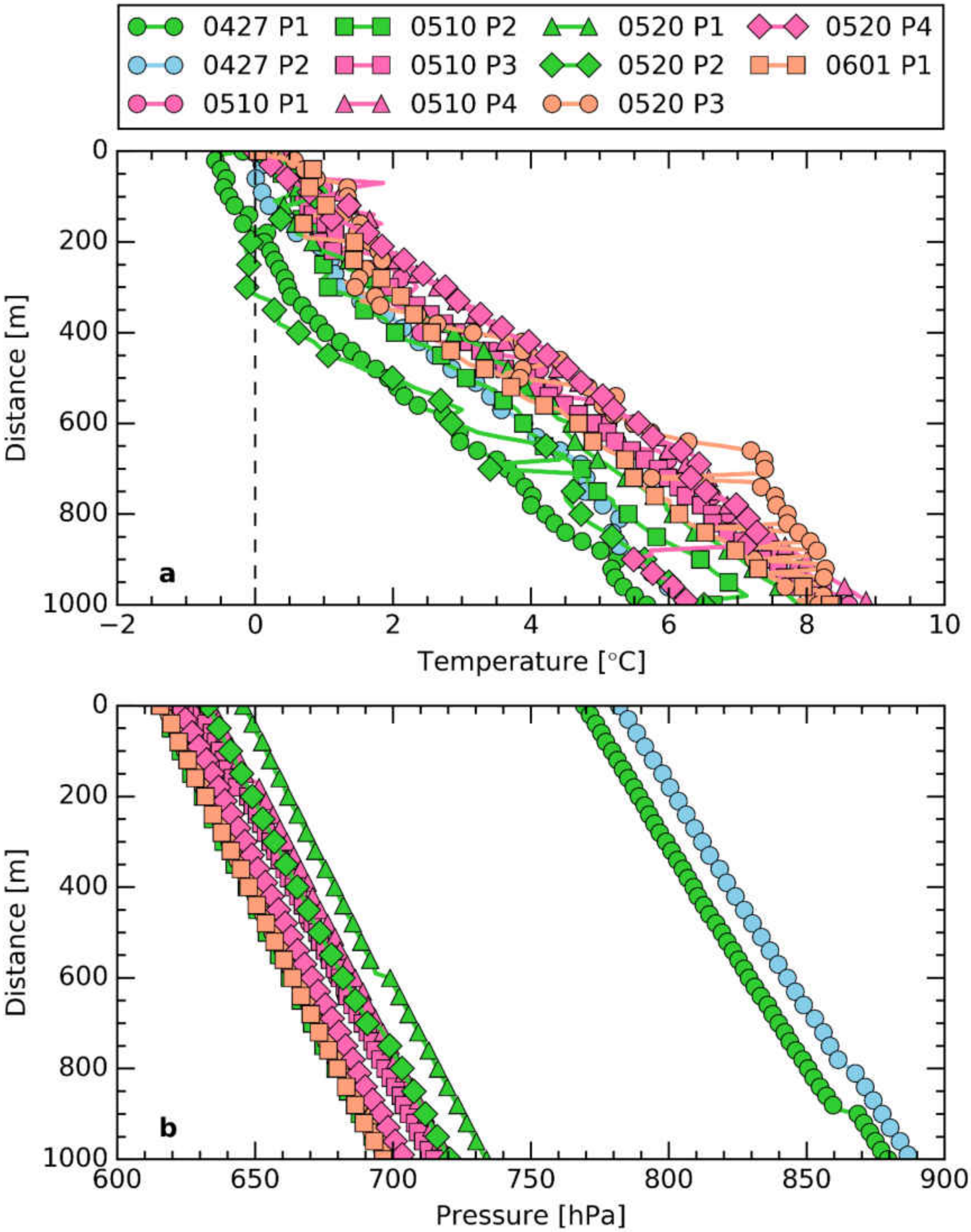

Figure 5-1: Observed a) air temperature and b) pressure profiles of melting layers from the MC3E field campaign as a function of distance from the highest observed 0 °C isotherm. Dashed line in a) denotes 0 °C isotherm. The blue, green, pink, and orange lines denotes the supersaturated, near-saturated, subsaturated, and very subsaturated profiles, respectively.

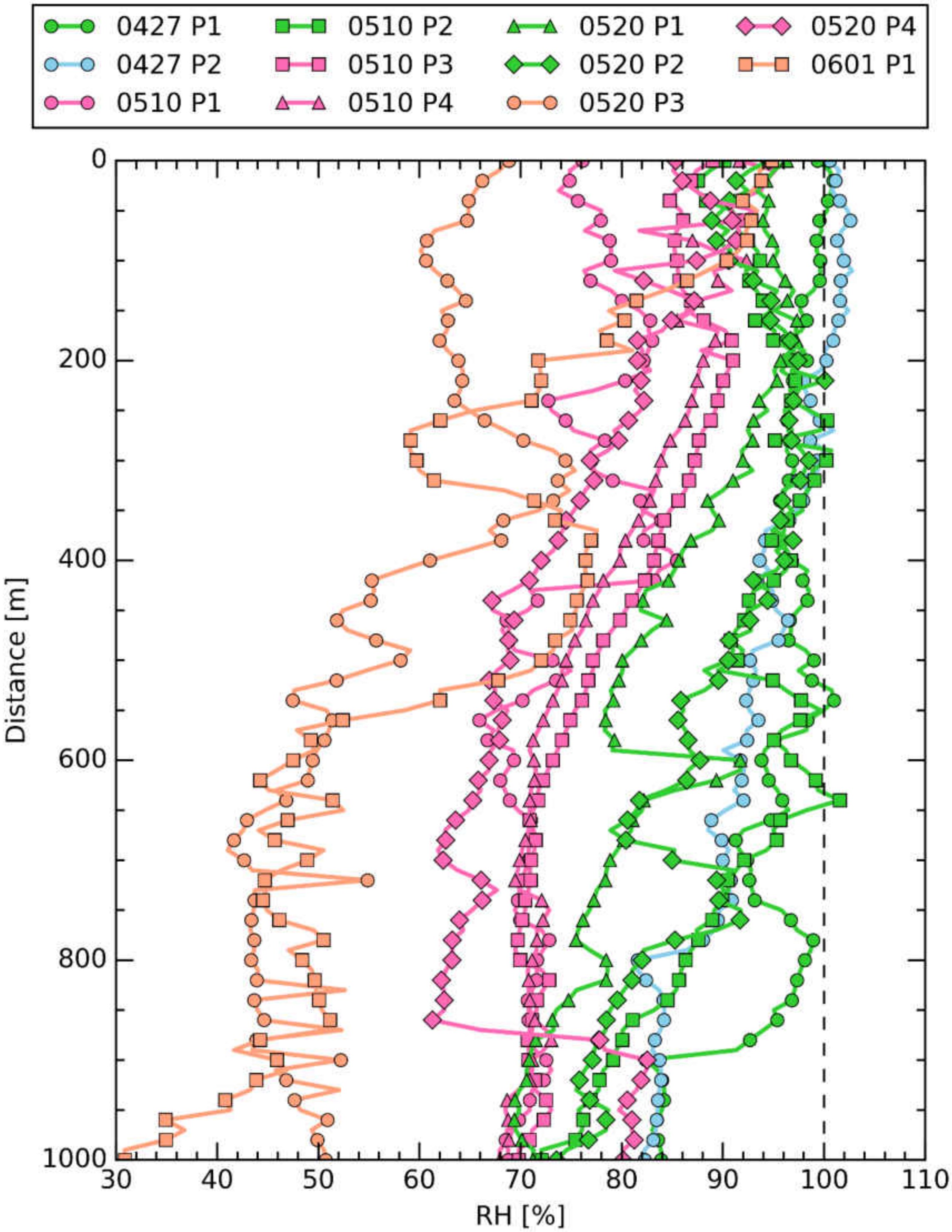

Figure 5-2: Observed relative humidity profiles of melting layers from the MC3E field campaign as a function of distance from the highest observed 0 °C isotherm. Dashed line denotes 100% relative humidity. The blue, green, pink, and orange lines denotes the supersaturated, near-saturated, subsaturated, and very subsaturated profiles, respectively.

Evaporative mass loss during melting

Figure 5-3 shows that nine of the eleven MC3E profiles show significant mass loss (again defined as more than 10% relative mass loss) in at least three size bins while melting. The 4/27_P2 represents a supersaturated environment where particles undergo significant particle growth via condensation. All of the particles in the remaining profile (5/20_P3) sublimate away before melting can begin. The aggregation/accretion/collision and coalescence (A/A/CC) processes act to increase the particle size and these processes are more effective for the large particle sizes, which is why there is a trend towards less particle mass loss/greater mass gain with increasing particle size in most profiles.

The 5/10_P1 simulation is notable because all particle size bins have over 5% of mass loss due to evaporation while melting and two-thirds of the size bins have over 10% mass loss (Figure 5-3). This profile appears to hit the "sweet spot" where the profile is subsaturated enough to have both significant amounts of melting and sublimational mass loss (Figure 5-4), but not too subsaturated so that all the particle sizes sublimate or evaporate completely. The time the particles spend sublimating within this profile is larger than most of the other profiles (Figure 5-5a) due to the long distance the particles must fall before melting can begin (Figure 5-2). The time the particles spend melting in the 5/10_P1 simulation is near average compared to all of the profiles that have melting particles. However, the profile has the largest sublimation rate in the top 270 m of the profile of all the simulations before melting starts and generally has the largest evaporation rate of all the profiles as well. In this case, the particles undergo large evaporation and sublimation rates, which causes the particles to have significant mass loss both in the sublimation and melting regions of the simulation.

The 5/10_P3 profile is generally a little more saturated on average than the 5/10_P1 profile (Figure 5-2), but only the smallest 12 size bins that encounter melting show significant mass loss while melting (Figure 5-3). Excluding the particles that sublimate completely, the particles in the 5/10_P3 profile spend about average amounts of time sublimating (Figure 5-5a), but the sublimation rate is about an order of magnitude smaller than the 5/10_P1 profile (Figure 5-6). The sublimation rate is still large enough for all of the particles to experience a significant amount of mass loss due to sublimation (Figure 5-4). The short melting times for the sub-millimeter particles (Figure 5-5b) and the small evaporation rates for the 5/10_P3 profile (Figure 5-7) lead to only the very smallest particles experiencing significant mass loss.

The 4/27_P1 profile also exhibits mostly insignificant mass change (again except for the very smallest of size bins; Figure 5-3), but this is from deposition and condensation compensating for evaporational and sublimational mass loss. Figure 5-6 shows the particles in the 4/27_P1 profile undergo deposition in the top 50 m of the simulation, then sublimation removes mass for the next 200 m. Once melting begins, particles lose mass due to evaporation as they fall through the 250-350 m layer, then undergo condensational growth while falling through the subsequent 300 m layer. The 5/10_P4 profile is the only other profile to exhibit depositional growth, but six out of the eleven MC3E profiles have compensating condensational mass gain/evaporation mass loss occurring.

The profiles with the most depositional/condensational growth are the 4/27_P2 and 5/10_P4 profiles. In the 4/27_P2 profile, only a handful of particles sizes have less than a 10% mass gain (Figure 5-3). The most significant mass gains are at the smallest of sizes due to the long time spent in the layer in which they melt (Figure 5-5b) and the largest particles sizes where condensational growth is aided by A/A/CC (largest particles gain the most mass from A/A/CC). The particles with initial sizes of 20 to 100 µm in the 5/10_P4 profile have the largest relative mass gain due to condensation of all of the MC3E simulations (Figure 5-3) due to the highly supersaturated environment (Figure 5-2). Once particles fall out of the supersaturated top 175 m of the 5/10_P4 profile, they undergo slight evaporational mass loss which offsets the mass gain via condensation somewhat (Figure 5-7).

On the opposite end of the spectrum, the particles within the 5/20_P3 profile experience only sublimation. Figure 5-8 shows that the melting rate for the particles is always less than zero, which means that the temperature difference between the air and the particles is never large enough to overcome the sublimational cooling occurring and thus the particles never melt. Although the sublimation rate is not the largest of the MC3E profiles (Figure 5-6), because the particles never encounter conditions conducive to melting in the simulation, the particles sublimate completely.

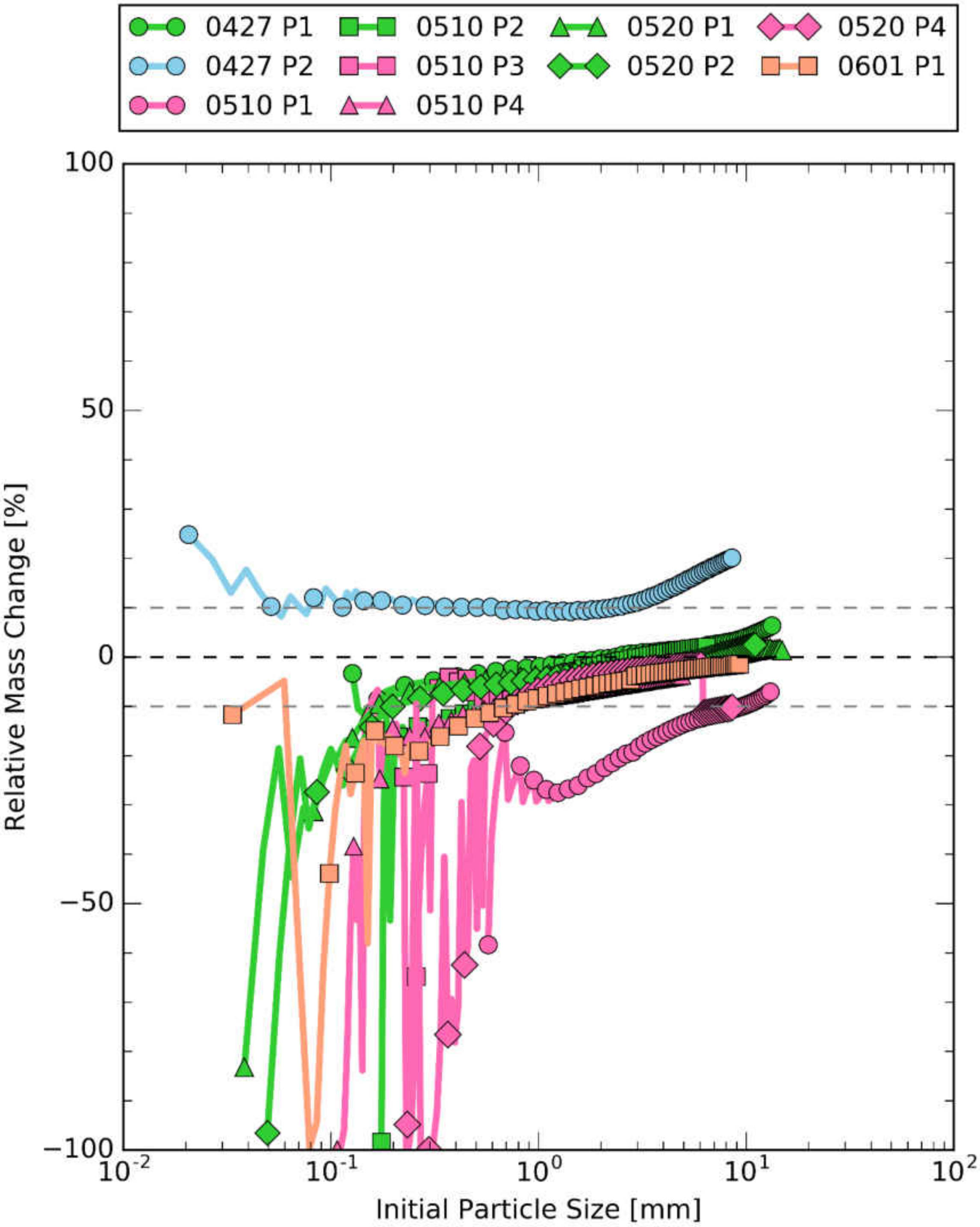

Figure 5-3: Relative mass change during melting as a function of initial particle diameter in millimeters for each simulated MC3E profile. Dashed black line denotes zero relative mass change and dashed gray lines denote 10% relative mass change. The blue, green, pink, and orange lines denotes the supersaturated, near-saturated, subsaturated, and very subsaturated profiles, respectively.

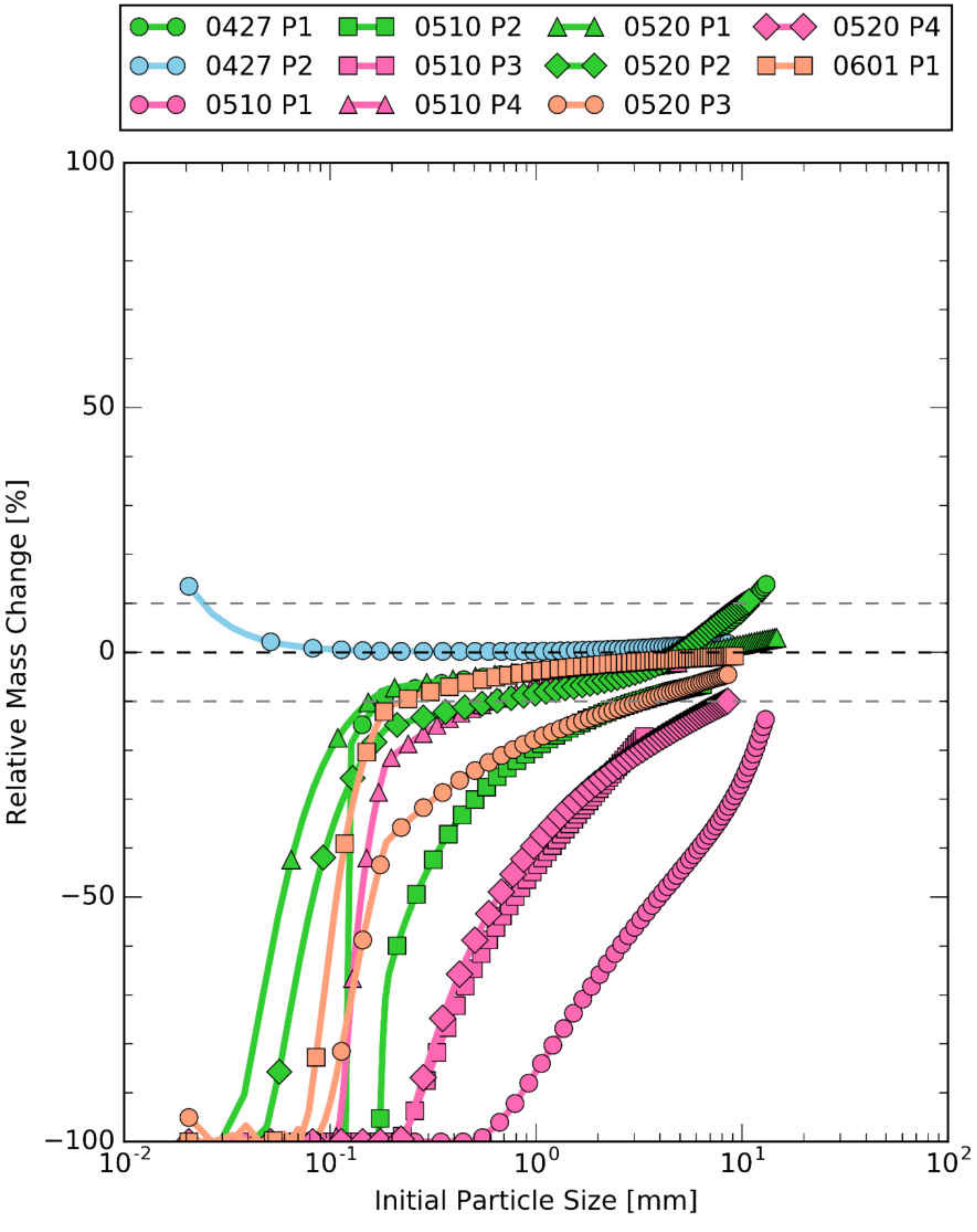

Figure 5-4: Relative mass change before melting begins as a function of initial particle diameter in millimeters for each simulated MC3E profile. The blue, green, pink, and orange lines denotes the supersaturated, near-saturated, subsaturated, and very subsaturated profiles, respectively.

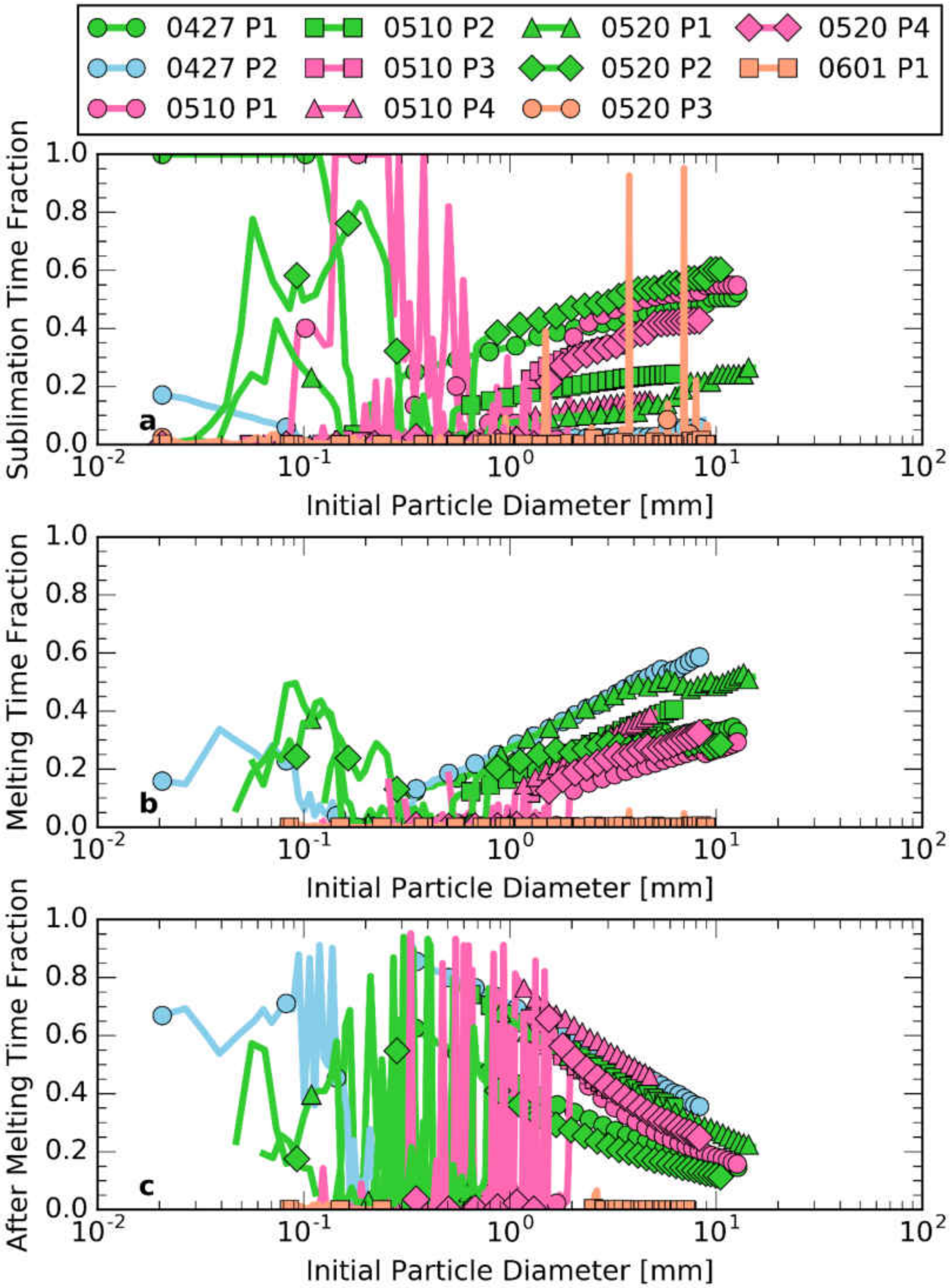

Figure 5-5: Fraction of total simulation time ice particles spend undergoing a) sublimation, b) melting, and c) evaporating after melting completes and before falling out the bottom of the simulation as a function of the initial particle diameter for MC3E melting layer profile simulations. The blue, green, pink, and orange lines denotes the supersaturated, near-saturated, subsaturated, and very subsaturated profiles, respectively.

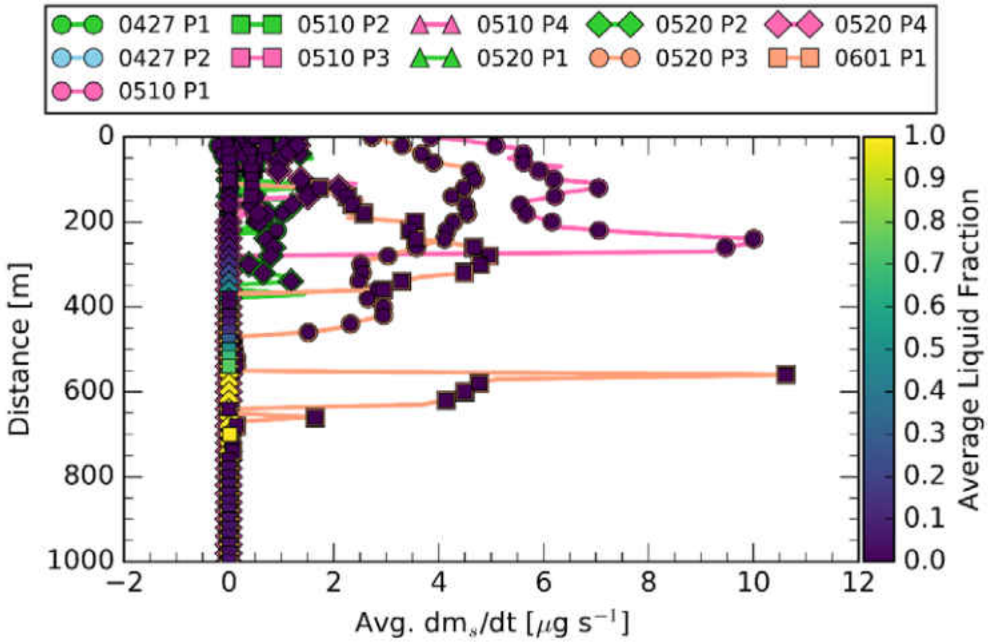

Figure 5-6: Average mass-weighted sublimation rate as a function of distance from the top of the melting layer model for each simulated profile. Average mass-weighted liquid volume fraction (F_{liq}) is given by the colored markers. The blue, green, pink, and orange lines denotes the supersaturated, near-saturated, subsaturated, and very subsaturated profiles, respectively.

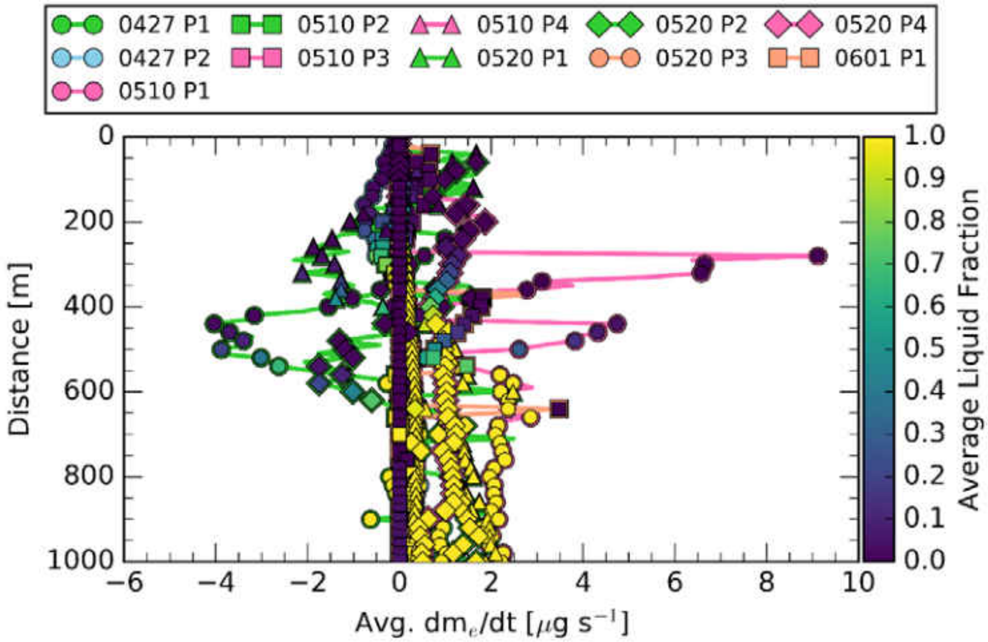

Figure 5-7: Average mass-weighted evaporation rate as a function of distance from the top of the melting layer model for each simulated profile. Average mass-weighted liquid volume fraction (F_{liq}) is given by the colored markers. The blue, green, pink, and orange lines denotes the supersaturated, near-saturated, subsaturated, and very subsaturated profiles, respectively.

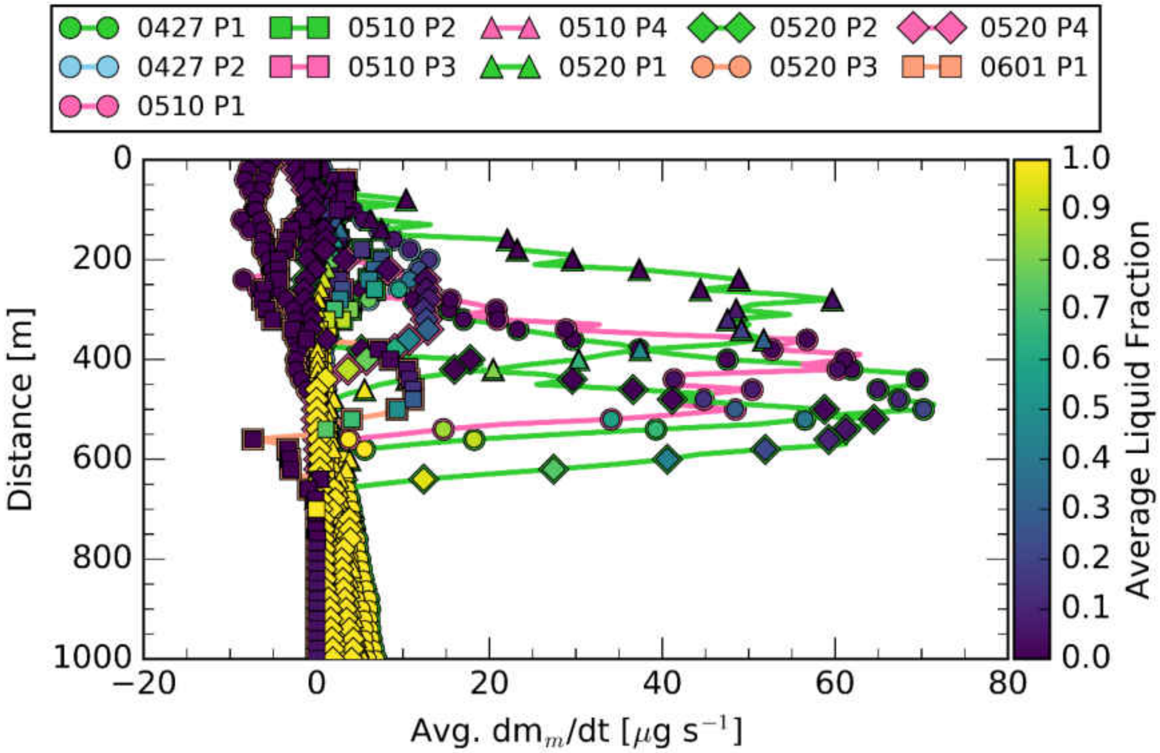

Figure 5-8: The mass-weighted average melting rate as a function of distance from the top of the melting layer model for the second profile on 20 May 2011 (0520 P2), the third profile on 20 May 2011 (0520 P3) and the first profile on 1 June 2011 (0601 P1). Average mass-weighted liquid volume fraction (F_{liq}) is given by the colored markers. The blue, green, pink, and orange lines denotes the supersaturated, near-saturated, subsaturated, and very subsaturated profiles, respectively.

Comparisons Between Observed and Simulated Profiles

The LWC and TWC measurements from the Nevzorov probe are used to compare the observed melting layers with their corresponding simulations. The Nevzorov probe has a known low bias in areas that have maximum particle diameters greater than 4 mm. Accuracy in both LWC and TWC measurements are estimated to be within 10% of the given value.

The profile with the best agreement between the observations and the simulation is the 0427_P2 profile which has really good agreement between total and liquid water content (Figure 5-9) and melting layer depth (Table 5-3). The simulated TWC at 0 °C is 0.30 g m^{-3} greater than the observations, but observations and simulation agree quite well from 60 m on downward. The observed LWC profile has a local maximum at 120 m below the 0 °C isotherm. It is possible the model has reproduced this feature since the simulated LWC profile also has a local maximum, located 60 m below the local maximum in the observed LWC profile. The 0510_P3 profile is also simulated quite well; although the simulated TWC is on the low side compared to the observations, the observed and simulated LWC and the melting layer depths are in fairly good agreement.

The melting layer model appears to simulate the processes occurring within the 0427_P2 profile very well, but does not do as well for other profiles. The 0520_P1, 0520_P2, and 0601_P1 profiles also have really good agreement between the observed and simulated TWC and LWC (not shown), but not for the melting layer depths (Table 5-3). The model underestimates the melting layer depth in the 0520_P1 profile and overestimates it in the 0520_P2 profile. The melting layer model evaporates the particles completely before melting can finish which is in disagreement with the observations (Table 5-3).

The 0427_P1 simulation TWC has good agreement with observations throughout the observed melting layer, but there is a large amount of LWC present in the top 300 m of the melting layer profile that is not accounted for by the model (Figure 5-11). The LWC at the top of the melting layer is likely from liquid cloud droplets. These cloud droplets would be accreted by precipitating ice particles and through latent heat release aid in the melting process. This may be why the melting layer model predicted a deeper melting layer depth than what was observed.

Two profiles appear to have a poor comparison between the observations and simulations. The 0510_P2 profile simulated and observed TWC and LWC are similar in the top 100 m of the melting layer (not shown); however, below 100 m, both the observed TWC and LWC increase significantly by as much as a factor of 10. The flight profile for 0510_P2 was an ascending ramp, so the particles observed in the 0 to -2 °C layer were tens of kilometers away from the particles observed in the middle and bottom of the melting layer and the stratiform precipitation region being sampled appears to be not very homogeneous.

The 0520_P3 profile was at the rear edge of a stratiform precipitation region where conditions were not homogeneous. Figure 5-12 shows that the simulated TWC at the 0 °C isotherm is much larger than the observed values. The observed LWC is likely biased 0.01 g m^{-3} low due to a poor Nevzorov baseline, but Figure 5-12 shows that there is possibly some LWC present in the melting layer. The simulation has all the particles sublimate completely before they even start melting. However, Figure 5-13a shows there are some millimeter-sized ice particles present in the 2DC imagery collected high in the melting layer and some round liquid droplets in the 2DC imagery from a lower altitude less than a minute earlier (flight pattern was an ascending spiral; Figure 5-12b). From the simulation results, either the parent ice particles for the liquid drops were very large or very dense, or the environmental profile was more saturated than what was depicted in the simulation.

Table 5-3: Observed melting layer (ML) depth, simulated melting layer depth, and the difference between the observed and simulated melting layer depths for each melting layer profile. Negative differences in melting layer depths indicate where the model underestimated melting layer depth compared to the observations. *SA means that all particles sublimated/evaporated away before they could melt or finish melting.

Date	Profile #	Obs. ML Depth [m]	Sim. ML Depth [m]	Difference [m]
04/27	1	429	580	151
04/27	2	363	370	7
05/10	1	662	550	-112
05/10	2	516	350	-166
05/10	3	200	170	-30
05/10	4	162	90	-72
05/20	1	579	470	-109
05/20	2	471	650	179
05/20	3	593	SA*	--
05/20	4	490	450	-40
06/01	1	684	SA*	--

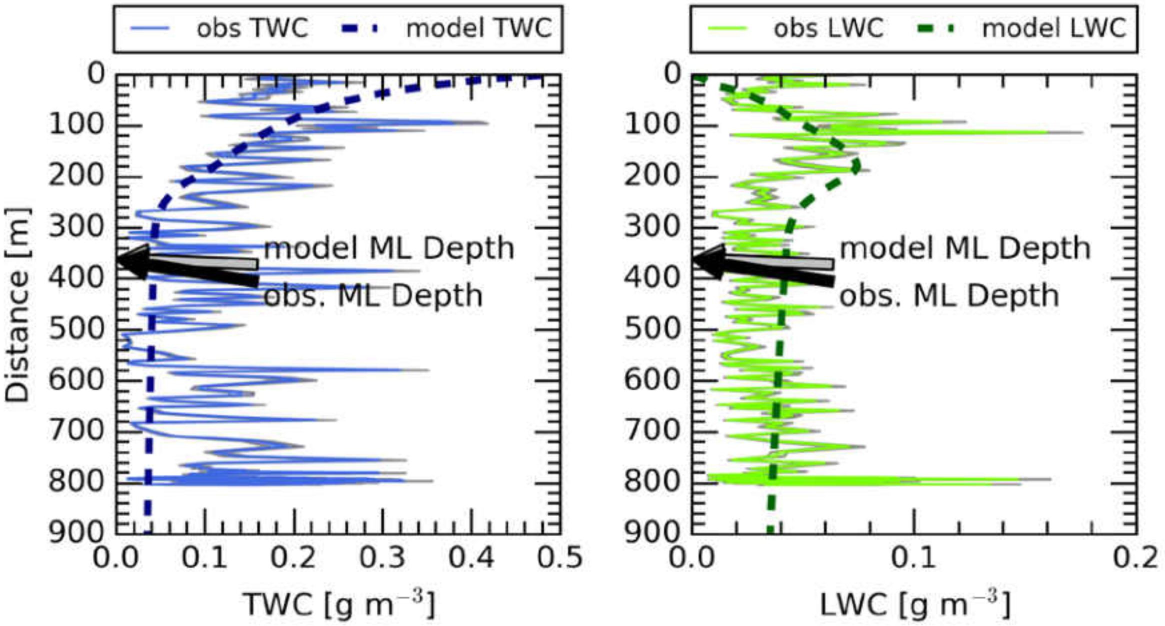

Figure 5-9: Total water content (left) and liquid water content (right) observed on the second melting layer profile on 27 April 2011 (solid line) and simulated with a melting layer model (dashed line). Observation uncertainty is shown in the shaded regions bracketing the observations. Depth of the melting layer from observations (obs. ML Depth) and from the simulation (model ML Depth) are depicted with black and gray arrows, respectively.

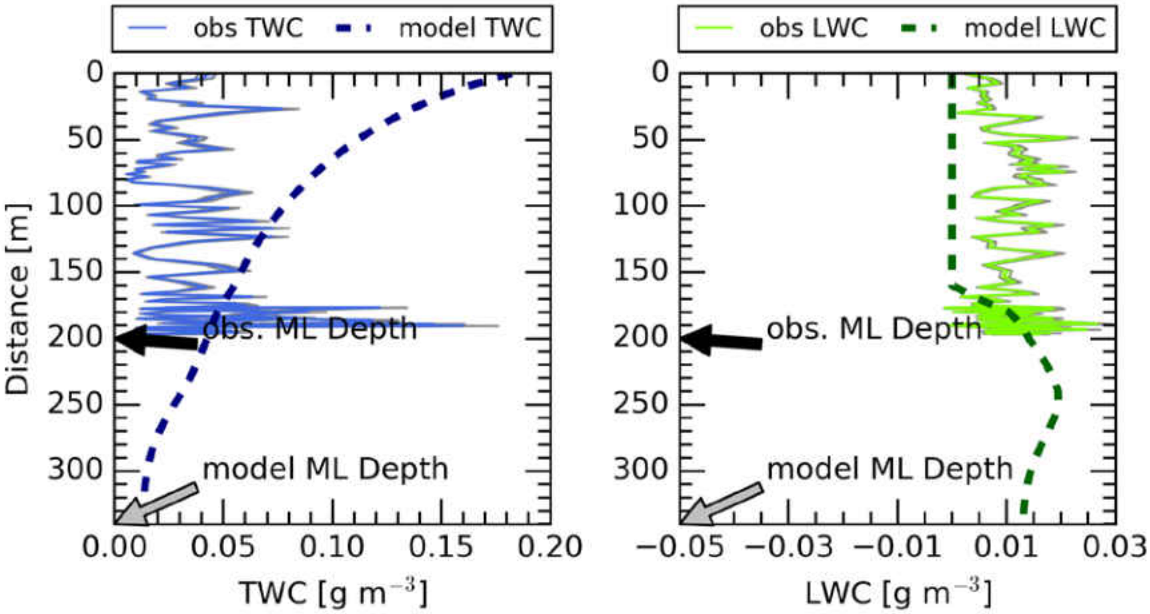

Figure 5-10: Total water content (left) and liquid water content (right) observed on the third melting layer profile on 10 May 2011 (solid line) and simulated with a melting layer model (dashed line). Observation uncertainty is shown in the shaded regions bracketing the observations. Depth of the melting layer from observations (obs. ML Depth) and from the simulation (model ML Depth) are depicted with black and gray arrows, respectively.

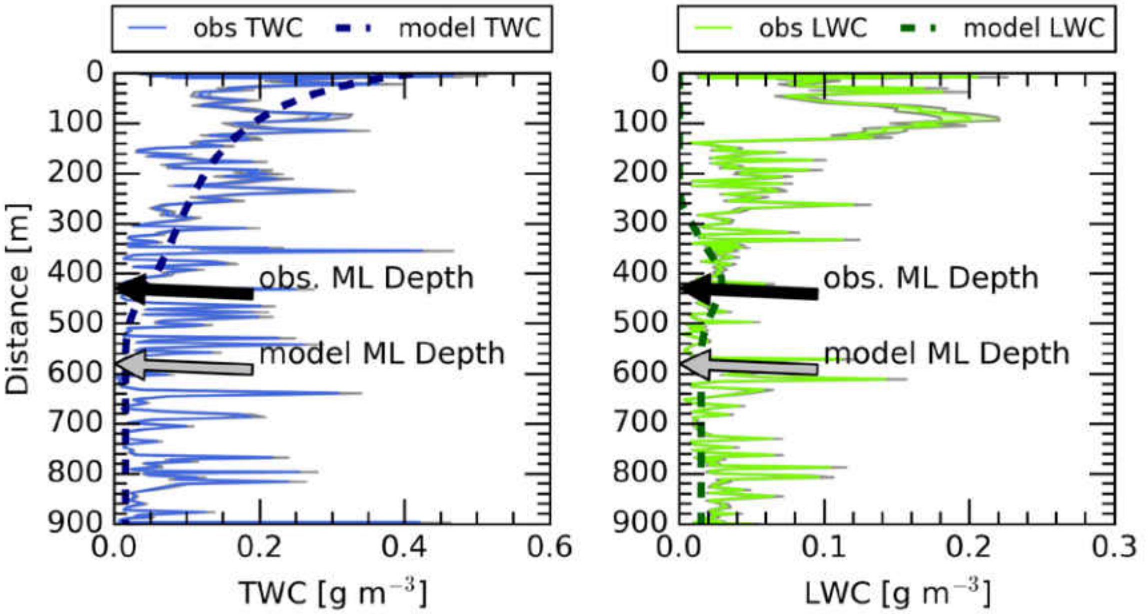

Figure 5-11: Total water content (left) and liquid water content (right) observed on the first melting layer profile on 27 April 2011 (solid line) and simulated with a melting layer model (dashed line). Observation uncertainty is shown in the shaded regions bracketing the observations. Depth of the melting layer from observations (obs. ML Depth) and from the simulation (model ML Depth) are depicted with black and gray arrows, respectively.

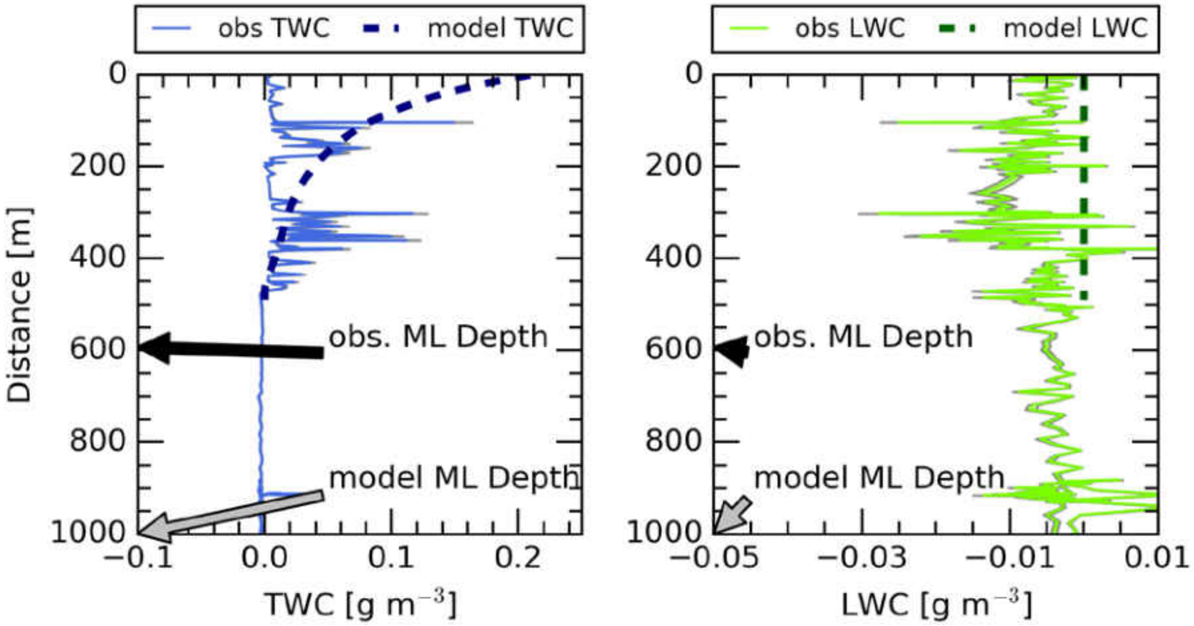

Figure 5-12: Total water content (left) and liquid water content (right) observed on the third melting layer profile on 20 May 2011 (solid line) and simulated with a melting layer model (dashed line). Observation uncertainty shown in the shaded regions bracketing the observations. Depth of the melting layer from observations (obs. ML Depth) and from the simulation (model ML Depth) are depicted with black and gray arrows, respectively.

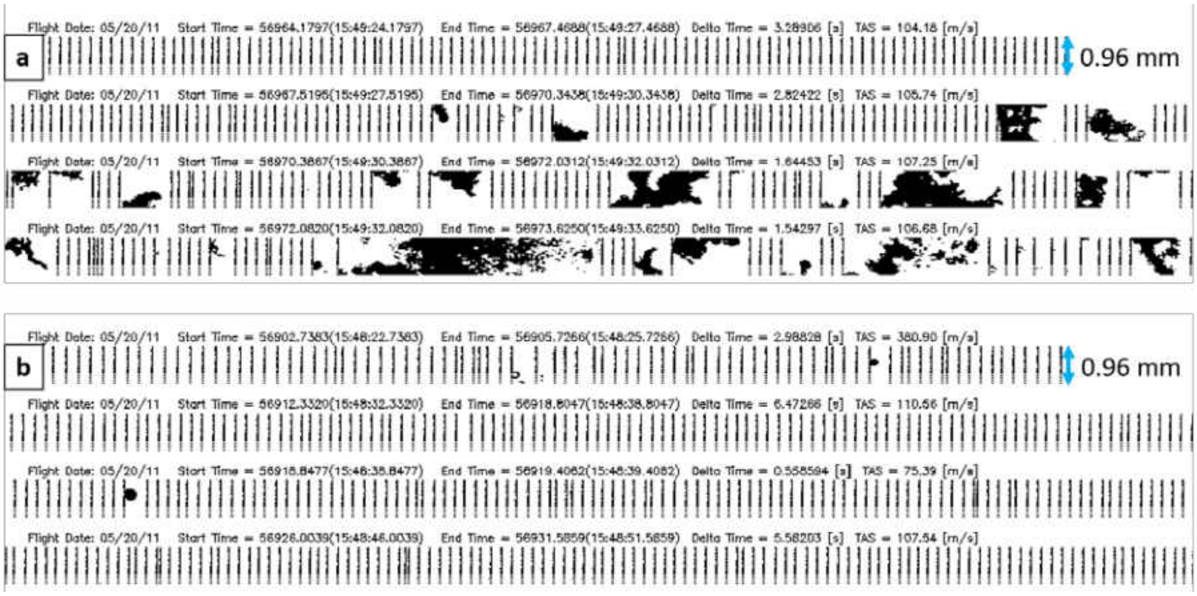

Figure 5-13: Particle images from the 2DC from the 20 May 2011 flight between a) 15:49:24.2 and 15:49:33.6, b) 15:48:22.7 and 15:48:51.6 UTC. Horizontal lines denote the start/end point of images. Image array width (blue arrow) is 0.96 mm.

Particle Shape, Size, and Density

Ice particle shape also affects the melting rate. Studies such as Oraltay and Hallett (2005) have shown that melting ice particles reach a critical point within the melting process and then particles' ice skeletons collapse, resulting in smaller particle diameters. A particle will have a smaller melting rate after the ice skeleton collapses because of its smaller diameter.

However, particle shape is not well resolved within these simulations, which applies a spherical particle approximation and no attempt is made to represent the collapsing of the particle ice structure. The diameter of the particles decrease though evaporation and sublimation, which removes mass, and melting which converts ice mass to water. Water has a higher density than ice and thus takes up less space than an equivalent amount of ice mass. Although the particle size decreases fairly rapidly at the end of the melting process during the simulations, it is likely the change in diameter is actually more dramatic, which would likely reduce the maximum instantaneous melting rates.

Particle size has a large influence on the melting layer model simulations. The ventilation coefficient is dependent on D, the melting rate depends on both f_v and D, and F_{liq} has a minor dependence on D. The cloud-size particles sublimate away before melting in low-RH environments while the large, precipitation-size particles fall quickly through the entire model depth. The cut-off RH value between where particles can begin to melt and where they cannot before sublimating away will vary with respect to the maximum size of the particle distribution and the mass of the ice particles. For example, increasing the maximum particle size or increasing the particle mass compared to the input distributions used here will result in decreasing the cut-off RH value.

Obviously, particle effective density also has large influence upon the melting layer, as shown in Chapter 2. The simulations within Chapters 3 and 4 both use a single effective-density relation that is dependent on D_e. Some of the variability and disagreement between the observations and simulations of the MC3E profiles probably comes from the use of a single effective density relation. To improve upon the results shown here, a better attempt at customizing the particle mass/density to the individual profiles should be considered.

Conclusions

As in Chapter 4, the results presented here in Chapter 5 show that significant mass loss due to evaporation during the melting process is possible given the right environmental conditions. A profile such as 0510_P1 represents relative humidity conditions that result in considerable mass loss for all particle sizes. Most melting layer profiles sampled during MC3E were too humid for more than a dozen or two of the smallest particle sizes to experience significant mass loss. The aggregation, accretion, and collision and coalescence processes also offset significant mass loss at the largest particles sizes because these particles are the most efficient at collecting smaller particles due to their relative large sweep-out area.

These results also show that the melting layer model can be used to successfully simulate processes that occur in actual melting layers. Two of the simulated melting layer profiles (0427_P2 and 0510_P3) have TWC, LWC, and melting layer depths that are similar to observations. Other profiles have less favorable results due to the presence of cloud liquid water that is unaccounted for in the model or model input. Additionally, some of the simulated melting layer profiles may have environments and/or initial particle properties that are non-representative of the melting layers that are being studied.

CHAPTER VI
SUMMARY AND DISCUSSION

Melting layers are present wherever ice particles fall into above freezing air and begin to melt. In warm environments most ice particles melt completely and fall to the ground as rain, although sufficiently dense particles do not fully melt and thus reach the surface as graupel and hail. Some previous melting layer studies assume that melting occurs at or near saturation and thus melting particles would not lose a significant amount of mass due to evaporation. However, there are places such as below MCS anvils, below MCS cloud bases, elevated precipitation regions, and downstream of orographic wave clouds where melting can occur in subsaturated environments.

This study uses the melting layer model described by Olson et al. (2001) to determine whether a melting ice particle loses a significant fraction of its mass due to evaporation in subsaturated environments. The melting layer model has been modified several ways:

- evaporation and sublimation are incorporated,
- the order in which the model loops over particle size and model layers is reversed,
- a particle sedimentation scheme is included,
- aggregation, accretion, and collision and coalescence processes are included,

- water vapor diffusivity (ψ) and the Schmidt number (Sc) are changed from constants to variables that follow simulated environmental conditions,
- particle temperature is changed from a fixed 0.01 °C to a variable dependent on the ambient temperature and relative humidity,
- the terminal velocity (v_t) of liquid drops is changed to follow the Beard (1976) parameterization to more accurately represent the actual v_t of drizzle-sized drops, and
- a new ice particle effective density-dimensional relationship is used to compute particle mass instead of fixed particle density which overestimates the mass of large particles.

The results of simulations of both idealized melting layer environments and observed melting layer profiles show that there is significant mass loss due to evaporation during melting within subsaturated environments. In the idealized melting layer simulations, short melting distances, accelerating particle fall speeds, and short melting times help constrain the amount of mass lost due to evaporation while melting is occurring, even in subsaturated profiles. Additional mass loss due to sublimation prior to melting can also be significant due to the delay in the onset of melting within the subsaturated profiles and the small terminal fall speeds and large sublimation rates present prior to the start of melting.

Based on MC3E profile simulations most melting layer profiles are too humid for most of the smallest particle sizes to experience significant mass loss. One of the observed profiles (0510_p1) is conducive to considerable mass loss for all particles sizes as the relative humidity is low enough for significant mass loss and high enough that the particles do not sublimate or evaporate completely. Aggregation, accretion, and collision and coalescence can constrain evaporative mass loss and even cause large particles to gain mass while melting in slightly subsaturated environments.

Particle-scale trends also appear in the bulk distribution parameters such as rainfall rate and IWC. Sublimation within subsaturated profiles removes a large amount of mass prior to melting, resulting in decreasing IWC, TWC, and rainfall rates with increasing distance into the melting layer. Condensational growth in the nearly water-saturated profiles (RH > 95%) results in an increase in LWC and rainfall rate with increasing distance into the melting layer.

Additional results from the MC3E simulations show two of the simulated melting layer profiles (0427_P2 and 0510_P3) have TWC, LWC, and melting layer depths that are similar to observed values. Other profiles compare less favorably due to the presence of cloud liquid water that is unaccounted for in the model or model input. In general, some of the simulated melting layer profiles may have environments and/or initial particle properties that are non-representative of the melting layers that are being studied.

However, there are some caveats that need to be noted. This study utilizes a column model, which is valid over only a small area and assumes homogeneous conditions within the column. Near-homogeneous conditions can be present in the middle of a broad stratiform precipitation region, but not at cloud edges or near embedded precipitation. The model also cannot account for advection of particles and environmental properties (e.g. temperature and moisture) into or out of the column walls, so the time scales in which this model can be applied are limited. This study also uses a fixed environment in which the processes at work on the particles do not feed back into the model environment. In reality, evaporation, melting, and sublimation within the melting layer can have a large impact upon surrounding environmental temperature and relative humidity. This again means that the timescales for which these results apply are limited and significant mass loss within a melting layer profile may be of short duration as evaporation supplies moisture to the environment and melting cools the air so that the profile becomes more saturated over time.

Despite the limitations, results from this study indicate that the assumption of negligible mass loss due to evaporation while melting is occurring is not valid within sufficiently subsaturated environments (average profile RH less than about 85%). To demonstrate the effect of assuming negligible mass loss during melting in subsaturated and saturated melting layers, two additional simulations are conducted. The first simulation uses the 0510_P1 profile, but turns off evaporation and sublimation mass losses (hereafter referred to as "no_evap"). Figure 6-1 shows that the simulated radar reflectivity factor (*Z*) for a Ka-band radar for the no_evap simulation follows the simulated *Z* profile with evaporative mass loss, but has an increasingly high bias in *Z* with increasing distance into the melting layer. Without the evaporative mass loss, the bright band is 50 m deeper than with evaporative mass loss and the peak reflectivity is 3 to 5 dB larger. The larger *Z* for the no_evap simulation compared to the original simulation is likely due to the larger particle diameters, which increases the amount of microwave energy being reflected back in the direction of the radar.

The second simulation uses the 0510_P1 temperature and pressure profile, but sets the RH to 1.0 (100%) for every model layer (hereafter referred to as "RH_1.0") to evaluate the assumption of all melting layers are saturated. The bright band in the RH_1.0 simulation is located in the 0 to 300 m level rather than the 300 to 550 m level in the simulations that use the observed RH profile. The peak *Z* in the RH_1.0 simulation is about 2 dB larger than the peak *Z* in the no_evap simulation; however, both simulations have similar *Z* after melting has completed. The larger peak *Z* in the RH_1.0 simulation compared to the no_evap simulation is likely due to condensation increasing the liquid water mass upon the still large melting ice particles, which increases the particle's dielectric constant and in turn increases the particle's reflectivity. The peak *Z* in the RH_orig simulation is about 6 dB less than the peak *Z* in the RH_1.0 case, which shows another example of how evaporation and sublimation affects the hydrometeors within the melting layer.

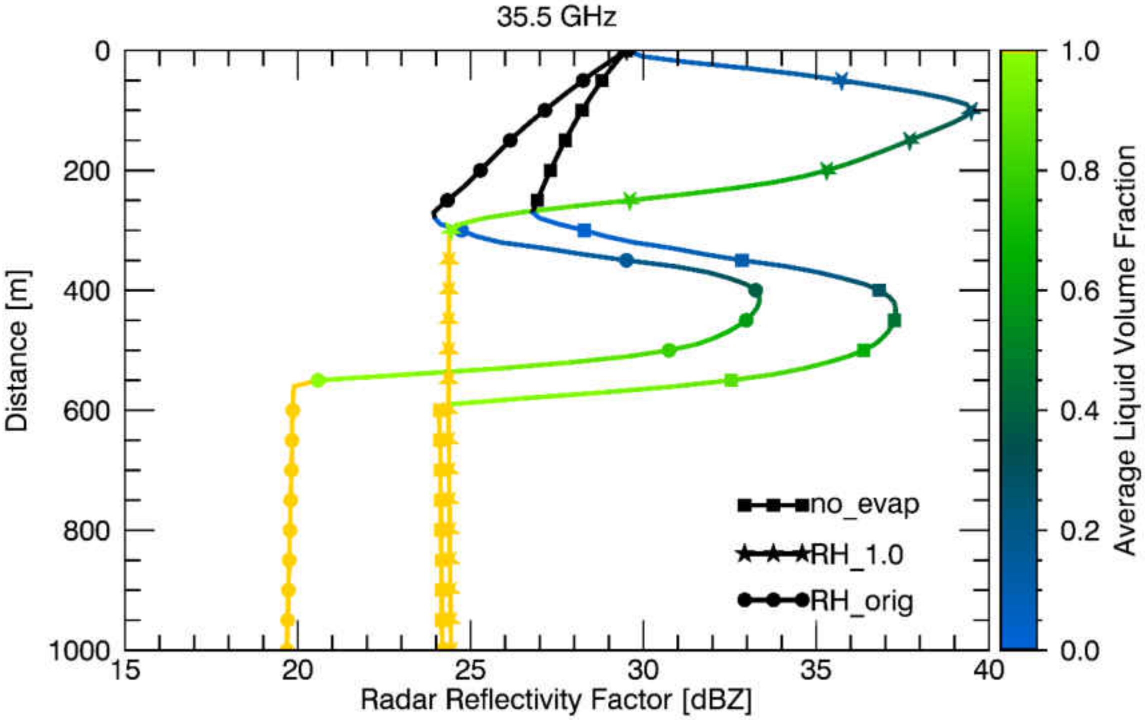

Figure 6-1: a) The simulated radar reflectivity factor (Z) for a 35.5 GHz (Ka band) radar as a function of distance and average liquid volume fraction (color) for the first melting layer profile observed with the UND Citation on 10 May 2011 with the original RH profile (RH_orig) and with RH at all levels set to 100% (RH_1.0). Black denotes particles are completely in the ice phase and yellow denotes particles are completely in the liquid phase.

APPENDIX
MODEL DESCRIPTION

Environmental Variables

Water vapor mixing ratio is calculated from an equation in Olson et al. (2001) and is given by

$$w = \varepsilon RH \frac{e_s\left(T_\infty\right)}{P} \tag{A-1}$$

where ε is the ratio of the gas constant for dry air (R_d) to the gas constant for water vapor (R_v) and equals 0.622, *RH* is the relative humidity, *P* is the ambient air pressure, and $e_s\left(T_\infty\right)$ is the saturated vapor pressure over liquid water at the ambient air temperature (T_∞) at model layer *k*. $e_s\left(T\right)$ is defined by

$$e_s(T) = a_0 + T\left(a_1 + T\left(a_2 + T\left(a_3 + T\left(a_4 + T\left(a_5 + Ta_6\right)\right)\right)\right)\right) \tag{A-2}$$

where *T* is the air temperature in degrees Celsius and the coefficients are given in Table A-1 (Pruppacher and Klett 1997).

Table A-1: Values for the coefficients in eq. (A-2).

Coefficient	Value
a_0	6.107799961
a_1	$4.436518521 \times 10^{-1}$
a_2	$1.428945805 \times 10^{-2}$
a_3	$2.650648471 \times 10^{-4}$
a_4	$3.031240396 \times 10^{-6}$
a_5	$2.034080948 \times 10^{-8}$
a_6	$6.136820929 \times 10^{-11}$

Olson et al. (2001) calculate ambient water vapor density from

$$\rho_v = \frac{RHe_s\left(T_\infty\right)}{R_v T_\infty} \tag{A-3}$$

Other Equations in the Melting Layer Model

There are several thermodynamic properties of an ice particle that must be computed before the melting rate can be determined.

The current parameterization for the ventilation coefficient is from Hall and Pruppacher (1976) and is given by

$$f_v = \begin{cases} 1.0 + 0.14\chi^2 & \chi < 1.0 \\ 0.86 + 0.28\chi & \chi \geq 1.0 \end{cases} \tag{A-4}$$

where

$$\chi = \mathrm{Re}^{\frac{1}{2}}\, Sc^{\frac{1}{3}} \tag{A-5}$$

where Re is the Reynolds number and Sc is the Schmidt number, defined in (3-20). Re is defined using the standard equation:

$$\mathrm{Re} = \frac{v_t D \rho_a}{\eta} \tag{A-6}$$

v_t is the terminal velocity of the particle, *D* is the particle diameter, ρ_a is the air density from (3-22), and η is the dynamic viscosity of air from (3-21).

The shape of the particle is assumed to be a sphere; therefore the dimensionless capacitance (C) is assumed to be a constant 0.5. The saturation vapor pressure at the particle's surface is defined by

$$\rho_{vs} = \frac{e_s\left(T_p\right)}{R_v T_p} \tag{A-7}$$

The total mass is the sum of m_i and m_l. The volume of the air, ice, and liquid water components to the particle are given as

$$V_{ia} = \frac{m_i}{\rho_s} \tag{A-8}$$

$$V_l = \frac{m_l}{\rho_l} \tag{A-9}$$

$$V_i = \frac{m_i}{\rho_i} \tag{A-10}$$

$$V_a = V_{ia} - V_i \tag{A-11}$$

$$V_e = \frac{m_t}{\rho_l} \tag{A-12}$$

Where V_{ia}, V_l, V_i, and V_a are the volumes of the ice-air mixture, liquid water, ice, and air, respectively. V_e is the volume of the particle would have if the total particle mass (m_t) were in liquid form. The particle diameter is computed from the total particle volume (V_t), which is the sum of V_{ia} and V_l, and given by

$$D = \left[\frac{6V_t}{\pi}\right]^{\frac{1}{3}} \tag{A-13}$$

The spherical equivalent diameter is computed using (A-13), but using V_e from (A-12) instead of $\left(V_{ia} + V_l\right)$. The overall particle density is computed by

$$\rho_m = \frac{m_t}{V_t} \tag{A-14}$$

Several of the equations in the melting layer model depend on the melted fraction of the particle. Here, the liquid volume fraction is used to represent the melted fraction of the particle and is given by

$$F_l = \frac{V_l}{\left(V_{ia} + V_l\right)} \tag{A-15}$$

REFERENCES

American Meteorological Society, Ice-bulb temperature. *Gloss. Meteorol.*,. http://glossary.ametsoc.org/wiki/Ice-bulb_temperature (Accessed November 22, 2016).

Bansemer, A., abansemer/soda2. *GitHub*,. https://github.com/abansemer/soda2 (Accessed October 13, 2016).

Battaglia, A., C. Kummerow, D.-B. Shin, and C. Williams, 2003: Constraining Microwave Brightness Temperatures by Radar Brightband Observations. *J. Atmospheric Ocean. Technol.*, **20**, 856–871, doi:10.1175/1520-0426(2003)020<0856:CMBTBR>2.0.CO;2.

Beard, K. V., 1976: Terminal Velocity and Shape of Cloud and Precipitation Drops Aloft. *J. Atmospheric Sci.*, **33**, 851–864, doi:10.1175/1520-0469(1976)033<0851:TVASOC>2.0.CO;2.

——, and H. R. Pruppacher, 1969: A Determination of the Terminal Velocity and Drag of Small Water Drops by Means of a Wind Tunnel. *J. Atmospheric Sci.*, **26**, 1066–1072, doi:10.1175/1520-0469(1969)026<1066:ADOTTV>2.0.CO;2.

——, and ——, 1971: A Wind Tunnel Investigation of the Rate of Evaporation of Small Water Drops Falling at Terminal Velocity in Air. *J. Atmospheric Sci.*, **28**, 1455–1464, doi:10.1175/1520-0469(1971)028<1455:AWTIOT>2.0.CO;2.

Buck, A. L., 1981: New Equations for Computing Vapor Pressure and Enhancement Factor. *J. Appl. Meteorol.*, **20**, 1527–1532, doi:10.1175/1520-0450(1981)020<1527:NEFCVP>2.0.CO;2.

Delene, D. J., 2011: Airborne data processing and analysis software package. *Earth Sci. Inform.*, **4**, 29–44, doi:10.1007/s12145-010-0061-4.

Gunn, R., and G. D. Kinzer, 1949: The terminal velocity of fall for water droplets in stagnant air. *J. Meteorol.*, **6**, 243–248, doi:10.1175/1520-0469(1949)006<0243:TTVOFF>2.0.CO;2.

Hall, W. D., and H. R. Pruppacher, 1976: The Survival of Ice Particles Falling from Cirrus Clouds in Subsaturated Air. *J. Atmospheric Sci.*, **33**, 1995–2006.

Hardaker, P. J., A. R. Holt, and C. G. Collier, 1995: A melting-layer model and its use in correcting for the bright band in single-polarization radar echoes. *Q. J. R. Meteorol. Soc.*, **121**, 495–525.

Heymsfield, A., and R. Wright, 2014: Graupel and Hail Terminal Velocities: Does a "Supercritical" Reynolds Number Apply? *J. Atmospheric Sci.*, **71**, 3392–3403, doi:10.1175/JAS-D-14-0034.1.

Heymsfield, A. J., and C. D. Westbrook, 2010: Advances in the Estimation of Ice Particle Fall Speeds Using Laboratory and Field Measurements. *J. Atmospheric Sci.*, **67**, 2469–2482, doi:10.1175/2010JAS3379.1.

Heymsfield, A. J., C. Schmitt, and A. Bansemer, 2013: Ice Cloud Particle Size Distributions and Pressure-Dependent Terminal Velocities from In Situ Observations at Temperatures from 0° to −86°C. *J. Atmospheric Sci.*, **70**, 4123–4154, doi:10.1175/JAS-D-12-0124.1.

——, A. Bansemer, M. R. Poellot, and N. Wood, 2015: Observations of Ice Microphysics through the Melting Layer. *J. Atmospheric Sci.*, **72**, 2902–2928, doi:10.1175/JAS-D-14-0363.1.

Jacobson, M. Z., and R. P. Turco, 1995: Simulating Condensational Growth, Evaporation, and Coagulation of Aerosols Using a Combined Moving and Stationary Size Grid. *Aerosol Sci. Technol.*, **22**, 73–92.

Jensen, M. P., and Coauthors, 2015: The Midlatitude Continental Convective Clouds Experiment (MC3E). *Bull. Am. Meteorol. Soc.*, doi:10.1175/BAMS-D-14-00228.1. http://journals.ametsoc.org/doi/abs/10.1175/BAMS-D-14-00228.1 (Accessed March 14, 2016).

Korolev, A. V., J. W. Strapp, G. A. Isaac, and A. N. Nevzorov, 1998: The Nevzorov Airborne Hot-Wire LWC–TWC Probe: Principle of Operation and Performance Characteristics. *J. Atmospheric Ocean. Technol.*, **15**, 1495–1510, doi:10.1175/1520-0426(1998)015<1495:TNAHWL>2.0.CO;2.

List, R. J., 1984: *Smithsonian Meteorological Tables*. Smithsonian Institution Press, 527 pp.

Locatelli, J. D., and P. V. Hobbs, 1974: Fall speeds and masses of solid precipitation particles. *J. Geophys. Res.*, **79**, 2185–2197, doi:10.1029/JC079i015p02185.

May, R. D., 1998: Open-path, near-infrared tunable diode laser spectrometer for atmospheric measurements of H2O. *J. Geophys. Res. Atmospheres*, **103**, 19161–19172, doi:10.1029/98JD01678.

Miloshevich, L. M., H. Vömel, D. N. Whiteman, and T. Leblanc, 2009: Accuracy assessment and correction of Vaisala RS92 radiosonde water vapor measurements. *J. Geophys. Res. Atmospheres*, **114**, D11305, doi:10.1029/2008JD011565.

Mitra, S. K., O. Vohl, M. Ahr, and H. R. Pruppacher, 1990: A Wind Tunnel and Theoretical Study of the Melting Behavior of Atmospheric Ice Particles. IV: Experiment and Theory for Snow Flakes. *J. Atmospheric Sci.*, **47**, 584–591, doi:10.1175/1520-0469(1990)047<0584:AWTATS>2.0.CO;2.

Moran, K. P., B. E. Martner, M. J. Post, R. A. Kropfli, D. C. Welsh, and K. B. Widener, 1998: An Unattended Cloud-Profiling Radar for Use in Climate Research. *Bull. Am. Meteorol. Soc.*, **79**, 443–455, doi:10.1175/1520-0477(1998)079<0443:AUCPRF>2.0.CO;2.

Neumann, A. J., M. R. Poellot, A. J. Heymsfield, and A. Bansemer, 2014: An Investigation of Aggregation Within the Melting Layer. https://ams.confex.com/ams/14CLOUD14ATRAD/webprogram/Paper250326.html (Accessed October 15, 2016).

Olson, W. S., P. Bauer, C. D. Kummerow, Y. Hong, and W.-K. Tao, 2001a: A Melting-Layer Model for Passive/Active Microwave Remote Sensing Applications. Part II: Simulation of TRMM Observations. *J. Appl. Meteorol.*, **40**, 1164–1179, doi:10.1175/1520-0450(2001)040<1164:AMLMFP>2.0.CO;2.

——, ——, N. F. Viltard, D. E. Johnson, W.-K. Tao, R. Meneghini, and L. Liao, 2001b: A Melting-Layer Model for Passive/Active Microwave Remote Sensing Applications. Part I: Model Formulation and Comparison with Observations. *J. Appl. Meteorol.*, **40**, 1145–1163, doi:10.1175/1520-0450(2001)040<1145:AMLMFP>2.0.CO;2.

Oraltay, R. G., and J. Hallett, 2005: The Melting Layer: A Laboratory Investigation of Ice Particle Melt and Evaporation near 0°C. *J. Appl. Meteorol.*, **44**, 206–220, doi:10.1175/JAM2194.1.

Petty, G. W., and K. Li, 2013: Improved Passive Microwave Retrievals of Rain Rate over Land and Ocean. Part I: Algorithm Description. *J. Atmospheric Ocean. Technol.*, **30**, 2493–2508, doi:10.1175/JTECH-D-12-00144.1.

Pruppacher, H. R., and J. D. Klett, 1997: *Microphysics of Clouds and Precipitation*. 2nd ed. Kluwer, 954 pp.

Rasmussen, R. M., and A. J. Heymsfield, 1987: Melting and Shedding of Graupel and Hail. Part I: Model Physics. *J. Atmospheric Sci.*, **44**, 2754–2763, doi:10.1175/1520-0469(1987)044<2754:MASOGA>2.0.CO;2.

Rogers, R. R., and M. K. Yau, 1996: *A Short Course in Cloud Physics*. Elsevier, 308 pp.

Stokes, G. M., and S. E. Schwartz, 1994: The Atmospheric Radiation Measurement (ARM) Program: Programmatic Background and Design of the Cloud and Radiation Test Bed. *Bull. Am. Meteorol. Soc.*, **75**, 1201–1221, doi:10.1175/1520-0477(1994)075<1201:TARMPP>2.0.CO;2.

Szyrmer, W., and I. Zawadzki, 1999: Modeling of the Melting Layer. Part I: Dynamics and Microphysics. *J. Atmospheric Sci.*, **56**, 3573–3592, doi:10.1175/1520-0469(1999)056<3573:MOTMLP>2.0.CO;2.

Westbrook, C. D., and A. J. Heymsfield, 2011: Ice Crystals Growing from Vapor in Supercooled Clouds between −2.5° and −22°C: Testing Current Parameterization Methods Using Laboratory Data. *J. Atmospheric Sci.*, **68**, 2416–2429, doi:10.1175/JAS-D-11-017.1.

Willis, P. T., and A. J. Heymsfield, 1989: Structure of the Melting Layer in Mesoscale Convective System Stratiform Precipitation. *J. Atmospheric Sci.*, **46**, 2008–2025, doi:10.1175/1520-0469(1989)046<2008:SOTMLI>2.0.CO;2.